

## Hybrid Maritime Satellite Communication Antenna

**Smith, Thomas Gunst; Larsen, Niels; Breinbjerg, Olav; Gothelf, Ulrich; Kim, Oleksiy S.**

*Publication date:*  
2013

*Document Version*  
Publisher's PDF, also known as Version of record

[Link back to DTU Orbit](#)

*Citation (APA):*  
Smith, T. G., Larsen, N., Breinbjerg, O., Gothelf, U., & Kim, O. S. (2013). Hybrid Maritime Satellite Communication Antenna. Kgs. Lyngby: Technical University of Denmark (DTU).

## DTU Library

Technical Information Center of Denmark

---

### General rights

Copyright and moral rights for the publications made accessible in the public portal are retained by the authors and/or other copyright owners and it is a condition of accessing publications that users recognise and abide by the legal requirements associated with these rights.

- Users may download and print one copy of any publication from the public portal for the purpose of private study or research.
- You may not further distribute the material or use it for any profit-making activity or commercial gain
- You may freely distribute the URL identifying the publication in the public portal

If you believe that this document breaches copyright please contact us providing details, and we will remove access to the work immediately and investigate your claim.

*Thomas Gunst Smith*

# **Hybrid Maritime Satellite Communication Antenna**

PhD thesis, May 2013



# HYBRID MARITIME SATELLITE COMMUNICATION ANTENNA

---

Ph.D. Thesis  
Thomas Smith  
May 2013



The present work was carried out at DTU Elektro and Cobham Satcom in partial fulfilment of the requirements for the Industrial Ph.D. degree from the Technical University of Denmark.

Supervisors:

Ulrich Gothelf, Ph.D.  
Niels Larsen, Ph.D.  
Cobham Satcom

Olav Breinbjerg, Professor, Ph.D.  
Oleksiy S. Kim, Associate Professor, Ph.D.  
Electromagnetic Systems, DTU Elektro,  
Technical University of Denmark



# ABSTRACT

---

Hybrid antennas for a maritime satellite communication terminal with simultaneous operation at L- and Ka-band have been investigated. The frequency bands of interest are 1,525.0 – 1,660.5 MHz (RX+TX, RHCP), 19.7 – 20.2 (RX, LHCP) and 29.5 – 30.0 GHz (TX, RHCP), which are all part of the Inmarsat BGAN and Inmarsat GX services, respectively. The results of this study are three antenna concepts, which demonstrates high performance at both L- and Ka-band.

A combined single/dual-reflector antenna is designed, which presents a favourable way of combining feed antennas for the diverse frequencies<sup>1</sup>. This antenna enables the use of a conventional horn-fed dual-reflector for Ka-band, while a backfire helical antenna is used to form a single-reflector antenna at L-band. Simulations show excellent performance of the L-band backfire helical reflector antenna, due to the utilization of the entire antenna aperture. The Ka-band dual-reflector is inherently a high-gain and low-loss antenna, and investigations show negligible impact of the L-band backfire helical antenna. Therefore, this hybrid single/dual-reflector antenna presents a viable solution to the combined L- and Ka-band antenna.

Novel hybrid antennas that use Frequency Selective Surfaces (FSSs) are investigated, such that an L-band antenna can be located behind and radiate through the Ka-band antenna. A planar periodic FSS, that is reflecting at both 20 and 30 GHz while being transparent at L-band, is designed and analyzed numerically. The FSS is incorporated in a parabolic FSS reflector antenna that is investigated by full-wave analysis tools, and the antenna shows performance comparable to conventional reflector antennas within its frequency band of operation. A planar prototype FSS is manufactured and measured with particular attention to the impact on the performance of an L-band antenna radiating through the FSS. From these investigations, it is concluded that the FSS antenna concept is well suited for hybrid L- and Ka-band operation.

---

<sup>1</sup>Patent pending, PCT/EP2013/050259.

A printed reflectarray antenna with FSS ground-plane is demonstrated. The reflectarray produces a collimated beam as a curved reflector, but its planar profile enables conventional manufacturing techniques used for printed circuit board fabrication. For this purpose, a new type of reflectarray element, the concentric dual split-loop element, is devised and investigated. This compact element facilitates phase-adjustment at 20 and 30 GHz simultaneously, which is exploited by a developed iterative design procedure. A numerical code is implemented to synthesize and analyze reflectarrays, and two prototype reflectarray antennas are fabricated - the first with a conventional solid ground-plane and the second with an FSS ground-plane. The radiation patterns of the prototype reflectarray antennas are measured at the DTU-ESA Spherical Near-Field Antenna Test Facility, as well as the L-band transparency of the FSS-backed reflectarray antenna, and the results demonstrate the high performance of this novel shared-aperture antenna.

## RESUMÉ

---

I nærværende afhandling beskrives studiet af hybridantenner til en maritim satellitkommunikationsterminal med samtidig anvendelse i L- og Ka-bånd. De specifikke frekvensbånd er 1.525, 0–1, 660.5 MHz (RX+TX, RHCP), 19, 7–20, 2 (RX, LHCP) og 29, 5 – 30, 0 GHz (TX, RHCP), som alle er del af Inmarsat BGAN-samt Inmarsat GX-systemet. Resultaterne af dette studie er tre antennekoncepter, der viser høj ydelse ved både L- og Ka-bånd.

En kombineret enkelt/dobbelt-reflektorantenne udvikles, hvor der demonstreres en fordelagtig måde at kombinere fødeantenner til adskilte frekvenser<sup>2</sup>. Denne antenne muliggør brug af en konventionel horn-fødet dobbelt-reflektorantenne ved Ka-bånd, mens en bagudstrålende helixantenne anvendes i en enkelt-reflektorantenne ved L-bånd. Simuleringer viser fortrinlig ydelse for den L-bånds bagudstrålende helixantenne-fødte enkeltreflektor, da hele antenneaperturen udnyttes. Ka-bånds dobbelt-reflektorantennen er naturligt en høj-forstærkning og lav-tabs antenne, og undersøgelser viser begrænset indflydelse af den L-bånds bagudstrålende helixantenne. Derved udgør denne kombinerede enkelt/dobbelt-reflektorantenne et lovende løsningsforslag til en hybrid L- og Ka-bånds antenne.

Nye hybrid-antenner der anvender frekvensselektive flader (FSSer) udvikles således, at en L-bånds antenne kan placeres bagved og transmittere igennem en Ka-bånds antenne. En plan periodisk FSS, der virker reflekterende ved både 20 og 30 GHz, mens den er gennemsigtig ved L-bånd, designes og analyseres numerisk. FSSen anvendes i en paraboloid-formet FSS-reflektorantenne, der undersøges ved brug af integralligningsmetoder, og antennen fremviser ydelse, der er sammenlignelig med konventionelle reflektorantenner. En plan FSS-prototype fremstilles og måles med særligt henblik på påvirkningen af en L-bånds antenne, der stråler gennem FSSen. Af disse undersøgelser konkluderes det, at FSS-antennekonceptet er velegnet til en hybrid L- og Ka-bånds antenne.

En trykt reflectarray-antenne med FSS-jordplan demonstreres. Reflectarrayet frembringer en kollimeret stråle som en krum reflektor, men dets plane

---

<sup>2</sup>Afventer patent, PCT/EP2013/0502259.



profil tillader almindelige produktionsmetoder der anvendes til fremstilling af printplader. Til dette formål udvikles og undersøges en ny type reflectarray-element; det koncentriske dobbelt split-ring element. Dette kompakte element muliggør samtidig fase-justering ved 20 og 30 GHz, hvilket udnyttes i en iterativ designproces. En numerisk kode implementeres til at syntetisere samt analysere reflectarrays, og to prototyper af disse reflectarray-antenner fremstilles - den første med almindeligt jordplan og den andet med et FSS jordplan. Udstrålingsdiagrammer af de to prototype reflectarray-antenner måles i det radiodøde rum ved DTU-ESA Spherical Near-Field Antenna Test Facility, og ligeledes måles L-bånds gennemsigtigheden af reflectarray-antennen med FSS jordplan. Resultaterne fremviser høj ydelse af denne nytænkte aperturdelte antenne.

# PREFACE

---

The work presented in this thesis was carried out at Cobham Satcom<sup>3</sup> and the Electromagnetic Systems Group, Technical University of Denmark (DTU), and was conducted from April 2010 to March 2013. The study was financed by Cobham Satcom with support from the Industrial PhD Programme of the Danish Ministry of Science, Innovation and Higher Education, while prototypes and measurements were provided by DTU.

During the study, I have received guidance and support from a number of people to whom I would like to extend my gratitude. Firstly, I thank my supervisors Ulrich Gothelf and Niels Larsen (Cobham Satcom), and Olav Breinbjerg and Oleksiy S. Kim (DTU). Their continuing inspiration and guidance has been invaluable to the outcome of this study. Min Zhou is thanked for the countless hours of conversation, for proofreading this thesis, and for sharing his expertise within reflectarrays. Martin Nielsen, Jan Mortensen and Frank Persson are all acknowledged for their assistance in practical challenges, and for providing high-precision mounts and support structures for the prototype antennas. Sergey Pivnenko is also thanked for sharing his expertise within antenna measurements, and for conducting these with state-of-the-art accuracy. At Cobham Satcom I have had numerous technical discussions with colleagues in the Antenna R&D division for which I am grateful, and I would particularly like to thank Morten Hagensen and Johan Granholm for their direct and indirect contributions to this project.

Finally, I extend my humble gratitude to my friends and family, for their constant love and support throughout my studies.

Thomas Smith, May 2013

---

<sup>3</sup>Formerly Thrane & Thrane A/S.



# CONTENTS

---

<b>Abstract</b>	<b>i</b>
<b>Resumé</b>	<b>iii</b>
<b>Preface</b>	<b>v</b>
<b>Contents</b>	<b>vii</b>
<b>List of Publications</b>	<b>xi</b>
<b>1 Introduction</b>	<b>1</b>
<b>2 L-/Ka-Band Single-/Dual-Reflector Antenna</b>	<b>5</b>
2.1 Background . . . . .	5
2.2 Antenna Concept . . . . .	6
2.3 L-Band Antenna . . . . .	6
2.3.1 Backfire Monofilar Helical Antenna . . . . .	6
2.3.2 Reflector Antenna Radiation . . . . .	9
2.4 Ka-band Antenna . . . . .	10
2.5 Summary . . . . .	12
<b>3 Frequency Selective Surfaces</b>	<b>15</b>
3.1 Background . . . . .	15
3.2 Planar FSS Ground-Planes . . . . .	16
3.3 Parabolic FSS Reflector Antenna . . . . .	17
3.4 Experimental Validation . . . . .	20
3.5 Summary . . . . .	22
<b>4 Reflectarray Antennas</b>	<b>25</b>
4.1 Background . . . . .	25

4.2	Antenna Concept . . . . .	26
4.3	Reflectarray Analysis . . . . .	27
4.4	Reflectarray Element . . . . .	28
4.4.1	CDSL with Solid Ground-Plane . . . . .	29
4.4.2	CDSL with FSS Ground-Plane . . . . .	31
4.5	Reflectarray Design Procedure . . . . .	32
4.6	Prototype Antennas . . . . .	33
4.6.1	Reflectarray with Solid Ground-Plane . . . . .	35
4.6.2	Reflectarray with FSS Ground-Plane . . . . .	37
4.7	Summary . . . . .	40
<b>5</b>	<b>Conclusions</b>	<b>43</b>
<b>A</b>	<b>Reflectarray Modeling</b>	<b>47</b>
A.1	Element Analysis . . . . .	47
A.2	Far-Field Calculation . . . . .	47
A.3	Validation . . . . .	49
A.3.1	DTU/Ticra sample I . . . . .	49
A.3.2	DTU/Ticra sample II . . . . .	51
<b>B</b>	<b>Variable Rotation Technique</b>	<b>53</b>
B.1	Derivation . . . . .	53
B.2	Circular Polarized Reflection Coefficients . . . . .	55
B.3	Dipole Example . . . . .	57
	<b>Publications</b>	<b>63</b>
	<b>Journal Paper I</b>	<b>63</b>
	<b>Journal Paper II</b>	<b>69</b>
	<b>Conference Paper I</b>	<b>79</b>
	<b>Conference Paper II</b>	<b>87</b>
	<b>Conference Paper III</b>	<b>95</b>
	<b>Patent Application I</b>	<b>101</b>

---

**Bibliography**

**119**



# LIST OF PUBLICATIONS

---

During this study, the journal papers [J1,J2], conference papers [C1–C3] and patent application [P1] have been prepared. All publications are included in the last part of this thesis.

## Journal Publications

- [J1] T. Smith, U. Gothelf, O. S. Kim, and O. Breinbjerg, “Design, Manufacturing, and Testing of a 20/30 GHz Dual-Band Circularly Polarized Reflectarray Antenna”, *Submitted to IEEE Antennas Wireless Propag. Lett.*, 2013.
- [J2] T. Smith, U. Gothelf, O. S. Kim, and O. Breinbjerg, “An FSS-backed 20/30 GHz Circularly Polarized Reflectarray for a Shared Aperture L- and Ka-band Satellite Communication Antenna”, *Submitted to IEEE Trans. Antennas Propag.*, 2013.

## Conference Publications

- [C1] T. Smith, N. Larsen, U. Gothelf, O. S. Kim, and O. Breinbjerg “Investigation of Backfire Monofilar Helical Antenna”, in *Proc. EuCAP*, Rome, Italy, 2011.
- [C2] T. Smith, N. Larsen, U. Gothelf, O. S. Kim, and O. Breinbjerg, “20/30 GHz Dual-Band Circularly Polarized Reflectarray Antenna based on the Concentric Dual Split-Loop Element”, in *Proc. 33rd ESA Antenna Workshop*, Noordwijk, The Netherlands, 2012.
- [C3] T. Smith, N. Larsen, U. Gothelf, O. S. Kim, and O. Breinbjerg, “An Offset-Fed 20/30 GHz Dual-Band Circularly Polarized Reflectarray Antenna”, in *Proc. EuCAP*, Göteborg, Sweden, 2013.



**Patent Publications**

- [P1] T. Smith, J. Granholm, O. S. Kim, and O. Breinbjerg, “Combined L-band (1-2 GHz) and Ka-band (20-30 GHz) Antenna”, Patent Application PCT/EP2013/050259, 2013.

# INTRODUCTION

---

High-frequency satellite communication antennas are subject to intense research and development efforts due to growing demands for global broadband communication [1, 2]. The Inmarsat Global Xpress (GX) system has been designed to be launched through 2013 and 2014, that will provide data transfer speeds up to 50 Mbps. The system utilize the frequency bands 19.2 to 20.2 GHz for receive (RX) and 29.0 to 30.0 GHz for transmit (TX) [3], from the user terminal point of view. The utilized frequencies lie in the Ka-band<sup>1</sup> frequency spectrum, which enables the large data bandwidth. However, the Ka-band presents many challenges, the biggest being the rain attenuation problem, which may easily cause the total path-loss to increase by more than 20 dB. Some techniques have been developed to compensate this problem, but at the expense of system capacity [2].

Satellite communication services at L-band have matured for decades and are very robust towards bad weather, where the data transfer speed is almost unaffected even in heavy rain. Existing L-band products at Cobham Satcom, operating in the Inmarsat Broadband Global Access Network (BGAN) from 1,525.0 to 1,660.5 MHz [4], provide up to 432 Kbps which is sufficient for voice communication, safety services and small amounts of data transfer [5], but is insufficient for high-definition video streaming and interactive multi-media services.

To provide maximum data speed and link stability simultaneously, a hybrid L- and Ka-band satellite communication user terminal is proposed. Though it is presently possible by combining two physically separate antennas, it is a desired feature to merge these two in a single antenna unit. This idea is not only aesthetically appealing, but also presents technical advantages by sharing antenna hardware for both frequencies, e.g. the radome, pedestal, power supply, cables, etc. It is thus evident that such a hybrid antenna is a favorable product for both the manufacturer and the consumers.

---

<sup>1</sup>Though the RX frequency band technically lies in the IEEE K-band, it is referred to as Ka-band in relation to satellite communication [2].

Hybrid antennas for different operating frequencies exist in a broad variety of sizes and shapes, and the applied antenna topologies depend on the application frequencies and specifications. The reflector antenna is a commonly used high-gain antenna, due to its low losses and mature design and analysis tools [6, 7], but has also been applied in medium-gain applications [8, 9]. Reflector antennas for multi-band operation have been designed using collocated feed antennas [10, 11] or by spatially separating the feed antennas for different frequencies [12–16]. The choice of feed antenna is usually determined by the operating frequency and the requirements to the dimensions of the antenna. However, for electrically small reflector antennas, the size of the feed antenna may become large compared to the reflector aperture and cause undesirable amounts of feed blockage, which render traditional feed antennas inapplicable.

During the 1950s, frequency selective surfaces (FSSs) became a growing research topic for military applications such as minimizing the radar cross section of antennas and military vehicles [17, 18]. Since then, FSSs have been exploited in the design of multi-band antennas [12–16, 19, 20], and present a potential solution for a hybrid L- and Ka-band antenna.

Multi-band microstrip array antennas have been utilized for widely separated frequencies [21–27]. However, for electrically large array antennas, losses in the microstrip feeding network are significant which deteriorate the overall antenna performance [28, 29]. The reflectarray antenna combines desirable features of the reflector antenna and the phased array antenna [30, 31]. Printed reflectarrays have been subject of increasing research interest, and broadband [32–37], dual-band [38–50] and multi-band [51, 52] reflectarrays have been proposed, and the applied reflectarray topology is determined by the separation of utilized frequencies and polarizations.

Though many hybrid antenna technologies exist, none of them are easily applied in this project due to primarily two reasons, namely the required polarizations at 20 and 30 GHz, and the very wide separation of the L and Ka frequency bands. The proposed hybrid antenna thus calls for investigations into new multi-band antenna technologies.

The overall purpose of this study is to design a hybrid antenna for a maritime satellite communication terminal of 60 cm diameter, with simultaneous operation at L- and Ka-band. The hybrid antenna Ka-band is desired to have a performance that is comparable to similar-sized purely Ka-band antennas, which means that the inclusion of the L-band antenna should have negligible impact.

The L-band part of the hybrid antenna is aimed at the Inmarsat BGAN system which utilizes the user terminal side receive (RX) frequency band from 1,525 to 1,559 MHz and the transmit (TX) frequency band from 1,626.5 to

**Table 1.1** *Frequency band specifications.*

L-band	RX	1,525.0 – 1,559.0 MHz	RHCP
	TX	1,626.5 – 1,660.5 MHz	RHCP
Ka-band	RX	19.7 – 20.2 GHz	LHCP
	TX	29.5 – 30.0 GHz	RHCP

1,660.5 MHz<sup>2</sup>. Right-hand circular polarization (RHCP) is used in both RX and TX frequency bands.

At Ka-band, frequency specifications for this project were established as RX from 19.7 to 20.2 GHz and TX from 29.5 to 30.0 GHz<sup>3</sup>. Left-hand circular polarization (LHCP) is used in the RX frequency band, while RHCP is used in the TX frequency band. The frequency bands and polarizations are summarized in Table 1.1.

When this study was initiated in 2010, it was expected that the new Inmarsat GX Ka-band satellites would be collocated with the existing Inmarsat L-band satellites, which meant that the hybrid antenna should radiate in the same direction at L- and Ka-band. However, during the Inmarsat GX satellites were specified not to be collocated with the existing L-band satellites. Therefore, the antennas investigated in this project include antennas for collocated satellites as well as dispersed satellites.

During this project, two journal papers [J1,J2], three conference papers [C1–C3], and one patent application [P1] have been prepared. The thesis presents an overview of these papers, but also includes parts of work and topics that were not described in the publications. A list of these works can be found on page xi.

The thesis is organized as follows: Chapter 2 presents the investigations of a combined L-/Ka-band single-/dual-reflector antenna. The antenna consists of a conventional Ka-band dual-reflector, while a backfire helical antenna that is mounted on the shadow side of the Ka-band sub-reflector is used as feed antenna for the L-band single-reflector. The backfire helical antenna is analyzed, and its radiation and impedance characteristics are investigated by a parametric study. The impact of the L-band backfire helical antenna on the Ka-band dual-reflector radiation is also assessed. In Chapter 3, a study on the applicability of FSSs in stacked hybrid antennas are presented. The results of a numerical investigation of a Ka-band parabolic FSS reflector antenna are given, and the performance

<sup>2</sup>The specified L-band frequencies constitute the current BGAN system, though an extended frequency range is planned for the coming BGAN XL system.

<sup>3</sup>The specified Ka-band frequencies cover only half of the presently specified Inmarsat GX frequency bands, 19.2–20.2 GHz and 29.0–30.0 GHz, which were not defined when this project was initiated.

of an L-band antenna radiating through the FSS is assessed by an experimental measurement campaign. Chapter 4 presents the design and analyses of a Ka-band FSS-backed reflectarray antenna. Details on the utilized concentric dual split-loop element are given, and an iterative reflectarray design procedure is presented. The results of a measurement campaign on two prototype reflectarray antennas are also analyzed. In Chapter 5, the conclusions of this study are summarized and recommendations for future work are given. In addition to these chapters, appendices are included followed by the publications that have been prepared during the study.

Throughout this thesis, the harmonic time dependence  $e^{j\omega t}$ ,  $\omega$  being the angular frequency, is assumed and suppressed.

# L-/KA-BAND SINGLE-/DUAL-REFLECTOR ANTENNA

---

In this chapter, the results of numerical analyses of a combined L- and Ka-band reflector antenna are given. A parametric investigation of the L-band feed antenna is presented to outline the attractive features of this specific antenna in a combined single/dual reflector antenna system. The combined L- and Ka-band antenna performance is demonstrated numerically by analysis of both the L- and Ka-band radiation characteristics of the antenna, and the influence of the L-band feed antenna on the Ka-band performance is assessed.

Due to Cobham Satcoms desire to patent the presented hybrid antenna concept, paper publications were limited to the isolated backfire helical antenna [C1] and not the entire hybrid L- and Ka-band reflector antenna configuration, which is, however, described in the patent application [P1].

## 2.1 Background

For high-frequency, high-gain antennas, the reflector antenna is commonly used due to its inherently low losses and mature methods of analysis. A reflector antenna consists of a feed antenna and a reflecting surface. For pencil beam antennas, the reflecting surface is shaped such that a collimated beam is obtained in the desired direction, which traditionally is achieved by using a paraboloidal reflecting surface, and placing the feed antenna phase center in the focal point of the paraboloid [6, 7].

In this project, it has been investigated how a Ka-band dual-reflector antenna can be combined with different L-band antennas. The possible antenna configurations include L-band helices distributed in the Ka-band main reflector, an L-band axial-mode helical antenna located in front of the Ka-band sub-reflector which can radiate directly towards the satellite or utilize the main reflector, and similar configurations using L-band patch antennas instead of helical antennas. However, investigations indicated that the L-band antennas distributed in the

main reflector will introduce scattering at Ka-band in arbitrary directions and polarizations, which will degrade the Ka-band performance and possibly render it impossible to comply with the antenna specifications. The same holds for the L-band antennas located on the Ka-band sub-reflector that utilize the main reflector, since both the axial-mode helical antenna and the patch antenna needs a ground-plane considerably larger than the Ka-band sub-reflector, which will cause undesirable scattering at Ka-band.

In the literature, multi-band reflector antennas have been designed using either collocated feed antennas for the different frequency bands [10, 11] or by using an FSS sub-reflector to spatially separate the feed antennas [12–16]. Since the wavelength at L-band is in the order of 20 cm, the conventional horn feed antenna is an impractical choice of feed antenna due to the consequent size, mass, and the amount of blockage that will be introduced [53]. Alternative feed antennas have been developed, e.g. a dipole-disk antenna [54], or a backfire helical antenna wound around a metal rod [55].

None of the applied L-band feed antennas are easily incorporated in a Ka-band reflector antenna design, and will introduce a significant amount of blockage since it may be located in the Ka-band ray paths [53]. Therefore, a combined L- and Ka-band reflector antenna requires a new type of L-band feed antenna to be developed.

## 2.2 Antenna Concept

In this project, an L-band backfire helical antenna has been designed and investigated, whose ground-plane can be combined with the Ka-band sub-reflector. Depending on the actual size of the Ka-band sub-reflector, the backfire helical feed can be designed such that the diameter of the helical coil is smaller than the sub-reflector, thus the scattering of the helical antenna should be small at Ka-band. The configuration is depicted in Figure 2.1.

## 2.3 L-Band Antenna

The results of the investigations of the proposed L-band antenna are divided into discussions on the developed feed antenna and the complete reflector antenna performance.

### 2.3.1 Backfire Monofilar Helical Antenna

A monofilar helical antenna typically consists of a conducting wire that is wound into a helical shape, a conducting ground-plane, and a feed point between the

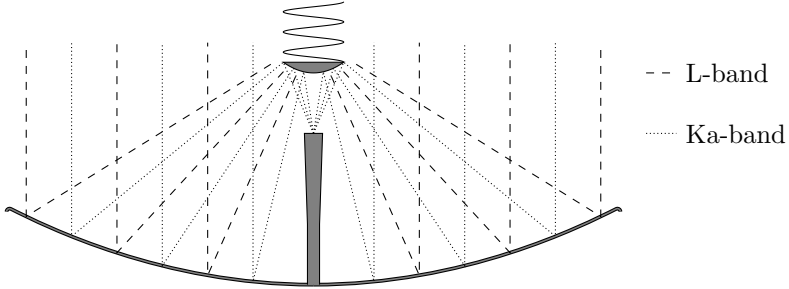


**Figure 2.1** *Ka-band Cassegrain antenna with L-band backfire helical antenna. A coordinate system is defined with the  $xy$ -plane in the plane of the upper sub-reflector surface and the  $x$ -axis intersects the excitation point between the helix coil and the sub-reflector.*

two [7, 56], see Figure 2.2. The antenna may be driven in different modes of radiation, which are often denoted the normal mode and the axial mode. In the normal mode, the antenna radiates in the direction normal to the axis of the helix, while the axial mode provides a radiation maximum along the axis of the helix.

The antenna operating mode is determined by the geometrical parameters of the helical antenna, i.e. the circumference of the helix coil  $C_h = 2\pi r_h$ , the circumference of the ground-plane  $C_g = 2\pi r_g$ , the spacing between turns  $S$  and the number of turns  $n$ . The normal mode is excited when  $C_h \ll \lambda_0$ , with  $\lambda_0$  being the free space wavelength, while the axial mode is excited when  $C_h \approx \lambda_0$  [57, 58]. However, the direction of the axial mode radiation is found to depend on the size of the ground-plane. For large ground-planes ( $C_g \gtrsim 1.3\lambda_0$ ), the direction of maximum radiation is in the direction away from the feed point, denoted endfire radiation, but for small ground-planes ( $C_g \lesssim 1.3\lambda_0$ ) the maximum radiation is in the direction towards the feed point [59, 60].

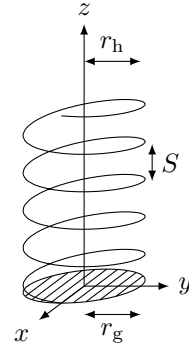


**Figure 2.2** *Geometry of the backfire monofilar helical antenna.*

In this study, monofilar helical antennas were investigated by the commercial



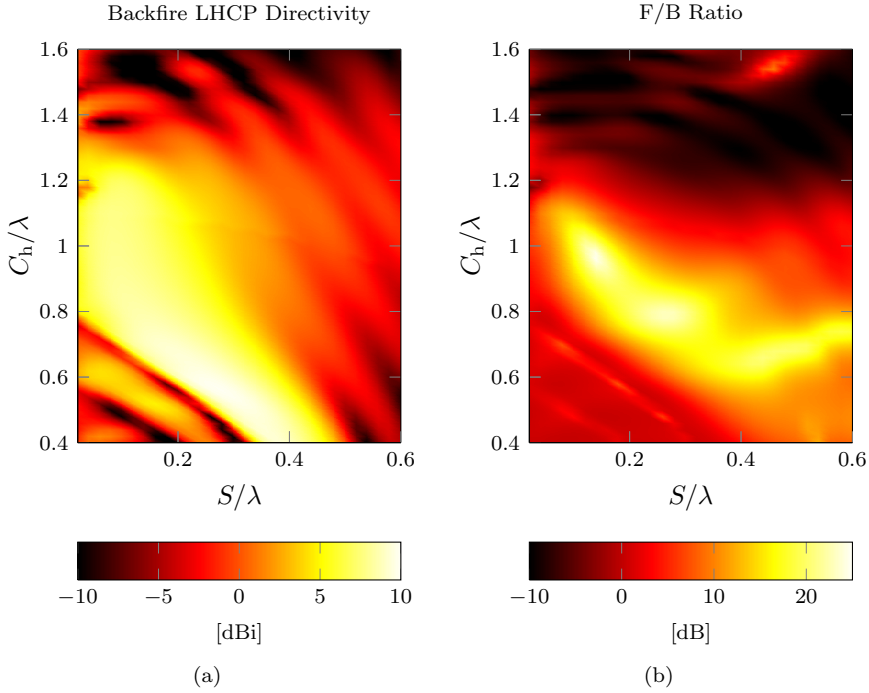


**Figure 2.3** Influence of the helical geometry on the (a) backfire LHCP directivity and (b) F/B ratio for  $C_g = C_h$ .

software HFSS and AWAS [61,62] as well as a developed integral equation analysis tool. A parametric investigation of the backfire monofilar helical antenna was conducted. Herein, the operating modes were explained by either slow and fast waves propagating along the helical conductor, that yields radiation in the endfire or backfire direction, respectively [C1]. In Figure 2.3a, the LHCP backfire directivity is shown for different combinations of  $S$  and  $C_h$ , keeping  $C_g = C_h$ . For spacing between turns in the order of  $0.1\lambda_0$ , maximum directivity is achieved when the circumference of the helix is between  $0.8\lambda_0$  and  $1.2\lambda_0$ , which is similar to the observations of axial mode helical antennas operating in the endfire mode [56]. High directivity may also be achieved for helical antennas of small circumference,  $C_h = 0.4\lambda_0$ , when the spacing between turns is large, i.e. in the order of  $S \approx 0.4\lambda_0$ .

It is seen that high directivity may be achieved for very different combinations

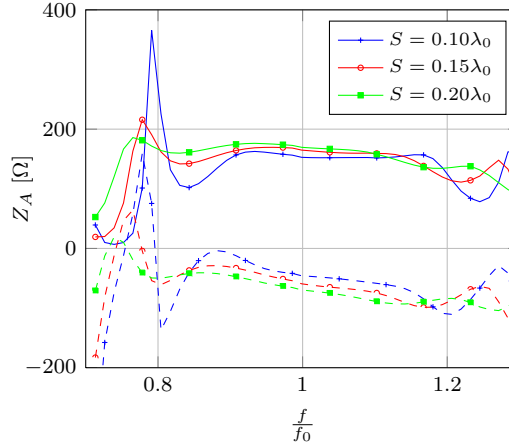


**Figure 2.4** *Input resistance (solid) and reactance (dashed) of the backfire monofilar helical antenna over normalized frequency range, for  $C_g = C_h = 1.0\lambda_0$ .*

of  $S$  and  $C_h$ , however, the front-to-back<sup>1</sup> (F/B) ratio is not necessarily high as seen from Fig. 2.3b. This is exemplified by the configuration  $C_h = 0.58\lambda_0$  and  $S = 0.28\lambda_0$  where maximum directivity of 9.9 dBi is achieved. For this antenna, the F/B ratio is 4.4 dB which may be unacceptable in some applications.

A maximum F/B ratio of 24.7 dB is achieved for the antenna configuration  $S = 0.14\lambda_0$  and  $C_h = 0.96\lambda_0$ , in which case the directivity is 7.6 dBi. From the parametric investigations, it is found that the backfire helical antenna can be operated with an F/B ratio better than 10 dB over a 37 % bandwidth [C1].

The backfire monofilar helical antenna exhibit wideband behavior similar to the endfire radiating helical antenna. In Figure 2.4, the input impedance of a 5-turn backfire helical antenna with  $C_g = C_h = \lambda_0$  is shown for three different spacings between turns. It is found that for the three cases, bandwidths of 36 %, 51 % and 64 % are obtained with return loss better than 15 dB by a simple two-component match to 50  $\Omega$  [C1].

### 2.3.2 Reflector Antenna Radiation

A backfire monofilar helical antenna has been designed to serve as feeding antenna for a single reflector antenna. The parameters of the helical antenna are

<sup>1</sup>Here, “front” refers to the direction of backfire direction.

given in Table 2.1 and the radiation pattern is shown in Figure 2.5a. The maximum backfire directivity is 8.2 dBi and the on-axis cross polarization is 24.7 dB below that. It is observed that the directivity in the endfire direction is about -7 dBi. Investigations have shown that the backfire monofilar helical antenna has a phase center on the axis of symmetry approximately 25 mm from the ground-plane inside the helix coil. This feature makes the backfire monofilar helical antenna ideal for usage in a multi-band Cassegrain antenna, since its phase center may be located close to the focal point of the paraboloidal main reflector.

The simulated radiation pattern of a 60 cm paraboloidal reflector antenna with  $F/D=0.47$  illuminated by the backfire monofilar helical feed antenna is depicted in Figure 2.5b. The antenna configuration is analyzed as a whole using method of moments (MoM) in GRASP, thus feed blockage is inherently included in the model. The backfire helical antenna is located such that its phase center and the focal point of the reflector coincide. The maximum directivity is 18.2 dBi, which corresponds to an aperture illumination efficiency of 70 %, neglecting losses. The side lobe level and on-axis cross polarization is 16.7 dB and 31.8 dB below that, respectively. The radiation in the backward direction is caused by edge diffraction on the main reflector, which may be altered by shaping of the reflector edge. Overall, the antenna complies to the Inmarsat Class 8 specifications for use in the L-band Inmarsat BGAN system [4].

**Table 2.1** *Parameters of the backfire monofilar helical feed antenna.*

$C_h$	176 mm
$C_g$	176 mm
$S$	18.5 mm
$n$	5

The investigations in this project were limited to backfire monofilar helical antennas. However, better performance in terms of the F/B ratio and the cross polarization may be achieved by e.g. backfire bifilar helical antennas [63]. Depending on the size of the Ka-band sub-reflector, which is a vital part of the Ka-band antenna design, the helical antenna geometry should be changed accordingly, while preserving the backfire radiating mode.

## 2.4 Ka-band Antenna

Considering the combined L- and Ka-band reflector antenna by Geometrical Optics (GO), the L-band feed antenna may be designed to be confined in the shadow region of the Ka-band sub-reflector. However, diffracted rays are produced at the edges of the structure, e.g. sub- or main reflector, which enter the shadow region and thus illuminates the helix coil [64, 65]. Due to this, the impact of the backfire helical antenna on the Ka-band radiation is assessed by

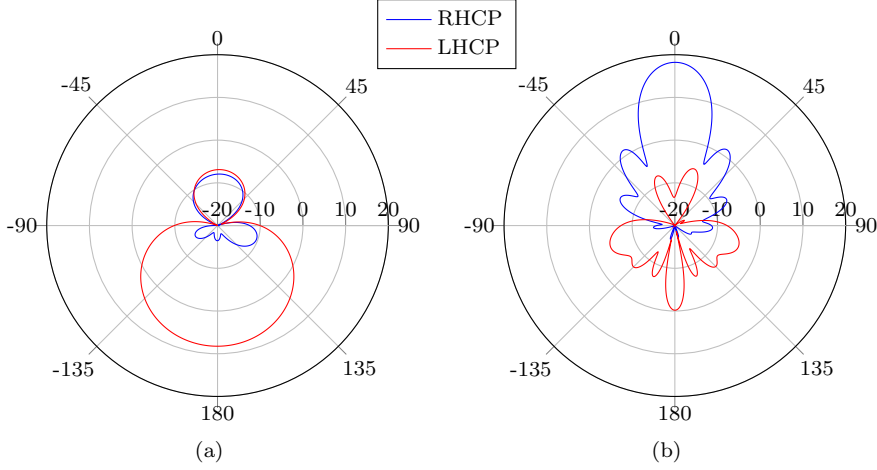


**Figure 2.5** Simulated directivity patterns of (a) the backfire monofilar helical antenna alone and (b) a 60 cm reflector antenna with  $F/D=0.47$  fed by the helical antenna, at 1,542 MHz in the  $\phi = 0^\circ$ .

investigations of a 60 cm Cassegrain type dual reflector antenna. The geometry is similar to the geometry depicted in Figure 2.1, and an LHCP Gaussian beam pattern is used as feeding antenna. The antenna is investigated using physical optics (PO) and physical theory of diffraction (PTD) in GRASP.

The radiation pattern of the Cassegrain antenna is shown in Figure 2.6, where the antenna including the backfire helical antenna is compared to the reference, i.e. the same antenna excluding the backfire helical antenna. The maximum directivity of the antenna including the backfire helical antenna is 42.8 dBi, which is 0.05 dB lower than the reference. The cross polarization and side lobe levels are 32.7 and 19.9 dB below the maximum directivity, which are both 0.6 dB higher than the reference. The radiation pattern further away from the main beam has shown similar negligible changes.

It should be noted that the general high side lobe level is caused by the blockage of the large sub-reflector of 56 mm diameter. However, the low impact of the backfire helical antenna on a small sub-reflector has been experimentally validated in a concurrent project at Cobham Satcom.

The results of this Ka-band investigation proves that the placement of the L-band backfire monofilar helical antenna in the shadow region of the sub-reflector introduces negligible scattering. Thus the Ka-band dual-reflector antenna can be optimized using commercially available software for this purpose, such as GRASP [66], and is able to maintain its performance despite the introduction of

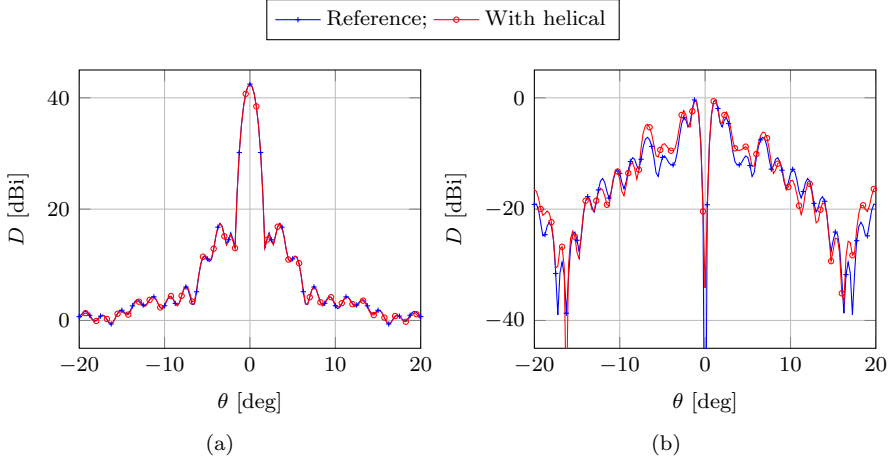


**Figure 2.6** (a) RHCP and (b) LHCP directivity pattern of the Ka-band Cassegrain antenna with and without the L-band backfire helical feed antenna, at 30.0 GHz in the  $\phi = 0^\circ$  plane.

the L-band antenna. However, the feeding of the L-band backfire helical antenna is an unattended concern that must be considered. Methods of drawing the L-band feeding cable are given in [P1], but the consequences of these should be attended.

## 2.5 Summary

A novel combined L-band single reflector and Ka-band dual reflector antenna has been developed. The L-band feeding antenna is a backfire monofilar helical antenna whose ground-plane may be combined with the sub-reflector of the Ka-band antenna. The antenna has been investigated numerically, using full-wave MoM at L-band and combined MoM/PO at Ka-band.

At L-band, the antenna demonstrates excellent performance, and the radiation pattern complies with the Inmarsat Class 8 specifications<sup>2</sup>. The aperture illumination efficiency is 70 %, which is satisfactory considering that the main reflector is only about  $3\lambda$  in diameter.

The motivation of this antenna was to facilitate conventional reflector antenna design for the Ka-band antenna. It was shown that the introduction of

<sup>2</sup>The radiation in the  $\theta = 180^\circ$  direction exceeds the specification envelope, however, antenna hardware will be mounted on the back of the antenna which will change the radiation in this direction.

the backfire helical antenna in the shadow region of the sub-reflector did in fact not affect the Ka-band radiation pattern noticeably.

Based on the results in this chapter, the antenna concept is considered a feasible candidate for simultaneous operation at L- and Ka-band, however, the actual feeding of the backfire helical antenna must be attended. Two methods of providing the L-band signal to the backfire helical antenna are described in the patent application [P1]. Optimization of the dual-reflector antenna to comply with Ka-band radiation specifications should be conducted.



## FREQUENCY SELECTIVE SURFACES

---

An investigation of the applicability of frequency selective surfaces (FSSs<sup>1</sup>) has been carried out, and the work is summarized in this chapter. Planar FSSs that are reflecting at 20 and 30 GHz, while being transparent at L-band, have been designed. A planar FSS design has been utilized in a numerical investigation of a paraboloidal reflector, and the performance of this antenna is presented. Lastly, the L-band transparency of a Ka-band reflecting FSS was validated experimentally, and these results are discussed.

### 3.1 Background

An FSS consists of identical scattering elements placed in a two-dimensional periodic grid, and are typically designed to have transmission and reflection properties which vary with frequency [17, 18]. Investigations into FSSs accelerated after the World War II with the purpose of minimizing the radar cross section of antennas and military vehicles. Since then, FSSs have been utilized in many civil and commercial applications, such as low-RCS radomes [67, 68], spatial filters [69, 70], polarizers [71–74], and multi-band antennas [12–15, 19, 20].

The possible FSS antenna configurations can generally be divided into two groups; one where an FSS Ka-band antenna is located in front of an L-band antenna, and a second where an FSS L-band antenna is located in front of a Ka-band antenna. Common for both groups is that the FSS antenna must be transparent for the non-FSS antenna, e.g. in the first group the FSS Ka-band antenna must be transparent at L-band. In this way, the non-FSS antenna may be designed using conventional antenna technologies.

In [19, 20], FSSs are utilized for dual-band antenna designs, where a low-frequency antenna is located behind a high-frequency FSS reflector antenna.

---

<sup>1</sup>FSSs are also known as dichroic surfaces in the literature, but are only referred to as FSSs in this thesis for simplicity.



However, in this study, the FSS must be reflective at both 20 and 30 GHz which calls for a multi-band FSS element design. Meanwhile, the transmission loss of the FSS must be low at L-band, to ensure minimum influence on the L-band antenna radiation and impedance.

### 3.2 Planar FSS Ground-Planes

Though FSSs are used in the design of curved sub- or main reflectors in multi-band antennas, they are usually designed and analyzed as planar infinite structures [69, 75]. Using this approach, the computational problem is reduced to a single FSS element that may be analyzed using commercial software that incorporates periodic boundaries. For microstrip FSSs, 2.5D MoM is computationally efficient, and the software Ansys Designer [76] that utilizes this formulation is used in this study.

The large separation between the Ka-band RX and TX frequencies makes it infeasible to cover the entire frequency spectrum in between by using a single broadband FSS element type. Single-layer multi-band FSSs for circular polarization may be designed using interleaved crossed dipoles of different sizes [77], fractal elements [78], combinations of different element geometries [79], etc. However, a variety of concentric loop elements with multi-band reflective properties has previously demonstrated good performance [13, 80, 81], which are utilized in this project due to the later application that will be described in Chapter 4.

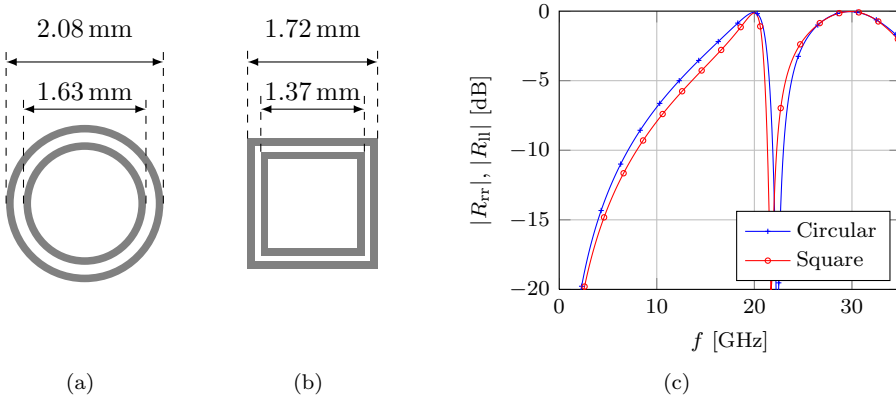


**Figure 3.1** Geometry of (a) the concentric circular loop element and (b) the concentric square loop element printed on a 0.787 mm Rogers 5880 Duroid substrate, and (c) their frequency response.

**Table 3.1** *Reflecion coefficients of the concentric circular and square loop elements printed on a 0.787mm Rogers 5880 substrate in the frequency bands of interest.*

	1,525.0–1,660.5,MHz	19.7–20.2 GHz	29.5–30.0 GHz
	$\max( R_{rr} )$	$\min( R_{ll} )$	$\min( R_{rr} )$
Conc. circular loop	-22.6 dB	-0.13 dB	-0.04 dB
Conc. square loop	-23.7 dB	-0.24 dB	-0.04 dB

FSSs consisting of concentric circular or square loop elements, printed on a 0.787mm Rogers 5880 substrate, have been optimized to be reflective at 20 and 30 GHz. The frequency responses of these FSSs are shown in Figure 3.1, where the magnitude of the reflection coefficient for a normal incidence plane wave is depicted. The reflection coefficients in the frequency bands of interest are summarized in Table 3.1. In both cases, the reflection coefficient at L-band is below -20 dB. However, it is observed that the concentric circular loop element provides a larger reflection bandwidth around 20 GHz, which also results in a higher minimum reflection coefficient.

From the two FSS designs, it is evident that the concentric loop elements can be tuned to be reflective at 20 and 30 GHz while being transparent at L-band. However, the investigations are conducted assuming plane wave incidence, while in the real antenna configuration the FSS will be located in the near-field region of the L-band antenna. The field radiating through the FSS will thus be a summation of plane waves, and the true impact on the L-band antenna should be assessed.

### 3.3 Parabolic FSS Reflector Antenna

A parabolic FSS reflector antenna has been investigated numerically. The configuration is depicted in Figure 3.2 where a Ka-band dual reflector antenna with an FSS main reflector is located in front of an L-band patch array antenna. The FSS is designed to be reflective at the two separate Ka-band frequency bands and transparent at L-band, and consists of concentric square loop elements.

In this project, only the Ka-band FSS reflector antenna was investigated. The aim was to design the FSS reflector antenna such that a conventional L-band patch array can be located behind and radiate through, and at the same time operate at Ka-band. Due to the electrically large dimensions of the FSS reflector at Ka-band, the FSS is considered locally planar and infinite, thus the elements are designed and analyzed similarly to the planar FSS ground-planes. However, to validate the performance of the actual parabolic FSS reflector, a

free-standing parabolic FSS reflector has been investigated using the commercial software GRASP, since neglecting dielectric substrate reduces the computational burden considerably.

A practical concern arises in the distribution of FSS elements on a double-curved surface, since any projection of a regular element grid will be distorted and may change inter-element spacing and element dimensions. However, it has been found that for parabolic reflectors with moderate focal length over diameter ratio ( $F/D$ ), i.e.  $F/D \lesssim 0.5$ , a planar projection of the element grid yields good performance. A routine has been implemented that adjusts the side lengths of the concentric square loops on the double-curved surface such that they are equal to the side lengths of the planar square loops, which would otherwise entail a frequency shift of the reflective properties of the FSS.

To accurately investigate the effects of the double-curved FSS reflector, the antenna was investigated using MoM. However, the analysis is computationally heavy, thus the analysis was carried out on an FSS reflector with 20 cm diameter, which includes 4,800 concentric square loop elements. The paraboloidal shape has  $F/D=0.4$ , and an LHCP Gaussian beam is used as feed.

The FSS reflector antenna is compared to an identical perfect electric conductor (PEC) reflector. The radiation patterns of the two reflector antennas are shown in Figure 3.3, at 30.0 GHz in the  $\phi = 45^\circ$  plane. Minor differences are noticed in the co-polar pattern, the most profound being the side lobe at  $30^\circ$  which is about 5 dB higher for the FSS reflector. The maximum directivity of the FSS reflector is 34.4 dBi, which is 0.3 dB lower than the PEC reflector, and only small changes are observed in the side lobe levels. For the PEC reflector, the cross polarization level is 48.8 dB below the maximum directivity, but for the FSS reflector the cross polarization level rises to 38.9 dB below maximum directivity. This is mainly due to the FSS elements being skewed in the planar projection onto the paraboloidal reflector surface and, as a result, the square

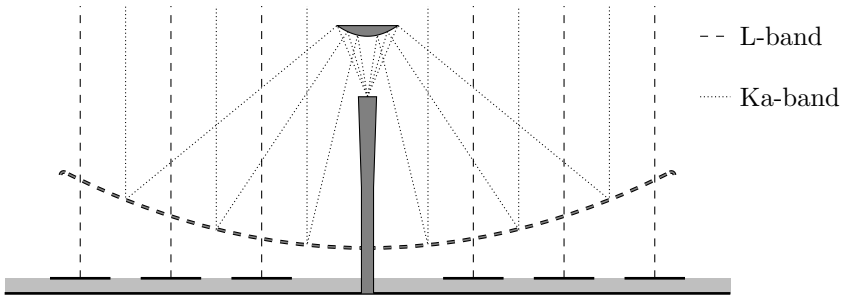


**Figure 3.2** A Ka-band FSS dual-reflector above an L-band patch array antenna.

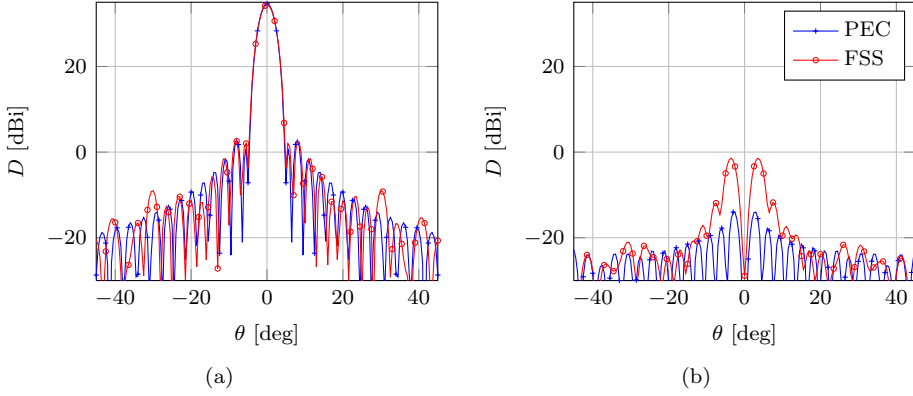


**Figure 3.3** Comparison of (a) RHCP and (b) LHCP directivity pattern of a 20 cm PEC and FSS reflector antenna at 30.0 GHz in the  $\phi = 45^\circ$  plane.

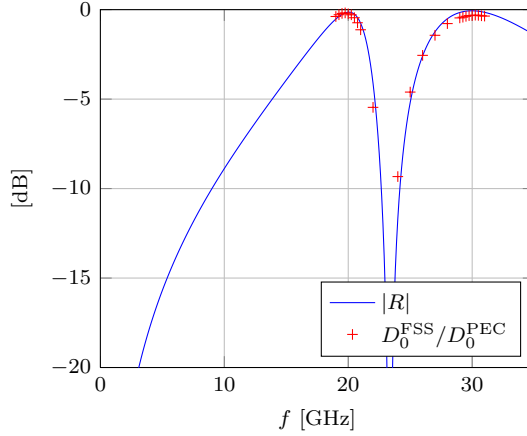


**Figure 3.4** Directivity degradation of FSS vs PEC reflector antenna and the planar FSS transmission coefficient vs frequency.

loop sides are non-orthogonal. This mostly affects the cross polarization and is worst in the depicted  $45^\circ$ -plane which is parallel to the diagonals of the FSS elements.

The frequency characteristics of the FSS reflector are shown in Figure 3.4, where the degradation in maximum directivity of the reflector antenna when us-

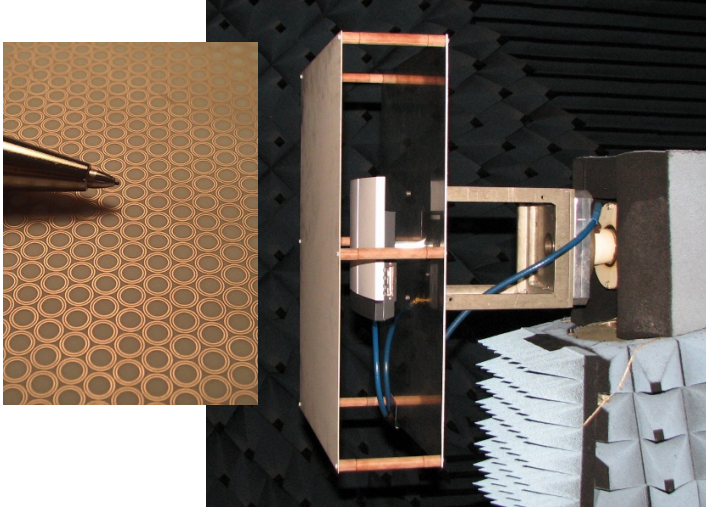


**Figure 3.5** Zoom of the FSS demonstrator and the measurement setup of the L-band antenna radiating through the FSS demonstrator.

ing an FSS instead of PEC reflector ( $D_0^{\text{FSS}}/D_0^{\text{PEC}}$ ) is compared to the magnitude of the reflection coefficient of an infinite planar FSS ( $|R|$ ). It is observed that frequency characteristics of the reflector agree with the characteristics of the planar FSS, which proves the applicability of the planar FSS design for shallow double-curved reflectors.

Since the investigated FSS consists of free-standing elements, the reflection coefficient at L-band is low (-25 dB). The reflection coefficient of a realizable printed FSS reflector will naturally be higher and depend on the permittivity of the chosen substrate.

Due to the electrically large dimensions of the entire FSS reflector consisting of electrically small elements, the numerical analysis by full-wave methods is limited to small reflectors. However, for large FSS reflectors it is proposed to implement a numerical equivalence formulation, as e.g. the Huygens's principle [82], which was out of the scope of this project.

### 3.4 Experimental Validation

In a masters project supervised during this project, a planar FSS demonstrator was designed and manufactured for identical frequency specifications [83].

The FSS is printed on a 1.52 mm thick Rogers 4003C substrate with  $\epsilon_r = 3.55$  and  $\tan \delta = 0.0027$ , consisting of concentric circular loops in a triangular grid. Numerical investigations of this FSS yields a maximum reflection coefficient of -14 dB over the L-band frequencies.

In this project, the L-band transparent properties of the FSS demonstrator were investigated experimentally, by measurements of an existing commercial L-band antenna<sup>2</sup> placed on a  $40 \times 60 \text{ cm}^2$  aluminum mounting plate. Measurements of this configuration has been carried out in the DTU-ESA Spherical Near-Field Antenna Test Facility, with and without the FSS in front of the antenna, as depicted in Figure 3.5. Four measurements were completed: one measurement without the FSS that serves as reference, and three measurements with the FSS with different distances to the antenna. The measured radiation patterns at 1,643 MHz are shown in Figure 3.6, where  $d$  is the distance from the L-band antenna to the FSS.

The maximum directivity of the reference antenna is 12.4 dBi and the cross polarization and side lobe levels are 14.1 and 19.1 dB below that<sup>3</sup>. For the three measurements including the FSS, the maximum directivity is within the range of 11.8 and 12.1 dBi, and both the maximum cross polarization and side lobe levels rise up to 1.6 dB compared to the reference.

Due to the finite reflection loss of the planar FSS, energy is indeed scattered off the FSS. This energy is thereafter reflected from the mounting aluminum plate and adds to the far-field in unpredictable directions. Due to the different measured distances between the L-band antenna and the FSS, the changes in the far-field are frequency dependent and likewise the optimum position of the FSS.

The reflection coefficient at the input of the L-band patch array antenna has been measured with a vector network analyzer (VNA), with the FSS in front of the antenna and without the FSS as reference, and is depicted in Figure 3.7. The reference measurement shows a reflection coefficient below -17.9 dB from 1,525.0 to 1,660.5 MHz. When the FSS is located in front of the antenna, here 38 mm between the antenna and the FSS, the maximum reflection coefficient is -16.6 dB.

The FSS demonstrator was designed with the aim of achieving best possible Ka-band performance, which induced the dense triangular grid as seen in Figure 3.5. The dense element grid improves the bandwidth in the reflecting

---

<sup>2</sup>The utilized antenna is a Thrane & Thrane Explorer 500 prototype including radome.

<sup>3</sup>The Thrane & Thane Explorer 500 is not designed to be mounted on such a mounting plate, thus the measured radiation pattern deviates from the designed and do not comply to any specifications.

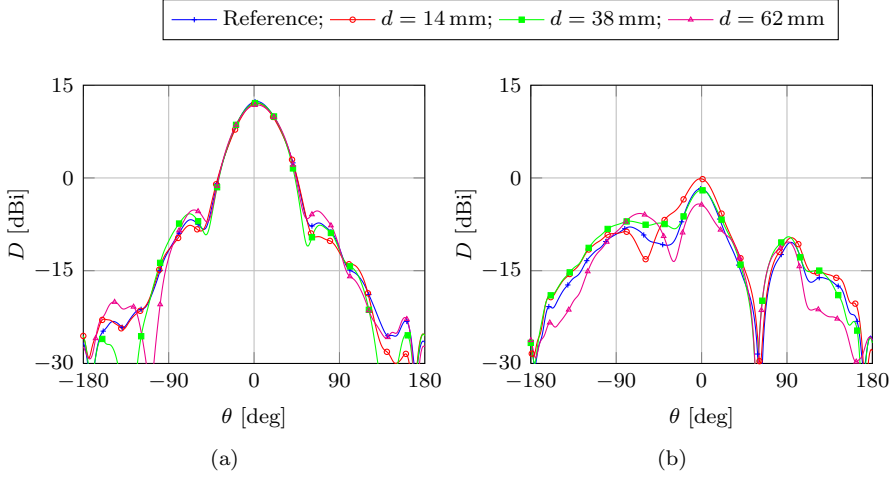


**Figure 3.6** Comparison of (a) RHCP and (b) LHCP directivity pattern of a commercial L-band satellite communication antenna, with and without the FSS demonstrator in front, at 1643 MHz in the horizontal plane.

frequency bands as well as the performance over different angles of incidence. However, these improvements are on the expense of higher reflection coefficient at L-band. Therefore, the impact of the FSS on both the L-band reflection coefficient and radiation pattern may be lowered by using a less dense element grid, or by using a dielectric substrate with lower permittivity such as the Rogers 5880 Duroid with  $\epsilon_r = 2.2$ .

The reader is referred to [83] for details on the Ka-band properties of the FSS demonstrator.

### 3.5 Summary

The use of FSSs for a hybrid L/Ka-band antenna has been studied. Elements for dual-band reflective properties have been considered and the concentric loop elements, square or circular, have demonstrated satisfying performance at both L- and Ka-band.

A Ka-band paraboloidal FSS reflector antenna was analyzed numerically by full-wave methods to investigate the applicability of planar FSS designs in a double-curved reflector. By adjusting the elements locally, the reflective properties of the FSS at 20 and 30 GHz was maintained. The co-polar far-field pattern of the FSS reflector antenna is comparable to that of an identical PEC reflector

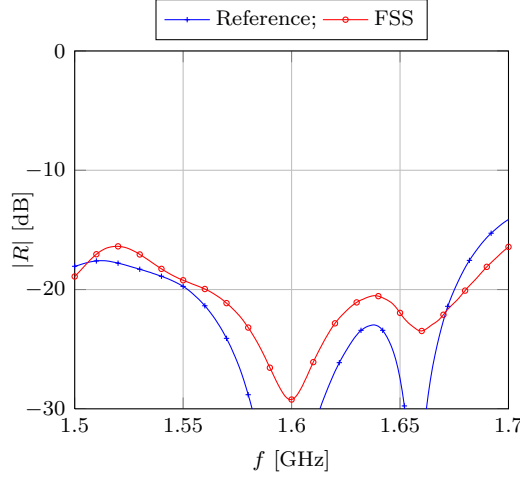


**Figure 3.7** Measured reflection coefficient of the L-band patch array antenna, for the distance  $d=38\text{ mm}$  between the L-band antenna and the FSS.

antenna. However, the cross-polarization is about 10 dB higher, which owes to the skewing of the elements in the projection of the FSS onto the paraboloidal surface, which should be corrected.

The L-band transparency of a Ka-band FSS was assessed experimentally, by measurements of a commercial L-band patch array antenna with and without a Ka-band FSS in front. The measurements show minor distortions in the L-band radiation pattern. The maximum directivity decreases by 0.3 to 0.5 dB depending on the distance between the L-band antenna and the FSS. Both the cross polarization and side lobe levels are increased by up to 1.6 dB. Small changes in the input impedance of the L-band antenna were observed. However, the observed changes may be acceptable if the L-band antenna is designed with margin to the specifications, and can be lowered by using low permittivity substrates or a less dense FSS element grid.

The FSS reflector antenna is proposed as solution for the hybrid L- and Ka-band antenna based on the electromagnetic properties that were demonstrated in this chapter. However, the major challenge of the FSS reflector antenna remains, which is the practical challenges in the manufacture of a double-curved FSS. A survey on manufacturing techniques was out of the scope of this project and should therefore be assessed.





## REFLECTARRAY ANTENNAS

---

Given the promising features of FSS antennas that were presented in Chapter 3, an FSS-backed reflectarray antenna has been developed and is presented in this chapter. The reflectarray consists of concentric dual split-loop elements. The characteristics of the element are given, followed by the outline of an iterative design procedure that has been developed for this specific element. Using this procedure, two prototype reflectarray antennas have been designed and manufactured. The antennas have been measured at the DTU-ESA Spherical Near-Field Antenna Test Facility and the results are presented and discussed.

Most of the work that is presented in this chapter has been documented in [J1,J2] and [C2,C3], which are found in the last part of this thesis.

### 4.1 Background

The reflectarray antenna combines desirable features from the reflector antenna and the phased array antenna. Particularly, printed reflectarray antennas have been subject to extensive research due to its low weight and ease of manufacturing. A reflectarray antenna consists of a surface of scattering elements and an illuminating antenna. Contrary to the conventional reflector antenna, the reflectarray is designed by adjusting the individual scattering elements to reflect the illuminating field with a desired phase to form e.g. a planar phase front in a given direction [30, 31].

Different design approaches for reflectarray antennas for widely separated frequencies, as here L- and Ka-band, have been used in the past by either using placing low-frequency elements above high-frequency elements in a multi-layer configuration [42, 52] or using interleaved elements on the same layer [46, 51, 52]. However, by the use of an FSS ground-plane instead of a conventional solid ground-plane enables cascading of multiple reflectarrays [84–89]. In this way, the L-band antenna may be designed using conventional antenna technology,

e.g. a patch array antenna, which may be located behind and radiate through the Ka-band reflectarray.

The separation of the Ka-band RX and TX frequencies presents a challenging task, since the planar reflectarray antenna is considered a narrow-band antenna [30]. The bandwidth of reflectarray antennas is limited by two factors: the differential spatial phase delay over the aperture, i.e. the different path lengths from the feed antenna to the reflectarray elements, and the bandwidth of the reflectarray elements [32]. The differential spatial phase delay can be mitigated by the use of true-time delay lines [35] or curved or multi-facet reflectarray [90–93]. However, for multi-band applications it is advantageous to adjust the reflection phase separately in each frequency band. Different reflectarray element topologies exist for this purpose, such as interlaced dipoles [39], interlaced crossed dipoles [40, 44], interlaced split-loops [48], stacked patches [38], and stacked loop elements [41–43] etc. Interleaved grids of different reflectarray elements have also been proposed [51, 52].

Depending on the angles of incidence, the inter-element spacing of the FSS and reflectarray elements should be less than 0.6 to 0.7 wavelengths to avoid grating lobes [30]. Also, recent literature suggest that small inter-element spacing entails larger frequency bandwidth, thus a small inter-element spacing is desired [34]. Though interlaced elements can be employed in the present study, it is preferred to utilize a compact reflectarray element that facilitates simultaneous phase adjustment at 20 and 30 GHz.

## 4.2 Antenna Concept

For printed reflectarray antennas, the scattering elements are manufactured by using printed circuit board (PCB) fabrication techniques. Usually, single layer reflectarray antennas comprise of a top layer where the scattering elements are located, a chosen dielectric substrate, and the bottom layer being a solid copper ground-plane. However, the PCB fabrication technique enables the use of an FSS ground-plane on the bottom layer. Designing the FSS to be reflective at the reflectarray operating frequency makes it possible to place a second antenna behind and radiate through the reflectarray, as the FSS reflector presented in Chapter 3. The reflectarray antenna with an FSS ground-plane, hereafter denoted FSS-backed reflectarray, in front of an L-band patch array antenna is depicted in Figure 4.1.

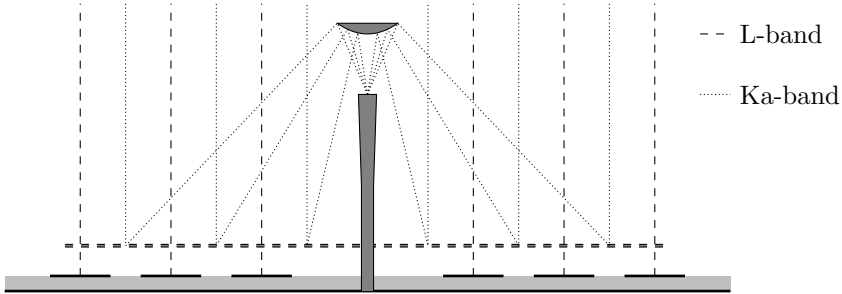


**Figure 4.1** A Ka-band FSS-backed reflectarray above an L-band patch array antenna.

### 4.3 Reflectarray Analysis

The individual reflectarray elements are designed to reflect the illuminating field with a given polarization and phase to obtain a desired far-field radiation pattern, thus the reflectarray elements are inherently aperiodic. Different methods can be used to design and analyze reflectarray antennas, and the choice is usually a trade-off between accuracy and numerical efficiency. Full-wave solvers such as Ansys HFSS, CST Microwave Studio, or similar software packages have the benefit of including the entire antenna in a full-wave analysis and thereby accounting for the mutual coupling of the actual aperiodic elements and the finite size of the reflectarray. However, this requires extensive CPU power and memory, and the computation time renders optimization of the antenna infeasible. This may be avoided by approximating the reflected field of the individual reflectarray elements as the reflection of an infinite array of identical elements [94], which reduce the domain of the analysis to each element independent of the other. This method is also known as the local periodicity (LP) assumption.

In this project, it was chosen to use the commercial software Ansys Designer to design and analyze the reflectarray elements. The software is a planar electromagnetic simulator based on the MoM and is computationally efficient for printed reflectarray elements. Each reflectarray element is simulated using periodic boundary conditions and plane wave excitation, thus emulating as if it was located in an infinite array of identical elements.

The far-field radiation of the reflectarray antenna is calculated using the equivalent currents technique [95, technique II], i.e. by integrating both electric and magnetic equivalent currents in the aperture. To do this, the reflectarray aperture is divided into unit cells where the reflected field is found by interpolation in a lookup table which is pre-computed for a finite set of element geometries and angles of incidence. A design tool has been implemented in a

numerical code that utilizes the pre-computed reflection coefficients to synthesize the reflectarray layout.

The developed code has been verified against several reflectarray antenna samples, and the details are found in Appendix A.

#### 4.4 Reflectarray Element

To facilitate simultaneous phase adjustment in the two separate RX and TX frequency bands, a concentric dual split-loop (CDSL) element, depicted in Figure 4.2, has been designed and investigated<sup>1</sup>. The element is characterized by the radii  $r_o$  and  $r_i$ , respectively, measured from the center to the outside of the conductor, the rotation angles  $\psi_o$  and  $\psi_i$ , the gap sizes  $g_o$  and  $g_i$ , and equal conductor width  $w$ .

A concentric circular loop element is utilized in the design of a FSS ground-plane, which is also depicted in Figure 4.2. The FSS element is characterized by the radii of the outer and inner loops,  $r_o^{\text{fss}}$  and  $r_i^{\text{fss}}$ , respectively.

The element utilizes the variable rotation technique (VRT) to adjust the phase of reflected circularly polarized fields at 20 and 30 GHz, simultaneously. The VRT requires the orthogonal linear reflection coefficients to be of equal amplitude and  $180^\circ$  out of phase, which is obtained by optimizing the gaps of the dual split-loops accordingly. In this case, a pure co-polar reflection coefficient is achieved, i.e. LHCP to LHCP ( $R_{\parallel}$ ) at 20 GHz and RHCP

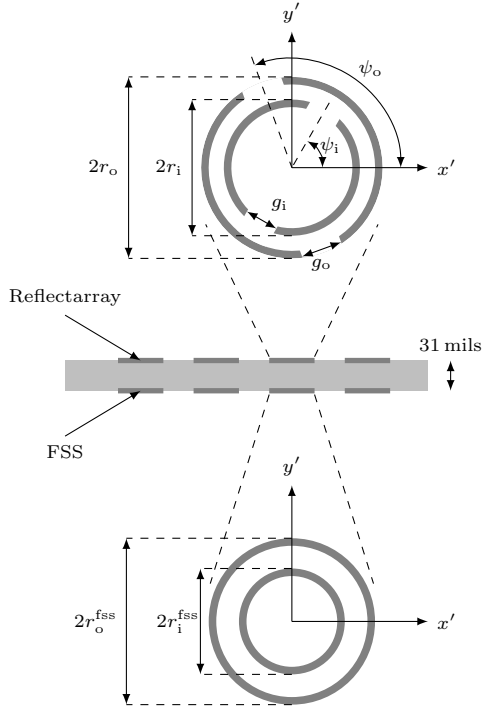


**Figure 4.2** Geometry of the FSS-backed CDSL element.

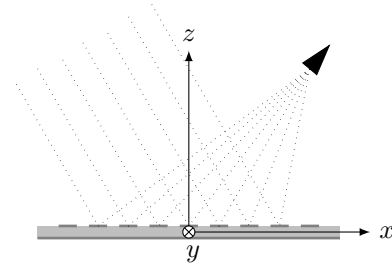
<sup>1</sup>The CDSL element has later in this study been found depicted in [30, p. 122] and [96, p. 57], however, without any investigations of this concentric topology.

**Table 4.1** *Parameters of the CDSL element with solid and FSS ground-plane.*

	$r_o$	$r_i$	$w$	$r_o^{\text{fss}}$	$r_i^{\text{fss}}$
Solid ground-plane	2.05 mm	1.40 mm	0.20 mm	-	-
FSS ground-plane	2.30 mm	1.90 mm	0.20 mm	2.10 mm	1.60 mm

to RHCP ( $R_{\text{rr}}$ ) at 30 GHz. For a circularly polarized incident field, then by rotating the element by  $\psi$  degrees, the reflected field is delayed or advanced by  $2\psi$  degrees, depending on the rotation of the incident field [97]. For the CDSL element, the outer and inner dual-split loops may be rotated independently, and each of these determine the reflection phase at 20 and 30 GHz, respectively. The reader is referred to Appendix B for more details on the VRT.

The radii of the designed CDSL element were adjusted to maximize the co-polar reflection coefficient, with solid and FSS ground-plane, separately. This adjustment was carried out considering a reduced set of rotation element rotation angles prior to the analysis of all rotation angles, and the final dimensions are given in Table 4.1. The reflection coefficients of the element change when the dual split-loops are rotated, thus the optimization of  $g_o$  and  $g_i$  is carried out for  $(\psi_o, \psi_i) \in [0^\circ, 10^\circ, \dots, 180^\circ]$ . The optimization is carried out using the Quasi Newton optimization in Ansys Designer to suppress the magnitude of the cross-polar reflection coefficients at the center frequencies of the RX and TX frequency bands, i.e. LHCP to RHCP ( $R_{\text{rl}}$ ) at 19.95 GHz and RHCP to LHCP ( $R_{\text{lr}}$ ) at 29.75 GHz. The plane wave incidence angles are  $\phi = 0^\circ$  and  $\theta = 30^\circ$ , which are the incidence angles towards the center of the prototype reflectarrays, see Figure 4.3.

**Figure 4.3** *Antenna configuration and coordinate system of the prototype reflectarray antennas.*

#### 4.4.1 CDSL with Solid Ground-Plane

For the CDSL element with solid ground-plane, the reflection coefficients at 20 GHz were found to be almost independent of the rotation of the inner dual split-loop. This feature has been utilized to first optimize  $g_o$  to suppress  $R_{\text{rl}}$  at 19.95 GHz using an approximate value of  $g_i$ , and thereafter optimize  $g_i$  to suppress  $R_{\text{lr}}$  at 29.75 GHz using the optimized value of  $g_o$ . For all combinations

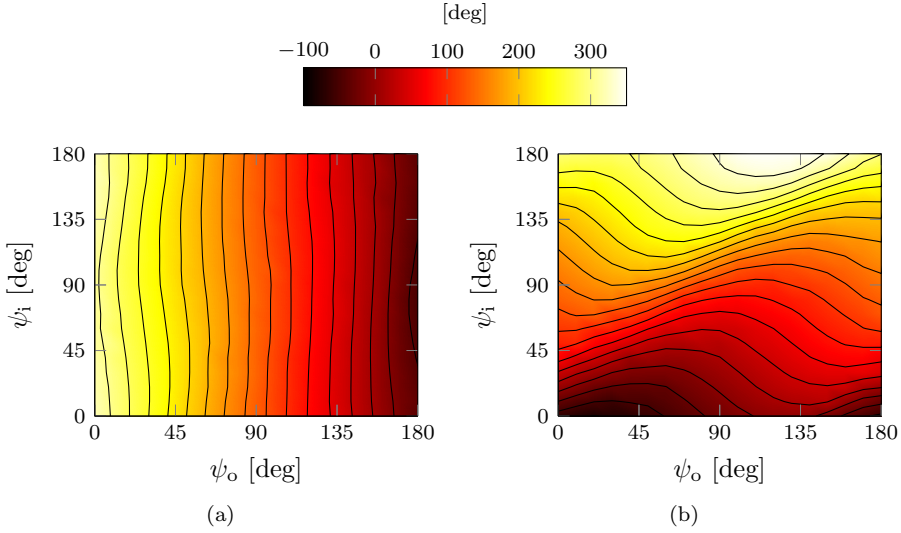


**Figure 4.4** 2-dimensional phase curves for the CDSL element with solid ground-plane. Phase of (a)  $R_{||}$  at 19.95 GHz and (b)  $R_{tr}$  at 29.75 GHz, for the incidence angles  $\phi = 0$  and  $\theta = 30^\circ$ .

of  $\psi_o$  and  $\psi_i$ , the magnitudes of the cross-polar reflection coefficients have been suppressed to a level in the order of -36 and -27 dB, at 19.95 and 29.75 GHz, respectively. The magnitude of the co-polar reflection coefficient at 19.95 GHz is approximately -0.2 dB, which owes to dielectric and conductor losses. At 29.75 GHz, the magnitude of the co-polar reflection coefficient varies from -0.4 to -0.1 dB.

Two-dimensional phase curves at 19.95 and 29.75 GHz are shown in Figure 4.4, where the important features of this elements are observed. Firstly, it is observed that a full 360° phase range at 19.95 GHz is obtained by adjusting  $\psi_o$ , and similarly at 29.75 GHz by adjusting  $\psi_i$ . Secondly, it is observed that the phase of  $R_{||}$  at 19.95 GHz is almost independent of  $\psi_i$ . This allows the final reflectarray antenna to be designed by adjusting  $\psi_o$  of all elements to obtain the desired radiation pattern at 19.95 GHz, and subsequently adjusting  $\psi_i$  to obtain the desired radiation pattern at 29.75 GHz.

More details on the CDSL element with solid ground-plane are found in [C2,C3,J1].

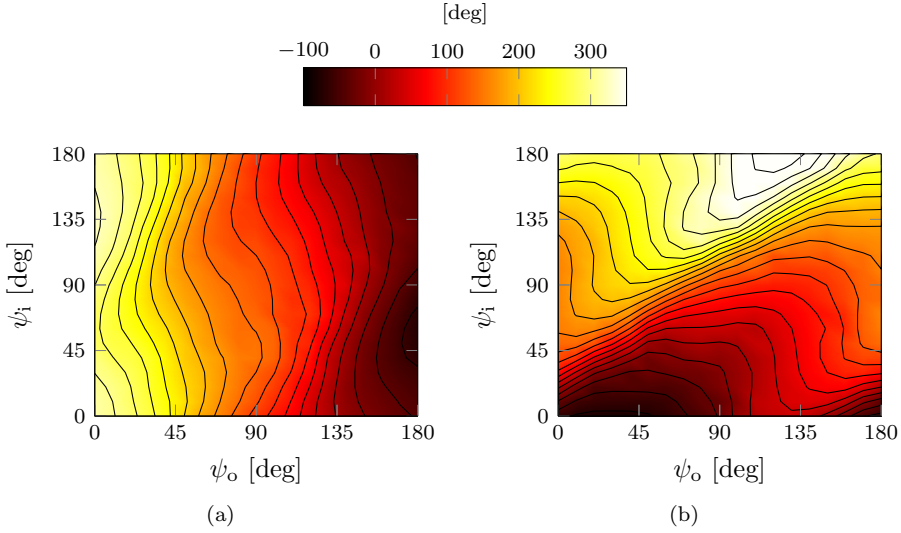


**Figure 4.5** 2-dimensional phase curves for the CDSL element with FSS ground-plane. Phase of (a)  $R_{||}$  at 19.95 GHz and (b)  $R_{tr}$  at 29.75 GHz, for the incidence angles  $\phi = 0$  and  $\theta = 30^\circ$ .

#### 4.4.2 CDSL with FSS Ground-Plane

For the reflectarray with FSS ground-plane, the radii of the outer and inner split-loops were changed from the values of the solid ground-plane design. A manual parametric study was conducted to find the radii that yield maximum magnitude of the co-polar reflection coefficient for multiple rotation angles<sup>2</sup>, see Table 4.1. As for the CDSL element with solid ground-plane, the element was thereafter optimized to maximize the magnitude of the co-polar reflection coefficient by adjusting  $g_o$  and  $g_i$ .

The two-dimensional phase-curves of the optimized FSS-backed CDSL element are depicted in Figure 4.5, where a full  $360^\circ$  phase range of  $R_{||}$  at 19.95 GHz is obtained for  $\psi_o \in [0^\circ; 180^\circ]$ , and similarly for  $R_{tr}$  at 29.75 GHz for  $\psi_i \in [0^\circ; 180^\circ]$ . In contrast to the CDSL element with solid ground-plane, the co-polar reflection coefficient at 19.95 GHz is found to change significantly with  $\psi_i$ , which entails that the reflectarray cannot be optimized for 30 GHz radiation by rotation the inner split-loops without affecting the 20 GHz radiation. This,

<sup>2</sup>The radii of the outer and inner split-loop may be included as optimization variables, but this increases the optimization time significantly and was not possible within the allocated time frame.



however, is handled by a developed iterative design procedure.

With an optimum design, all power should be reflected by the FSS-backed reflectarray, as in the case of a conventional solid ground-plane. For the present element design,  $|R_{ll}|$  is in the range of -0.7 to -0.3 dB at 19.95 GHz. At 29.75 GHz,  $|R_{rr}|$  is in the order of -0.5 dB for most rotation angles. The average cross-polar reflection, i.e.  $|R_{rl}|$  at 19.95 GHz and  $|R_{lr}|$  at 29.75 GHz, is below -20 dB. However, for  $\psi_o \approx \psi_i$ ,  $|R_{rr}|$  decreases to -1.5 dB. This means that part of the power of the incident plane wave is transmitted through the reflectarray and will scatter off the reflectarray support structure. It is expected that the element may be further optimized by including more geometry variables, such as  $r_o$  and  $r_i$ , as optimization variables, but this was not possible within the allocated time frame.

## 4.5 Reflectarray Design Procedure

For pencil beam reflectarray antenna designs, the elements must be adjusted such that the reflected field over the entire antenna aperture forms a collimated beam in the desired direction. In the literature, the feed antenna is often assumed as a  $\cos^n \theta$  modulated spherical wave [33], i.e. the feed antenna has a true phase center. However, the position of the phase center of practical feed antennas often varies in plane of observation and over frequency. To obtain an optimum reflectarray design, the near-field of the specific feed antenna, obtained either by measurements or an accurate simulation tool, should be used [98], and this approach has been implemented in the developed code.

For the CDSL element with solid ground-plane, it was found that the reflection coefficients were determined by  $\psi_o$  and the adjustment of  $\psi_i$  had negligible effects. Given these characteristics, a sequential design procedure was developed that consists of the following steps:

1. The reflectarray unit element is optimized and the scattering matrices are stored
2. The design tool is initialized with  $\psi_o = \psi_i = 0^\circ$  for all elements
3. A 1-dimensional phase-curve of  $R_{ll}$  at 19.95 GHz is generated using local values of  $(\phi, \theta, \psi_i)$ , from which  $\psi_o$  is determined
4. A 1-dimensional phase-curve of  $R_{rr}$  at 29.75 GHz is generated using local values of  $(\phi, \theta, \psi_o)$ , from which  $\psi_i$  is determined
5. The scattered aperture field is determined by interpolation of the reflection matrix

**Table 4.2** *Reflectarray antenna data for Prototype 1 and 2.*

RX frequencies	19.7 GHz – 20.2 GHz LHCP
TX frequencies	29.5 GHz – 30.0 GHz RHCP
Reflectarray dimensions	400 mm $\times$ 400 mm
Feed distance to center of array	300 mm
Feed offset angle	$\phi = 0^\circ, \theta = 30^\circ$
Direction of mainbeam	$\phi = 180^\circ, \theta = 30^\circ$

6. The radiated far-field is calculated by equivalent currents technique

Since the 20 GHz reflection coefficients of the CDSL element with solid ground-plane does not change when adjusting  $\psi_i$ , the 20 GHz reflectarray antenna radiation does not either. However, for the FSS-backed CDSL element the 20 GHz reflection coefficients depend on both  $\psi_o$  and  $\psi_i$ , thus the 20 GHz radiation pattern is impaired by the 30 GHz design in Step 4. To improve this, Step 3 and 4 may be repeated to form an iterative design procedure. For the FSS-backed CDSL reflectarray antenna design, improvements of 0.6 dB higher peak directivity and lower cross polarization and side lobes are obtained [J2].

## 4.6 Prototype Antennas

Using the developed design tool, two prototype antennas have been manufactured: Prototype 1 is designed using the CDSL element on a solid ground-plane, and Prototype 2 with the FSS-backed CDSL elements.

The reflectarray antennas are offset fed with a collimated beam in the specular direction to avoid blockage and scattering from the feed antenna and the support structure. The dimensions of both prototype reflectarrays are 400  $\times$  400 mm<sup>2</sup>, and the distance to the feed antenna is 300 mm with an offset angle of  $\phi = 0^\circ, \theta = 30^\circ$ . The data are summarized in Table 4.2.

A corrugated horn antenna with integrated diplexer and polarizer is used as feeding antenna. However, due to a problem with higher-order modes being excited in the available version of the feeding horn antenna, the horn has been modeled in the commercial software CHAMP [99] where only the fundamental mode is excited. This model has been used to calculate the near-field of the feeding horn antenna, which is used for the reflectarray design. The feed antenna has not been optimized for this particular application, however, the focal length of the reflectarray has been chosen such that the illumination level along the edge of the reflectarray varies from approximately  $-20$  to  $-5$  dB relative to the maximum in the reflectarray aperture.

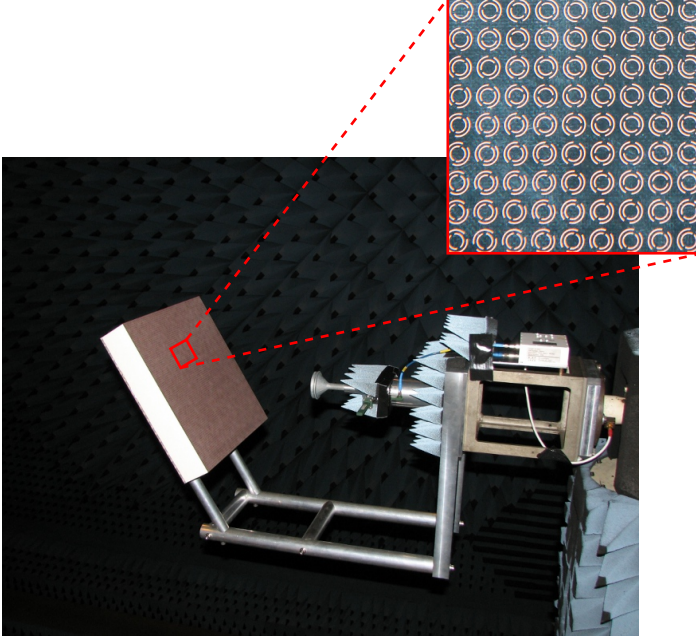


**Figure 4.6** *The Prototype 1 reflectarray antenna in the DTU-ESA Spherical Near-Field Antenna Test Facility. The measurement coordinate system is located with the z-axis in the direction of the main beam and the x-axis in the plane that contains the main beam and the feed antenna.*

The antenna support structure has been manufactured by the mechanical workshop at the Electromagnetic Systems (EMS) group at DTU Electro. The reflectarray prototypes have been measured at the DTU-ESA Spherical Near-Field Antenna Test Facility [100] with a  $1\sigma$  uncertainty of 0.1 dB on the maximum directivity.

The assembled Prototype 1 reflectarray antenna is depicted in Figure 4.6, mounted in the DTU-ESA Spherical Near-Field Antenna Test Facility. To increase repeatability and for comparison purposes, both reflectarray antennas are mounted identically. Since the FSS-backed reflectarray elements are optimized in a free-standing configuration, i.e. in free space without support structure, a  $400 \times 400 \text{ mm}^2$  block of 70 mm thick Rohacell HF 51, with  $\epsilon_r = 1.08$  and  $\tan \delta = 0.0021$ , is mounted between the reflectarray and the support structure using few small patches of double adhesive tape.

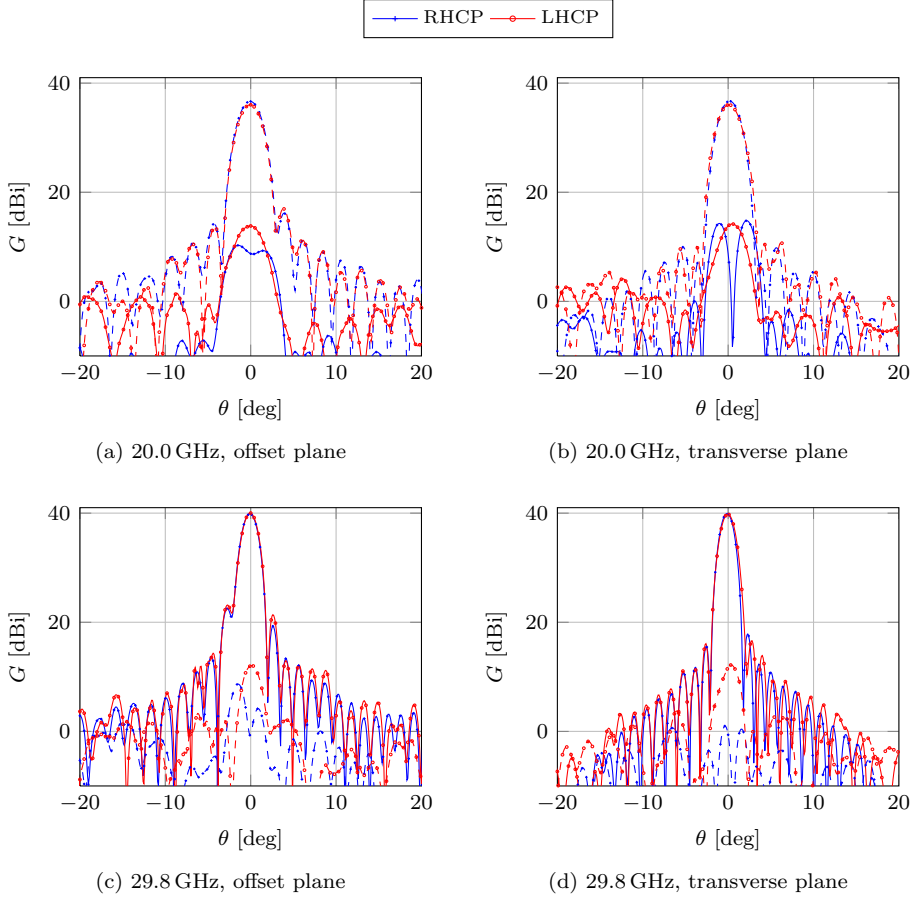


**Figure 4.7** Simulated and measured gain patterns of Prototype 1 reflectarray antenna at 20.0 and 29.8 GHz.

#### 4.6.1 Reflectarray with Solid Ground-Plane

The first prototype reflectarray antenna was manufactured to validate the performance of the CDSL elements and the design tool, without the effects of an FSS ground-plane. The simulated and measured gain patterns of the reflectarray antenna are shown in Figure 4.7.

At 20.0 GHz, the measured maximum gain is 35.8 dBi and the maximum cross-polarization level is 21.8 dB below that. The side lobe level is 19.1 dB below the maximum gain. The simulated maximum gain is 0.8 dB higher than

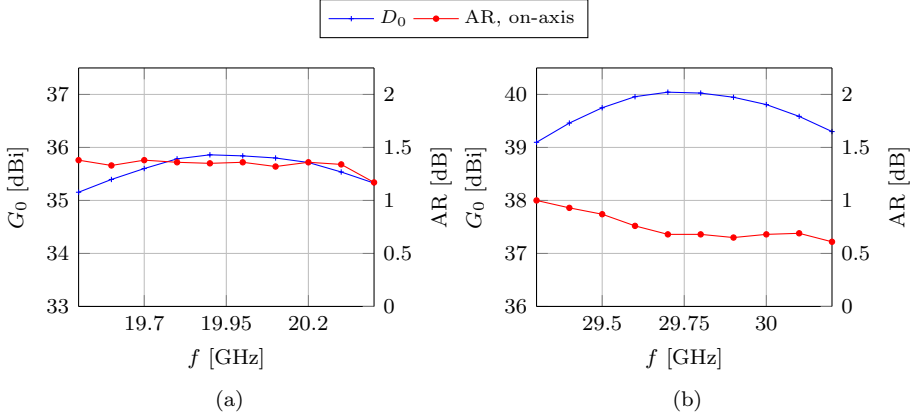


**Figure 4.8** Co-polar gain and on-axis AR of the Prototype 1 reflectarray over the (a) RX and (b) TX frequency bands.

the measurements, but does not include losses in the feed antenna and polarizer. The first side lobes agree within 0.7 dB, while the measured maximum cross polarization is approximately 3 dB higher than the simulations.

At 29.8 GHz, a measured maximum gain of 40.0 dBi is obtained. The cross-polarization level and side lobe level are 27 dB and 17 dB below this. The simulations agree well, where the maximum gain is 0.2 dB higher. The first side lobes and maximum cross polarization levels are in the order of 2 to 3 dB lower than the measured. The asymmetric side lobes observed in both simulations and measurements in Figure 4.7c and Figure 4.7d are caused by higher-order modes being excited in the feed antenna polarizer, which causes the incident field to be asymmetric.

Though the reflectarray support structure is rigid and accurately aligned, the reflectarray surface has been found to move up to 1 mm from the design due to structure deformation, when it is rotated in the spherical near-field measurement facility. This means that the feed is slightly offset from the design position, which causes changes in the radiation pattern such as the higher measured on-axis cross polarization. However, the effect of the deformation is most apparent at 29.8 GHz in the transverse plane in Figure 4.7d. Here, the position of the side lobes on the left side of the simulated and measured radiation patterns coincide. However, the side lobes on the right side appear to be shifted by  $0.3^\circ$  due to the deformation of the support structure.

The spherical near-field measurements were conducted in steps of 100 MHz,

and the co-polar gain and on-axis axial-ratio (AR) are depicted in Figure 4.8. It is seen that the minimum peak gain within 19.7 to 20.2 GHz is 35.6 dBi, while between 29.5 and 30.0 GHz the minimum peak gain is 39.8 dBi.

The antenna loss, measured at the input of the diplexer, is in 0.5 and 0.3 dB in the RX and TX frequency bands, respectively. The magnitude of the co-polar reflection coefficients of the CDSL element, when optimized to cross-polar reflection coefficients in the order of -30 dB, is in the order of -0.1 to -0.4 dB [C3]. In the measurements, losses in the horn and polarizer are included, which agrees with the measured losses being slightly higher and the element losses. The aperture illumination efficiency is in the range of 53 to 63 % over both frequency bands of interest [J1].

#### 4.6.2 Reflectarray with FSS Ground-Plane

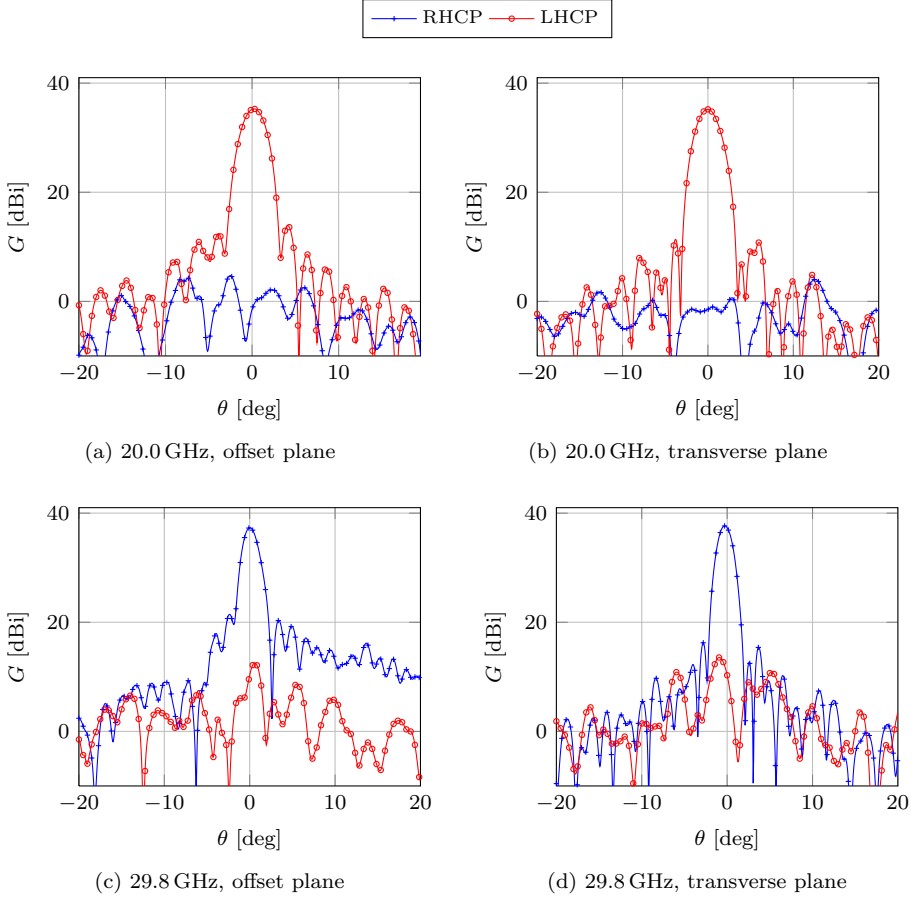
The measured radiation patterns of the reflectarray at 20.0 and 29.8 GHz are depicted in Figure. 4.9 in the offset and transverse plane<sup>3</sup>. At 20.0 GHz, the maximum gain is 35.3 dBi. The side lobe and cross polarization levels are 21.4 dB and 30.6 dB, respectively, below the maximum gain. The antenna loss is 1.1 dB with the reference plane at the input of the diplexer. At 29.8 GHz, the maximum gain is 37.7 dBi, and the side lobe level and cross polarization levels are 16.2 dB and 24.1 dB below that. Here, the antenna loss is approximately 0.8 dB.

Figure 4.10 presents the co-polar gain and on-axis AR over the RX and TX frequency bands. In the RX frequency band, the minimum peak gain is 34.9 dBi and the AR is below 0.8 dB. The aperture illumination efficiency is 53 to 57 %, which is similar to the performance of the reflectarray with solid ground-plane. In the TX frequency band, the minimum peak gain is 36.7 dBi, and the AR is below 1.8 dB. The aperture illumination efficiency is in the range of 32 to 48 % [J2].

It is observed that the co-polar gain varies more than 1.5 dB in the TX frequency band, which also cause the low aperture efficiency of 32 %. This owes to power being transmitted through the FSS ground-plane, which is then reflected from the aluminum mounting plate behind the Rohacell. This power is then scattered in different directions through the sides of the Rohacell and adds to the far-field in different phases depending on the frequency. Thus, the reflectarray performance in the TX frequency band should be improved by further optimization of the reflectarray and FSS elements, to maximize the magnitude of the co-polar reflection coefficient, i.e.  $|R_{rr}|$  at 29.75 GHz. This may be achieved by including the radii of the both the split-loops and the radii of the FSS loops into optimization, as described in Section 4.4.2.

---

<sup>3</sup>Accurate simulations of the FSS-backed prototype reflectarray antenna were not carried out at the measured frequencies due to the limited time frame.



**Figure 4.9** Measured gain patterns of Prototype 2 reflectarray antenna at 20.0 and 29.8 GHz.

#### 4.6.2.1 L-Band Measurement

To examine the L-band transparency of the FSS-backed reflectarray, the Cobham Satcom Explorer 500 antenna was measured with and without the reflectarray in front, similarly to the investigations described in Chapter 3. A dedicated measurement setup was constructed where the reflectarray is supported by Rohacell 51 HF to minimize scattering of the support structure. The setup is depicted in Figure 4.11. The measurement of the L-band antenna without the FSS-backed reflectarray in front serves as reference when observing the influence of the FSS-

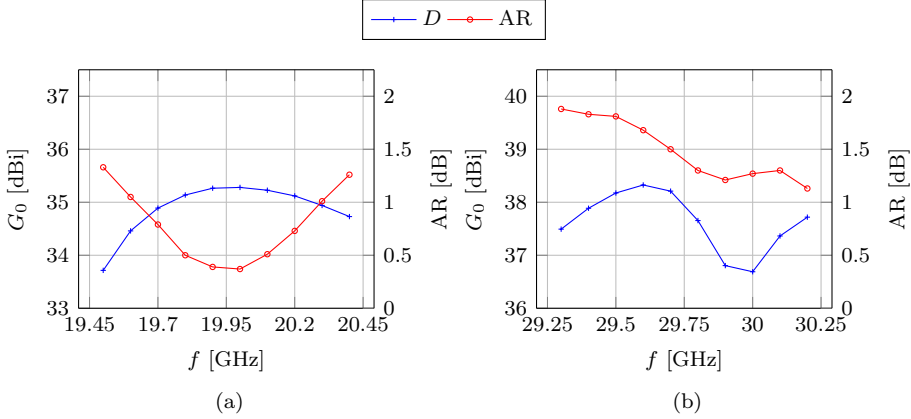


**Figure 4.10** Co-polar gain and on-axis AR of the Prototype 2 reflectarray at the (a) RX and (b) TX frequency band.

backed reflectarray.

The radiation patterns of both measurements, at 1,643 GHz in the  $\phi = 0^\circ$  plane, are shown in Figure 4.12. The maximum directivity of the L-band antenna with the FSS-backed reflectarray in front is 12.2 dBi, which is 0.1 dB lower than the reference. The maximum cross polarization level is 13.3 dB below the maximum directivity, which is 0.8 dB higher than the reference. The side lobes change asymmetrically such that the side lobe level at  $\theta = -70^\circ$  rises by 0.7 dB, while the side lobe level at  $\theta = 70^\circ$  decreases by 0.4 dB. Similar changes in the radiation pattern was observed in the entire far-field sphere.

The measurements were conducted from 1,500 to 1,700 MHz, and the directivity varies within  $\pm 0.15$  dB of the reference, and the maximum cross polarization level varies less than  $\pm 2.5$  dB.

The reflection coefficient at the input of the L-band antenna has been measured with a VNA, with and without the FSS-backed reflectarray in front, and is shown in Figure 4.13. Within the frequency band of interest, 1,525.0 to 1,660.5 MHz, the maximum reflection coefficient with the reflectarray in front is -17.0 dB, which is slightly higher than the -17.9 dB without the reflectarray in front. Overall, the changes in both radiation pattern and reflection coefficient are small, which validates the L-band transparency of the FSS-backed reflectarray antenna.



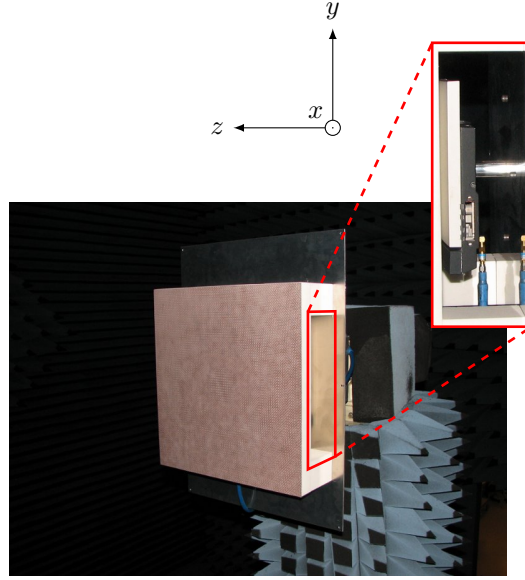


**Figure 4.11** *L-band measurement setup to assess the transparency of the FSS-backed reflectarray. The measurement coordinate system is located with the  $z$ -axis orthogonal to the reflectarray surface, and the  $x$ -axis in the horizontal plane.*

## 4.7 Summary

A hybrid L/Ka-band antenna concept that consists of a Ka-band FSS-backed reflectarray antenna above an L-band patch array antenna was demonstrated.

To accommodate the widely separated Ka-band RX and TX frequencies with opposite sense of circular polarization, the CDSL element was designed and investigated. The element utilizes the VRT to enable the simultaneous phase adjustments at 20 and 30 GHz. The element geometry was optimized to minimize the magnitude of the cross-polar reflection coefficient, and a full  $360^\circ$  phase range can be covered at both 20 and 30 GHz.

An iterative design procedure was implemented to improve the reflectarray design. Using this approach, two prototype reflectarray antennas were designed. The first, using a conventional solid ground-plane, validates the element design and the reflectarray design. The prototype reflectarray antenna has aperture illumination efficiencies within the range of 53 to 63 % are achieved over the two frequency bands of interest.

The second reflectarray prototype was designed using the CDSL element and

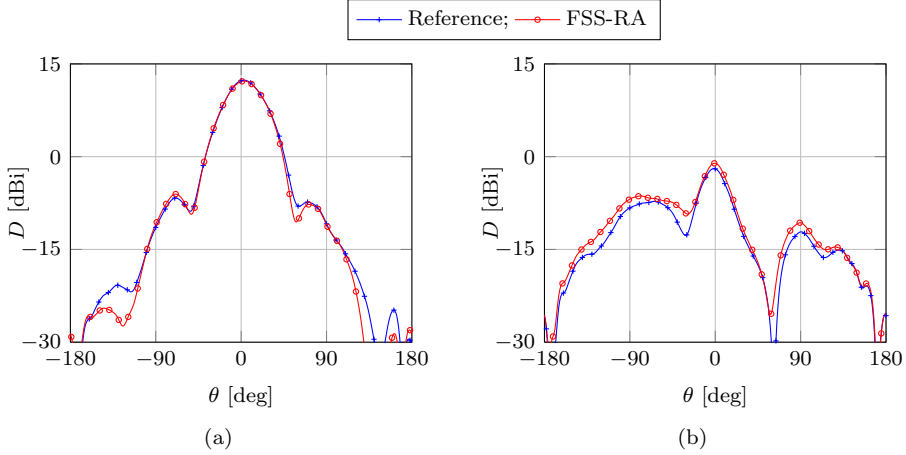


**Figure 4.12** Comparison of (a) co- and (b) cross-polar radiation pattern of a commercial L-band satellite communication antenna, without the reflectarray (w/o RA) and with the reflectarray (w/ RA) in front, at 1643 MHz in the  $\phi = 0^\circ$  plane.

an FSS ground-plane. Due to a limited time frame, a non-optimal element design was used for the FSS-backed reflectarray antenna. Therefore, the performance of this antenna was inferior to the performance of the reflectarray with solid ground-plane, and the aperture illumination efficiency was between 32 and 48 % over the two frequency bands of interest. However, the prototype antenna validates and demonstrates the capabilities of the proposed antenna concept. It is expected that further optimization of the reflectarray element can improve the performance of the final antenna design.

The L-band transparency of the FSS-backed reflectarray was assessed by measurements of a commercial L-band antenna radiating through the reflectarray prototype. The results demonstrate negligible influence on both the antenna radiation and input impedance, which validate the applicability of the proposed antenna configuration.

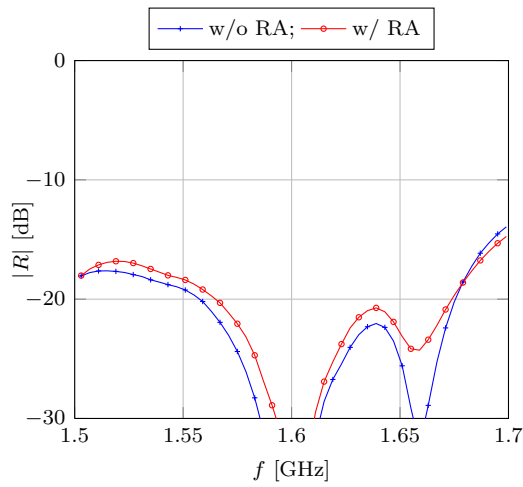


**Figure 4.13** Measured reflection coefficient of the L-band patch array antenna, without the reflectarray (w/o RA) and with the reflectarray (w/ RA) in front.

## CONCLUSIONS

---

In this study, antennas for simultaneous operation in L-band (1,525.0–1,660.5 MHz) and Ka-band (19.7–20.2 GHz and 29.5–30.0 GHz) satellite communication services have been investigated. The main outcomes of the study are three antenna concepts that are recommended for further development.

The first antenna proposal is a combined L-/Ka-band single-/dual-reflector. The Ka-band antenna is a conventional dual-reflector antenna, however, the L-band antenna constitute a single-reflector that is fed by a backfire monofilar helical antenna that is mounted on the shadow side of the Ka-band sub-reflector. The backfire helical antenna and the complete antenna system have been investigated by method of moments (MoM) and physical optics (PO) using the commercially available software GRASP. It was found that the helical antenna provides backfire radiation over a broad span of its associated geometrical parameters, which enables the size of the helical antenna to be adjusted to the approximate size of the Ka-band sub-reflector. The radiation patterns of the L-band single-reflector antenna demonstrate excellent performance, with an aperture illumination efficiency that exceeds 70 %. Thereafter, it was shown that the helical antenna introduces negligible scattering at Ka-band, with a 0.05 dB degradation in maximum directivity and a 0.6 dB increase in both side lobe and cross polarization levels for the Ka-band antenna. The key feature of the combined L/Ka-band single/dual-reflector antenna is the possibility of using conventional reflector antenna technology and design tools for the Ka-band antenna, and its performance is almost unaffected by the introduction of the L-band antenna.

For the second antenna proposal, a Ka-band paraboloidal frequency selective surface (FSS) reflector has been examined. This antenna enables the use of conventional L-band antennas located behind and radiating through the FSS reflector. Different FSSs have been designed to be reflective at Ka-band, while being transparent at L-band, i.e. the magnitude of the co-polar reflection coefficient is -0.3 dB and -20 dB, respectively. A free-standing planar FSS was

subsequently projected onto a paraboloidal reflector shape and the antenna was investigated by MoM. The results show satisfying performance and are consistent with the planar investigations, with a 0.3 dB drop in maximum directivity at Ka-band. The L-band transparency was examined by measurements of the radiation pattern of a commercial L-band antenna that radiates through a planar FSS prototype. The measurements were conducted at the DTU-ESA Spherical Near-Field Antenna Test Facility, and the results show small impact on the L-band antenna impedance and radiation properties, where the decrease in maximum directivity is in the order of 0.5 dB.

To circumvent the practical difficulties in manufacturing of a double-curved FSS reflector, a Ka-band planar FSS-backed reflectarray antenna was suggested as the third possible antenna configuration. To facilitate the investigation of this antenna, a concentric dual split-loop element, which provides phase adjustment for circularly polarized fields at 20 and 30 GHz simultaneously, was examined as element type for the FSS-backed reflectarray. The element is optimized to suppress cross polarization and provides a full  $360^\circ$  phase variation at both frequency bands by utilizing the variable rotation technique (VRT). An iterative design procedure was developed which improves the reflectarray antenna design, by which two prototype reflectarray antennas were designed and manufactured: one with a conventional solid ground-plane and a second with an FSS ground-plane. Both antennas were measured at the DTU-ESA Spherical Near-Field Antenna Test Facility and the results validate the performance of the concentric dual split-loop element and the reflectarray designs. Both prototypes reflectarrays are offset-fed and have dimensions of  $40 \times 40 \text{ cm}^2$  ( $80 \times 80$  elements). The first prototype demonstrates aperture illumination efficiencies in the order of 53 to 63 % over both frequency bands of interest. For the second prototype, the aperture illumination efficiency varies from 32 to 48 %, which owes to a suboptimal design of the FSS and the reflectarray elements where the magnitude of the co-polar reflection coefficients varies between -1.5 and -0.5 dB for different element geometries. Therefore, not all the energy is reflected by the reflectarray. By further optimization of the element design, the maximum gain and thus aperture illumination efficiency of the reflectarray may be improved. Finally, the L-band transparency was demonstrated by measurements of a commercial L-band antenna that was located behind and radiated through the FSS-backed reflectarray. These measurements shown negligible influence on the input impedance as well as the radiation pattern of the L-band antenna, where the maximum directivity decreases by less than 0.2 dB.

The antennas described above demonstrate promising performance and are all recommended for a hybrid L/Ka-band antenna. However, the following topics are proposed for future investigations before the final choice of antenna is made.

For the combined L/Ka-band single/dual reflector, the placement of the feed cable for the backfire helical antenna must be determined. This may be done by using a cable drawn in metallic struts that support the sub-reflector. However, this will cause undesirable scattering from the struts. In [P1], a cable drawn through a coaxial-type Ka-band waveguide, which also serves as support for the sub-reflector, is proposed and should be investigated further.

The Ka-band parabolic FSS reflector antenna shows satisfying performance, but may be improved by a more optimized mapping of the FSS elements onto the double-curved surface. However, a major challenge is the fabrication of such a double-curved FSS reflector. For a commercial antenna, the manufacturing costs should be low, while mechanical requirements with respect to accuracy as well as robustness are tough. Feasible fabrication techniques must thus be assessed.

The results of this study demonstrated the low influence of Ka-band FSS antennas on L-band antennas radiating through these. However, for both the FSS reflector and the FSS-backed reflectarray, the antennas are recommended to be used in a dual reflector/reflectarray configuration, due to the spherical radome which usually encloses maritime satellite communication antennas. Thus, investigations on the influence of the Ka-band waveguide, horn and sub-reflector, on the L-band antenna radiation must be carried out. The use of a reconfigurable reflectarray sub-reflector is also suggested to be studied, since this presents desirable features for tracking antennas [101, 102].

In this study, the L-band transparency of the Ka-band FSSs was assessed by infinite planar simulations and experimental validations. It is proposed to formulate a low-frequency model of the FSS reflector and FSS-backed reflectarray, e.g. by an impedance boundary condition formulation [103]. Doing this enables the Ka-band antenna to be included in the L-band antenna design, thus accounting and potentially suppressing the influence of the Ka-band antenna.



## REFLECTARRAY MODELING

---

This appendix presents details on the analysis methods used for the reflectarray antennas that were considered in this project. The numerical code that was implemented is validated by reflectarray antennas that were measured at the DTU-ESA Spherical Near-Field Antenna Test Facility.

### A.1 Element Analysis

For the analysis of reflectarray antennas, different methods exist to analyze the scattering of the individual reflectarray elements [30]. In this project, local periodicity (LP) is utilized such that each element is analyzed assuming it is located in an infinite array of identical elements as illustrated in Figure A.1. Using this approach, the computational problem is reduced to a single reflectarray element, which is analyzed using the commercial software Ansys Designer [76].

The element is characterized by its position  $(x_{pq}, y_{pq})$ , where  $p$  and  $q$  are the indices of the element in the  $x$  and  $y$  direction, respectively, and the unit cell dimensions  $d_x$  and  $d_y$ , see Figure A.1.

A finite number of element geometry samples is analyzed for a multiple of plane waves that cover the incidence angles for a particular reflectarray design. The outcome of this analysis is a scattering matrix look-up table, which is stored and can be reused for multiple reflectarray designs.

### A.2 Far-Field Calculation

In the pursuit of accurate analysis of reflectarray antennas, the calculation of the radiation pattern has been found to be an important step, and yet often neglected. In this project, the equivalent currents technique [95, technique II] is utilized. The equivalent electric currents,  $\mathbf{J}$ , and magnetic currents,  $\mathbf{M}$ , are found by the aperture fields that may be expressed in terms of summations of



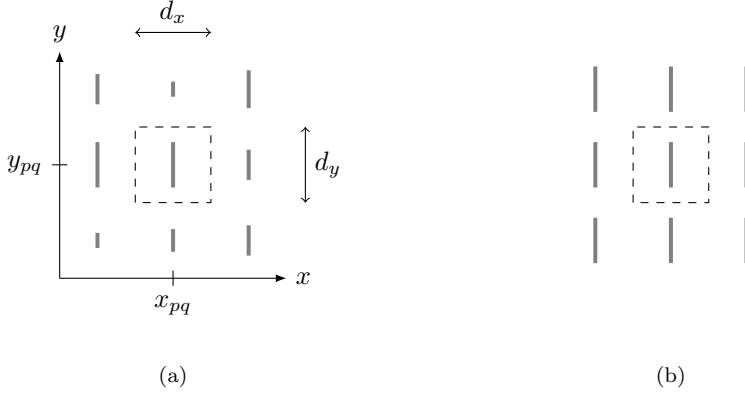


**Figure A.1** (a) The reflectarray element under consideration at the center, and (b) the application of the LP assumption where the element is considered as if it was located in an infinite array of identical elements.

Floquet harmonics with index  $(m, n)$ . The far-field is found by a summation of the aperture fields of all reflectarray elements with index  $(p, q)$ .

The radiated far-field can be isolated to the field that is radiated by the equivalent electric currents

$$\begin{aligned} \mathbf{E}_A(\mathbf{r}) = & -jk_0\eta_0 \frac{e^{-jk_0r}}{4\pi r} \sum_{pq} e^{j(k_x x_{pq} + k_y y_{pq})} \sum_{mn} \zeta_{mn} \\ & \left[ \hat{\theta} \left( \cos \theta \cos \phi J_{pq,x}^{mn} + \cos \theta \sin \phi J_{pq,y}^{mn} \right) \right. \\ & \left. + \hat{\phi} \left( \cos \phi J_{pq,y}^{mn} - \sin \phi J_{pq,x}^{mn} \right) \right], \end{aligned} \quad (\text{A.1})$$

and the equivalent magnetic currents

$$\begin{aligned} \mathbf{E}_F(\mathbf{r}) = & jk_0 \frac{e^{-jk_0r}}{4\pi r} \sum_{pq} e^{j(k_x x_{pq} + k_y y_{pq})} \sum_{mn} \zeta_{mn} \\ & \left[ \hat{\phi} \left( \cos \theta \cos \phi M_{pq,x}^{mn} + \cos \theta \sin \phi M_{pq,y}^{mn} \right) \right. \\ & \left. - \hat{\theta} \left( \cos \phi M_{pq,y}^{mn} - \sin \phi M_{pq,x}^{mn} \right) \right], \end{aligned} \quad (\text{A.2})$$

where

$$\zeta_{mn} = d_x d_y e^{j(k_z - \gamma_0^{mn})} \text{sinc} \left( \frac{(k_x - \beta_{xmn}) d_x}{2\pi} \right) \text{sinc} \left( \frac{(k_y - \beta_{ymn}) d_y}{2\pi} \right). \quad (\text{A.3})$$

In here,  $k_x = k_0 \sin \theta \cos \phi$ ,  $k_y = k_0 \sin \theta \sin \phi$  and  $k_z = k_0 \cos \theta$ , where  $k_0$  is the free space wave number, and  $\eta_0$  is the intrinsic impedance of free space.  $\beta_{xmn}$ ,  $\beta_{ymn}$  and  $\gamma_0^{mn}$  are the Floquet wave numbers.  $J_{pq,x}^{mn}$  and  $J_{pq,y}^{mn}$  are the  $x$ - and  $y$ -components of the equivalent electric currents that are induced by the  $p, q$  Floquet mode in the  $m, n$  unit cell. Similarly,  $M_{pq,x}^{mn}$  and  $M_{pq,y}^{mn}$  are the  $x$ - and  $y$ -components of the equivalent electric currents that are induced by the  $p, q$  Floquet mode in the  $m, n$  unit cell. The equivalent currents are defined by

$$\mathbf{J} = \hat{n} \times \mathbf{H}, \quad (\text{A.4})$$

$$\mathbf{M} = -\hat{n} \times \mathbf{E}, \quad (\text{A.5})$$

where  $\mathbf{E}$  and  $\mathbf{H}$  are the total electric and magnetic fields at the surface and  $\hat{n}$  is the outward unit vector normal to the surface. When grating lobes are not present, it is sufficient to include only the  $m = n = 0$  in the above formulation.

The use of the image principle can be used to short-circuit one of the two equivalent currents, However, the use of both equivalent currents is found to be more accurate than by using only one current. Thus both electric and magnetic equivalent currents are used. Furthermore, the far-field in the entire far-field sphere can be determined using this approach.

### A.3 Validation

The analysis tool that was developed in this project, was validated by analyses of two existing Ku-band reflectarray samples at DTU, DTU/Ticra sample I and DTU/Ticra sample II, respectively. Both reflectarrays are printed on a 0.762 mm thick Rogers 4350B substrate, and the permittivity is 3.66 and the loss tangent is 0.0037.

The antenna configuration and support structure are similar to those that were utilized in the developed Ka-band reflectarrays. The DTU/Ticra sample I and antenna support structure are depicted in Figure A.2. The antennas were measured at the DTU-ESA Spherical Near-Field Antenna Test Facility, with a  $1\sigma$  uncertainty of 0.1 dB for the maximum directivity.

#### A.3.1 DTU/Ticra sample I

The first reflectarray sample, DTU/Ticra sample I, is an offset reflectarray antenna which is designed to have a pencil beam in the specular direction. The feed antenna is located 600 mm from the center of the reflectarray in the direction  $\phi = 0^\circ$  and  $\theta = 30^\circ$ , thus the main beam is in the direction  $\phi = 180^\circ$  and  $\theta = 30^\circ$ . The dimensions of the reflectarray are 435 mm  $\times$  435 mm, consisting of 30  $\times$  30 elements, and the PCB mask layout is depicted in Figure A.3.

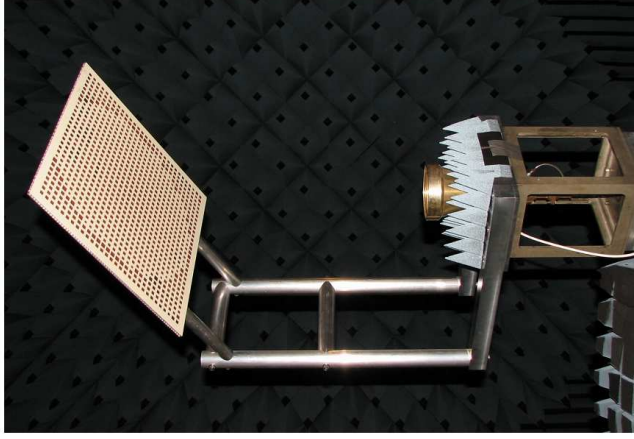


**Figure A.2** *Reflectarray validation measurement setup of the DTU/Ticra sample I.*

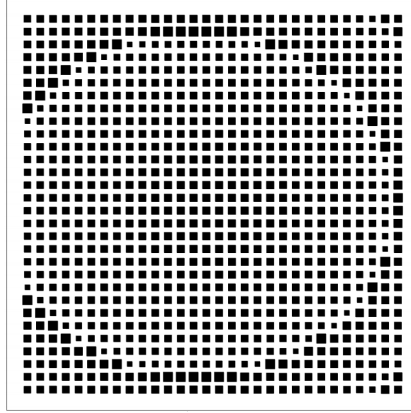


**Figure A.3** *PCB layout mask of the DTU/Ticra sample I.*

The simulated and measured gain patterns of the DTU/Ticra sample I are shown in Figure A.4, at 9.6 GHz in the  $\phi = 180^\circ$  plane. A good agreement is observed in both the front and back hemisphere. The measured maximum gain is 29.7 dBi, and the simulations deviated by less than 0.1 dB. The measured maximum cross polarization is -7.17 dBi and the simulated is 0.14 dB higher.

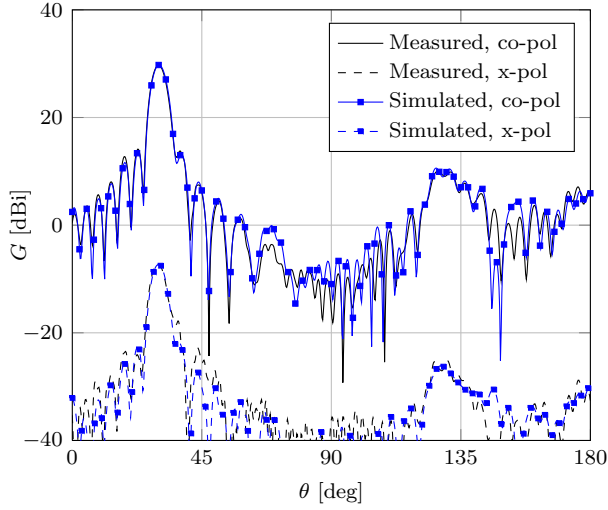


**Figure A.4** Simulated and measured gain pattern of DTU/Ticra sample I at 9.6 GHz in the  $\phi=180^\circ$  cut.

### A.3.2 DTU/Ticra sample II

The dimensions of the second reflectarray sample, DTU/Ticra sample II, are equal to the dimensions of the DTU/Ticra Sample I. The feed antenna is located 350 mm from the center of the reflectarray, in the direction  $\phi = 0^\circ$  and  $\theta = 45^\circ$ . The reflectarray produces a collimated beam in the direction  $\phi = 135^\circ$  and  $\theta = 35^\circ$ , which causes the reflectarray elements to be more aperiodic than the DTU/Ticra sample I, as seen in Figure A.5.

The measured and simulated gain patterns of DTU/Ticra sample II are shown in Figure A.6, at 9.6 GHz in the  $\phi = 135^\circ$  plane. The measured maximum gain is 18.8 dBi, while the simulated maximum gain is 18.3 dBi. The measured maximum cross polarization is 3.4 dBi, and the simulated maximum cross polarization deviates up to 2.2 dB on each side of the maximum gain. The discrepancy in the  $\theta = 145^\circ$  direction is an erroneous beam due to discontinuous equivalent currents [95].

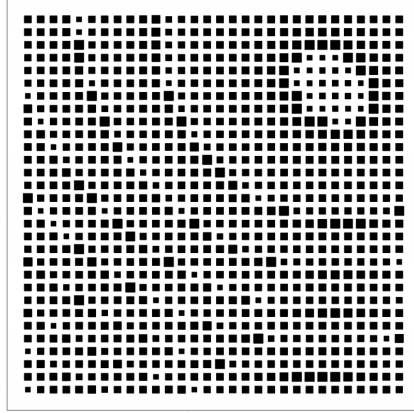


**Figure A.5** *PCB layout mask of the DTU/Ticra sample II.*

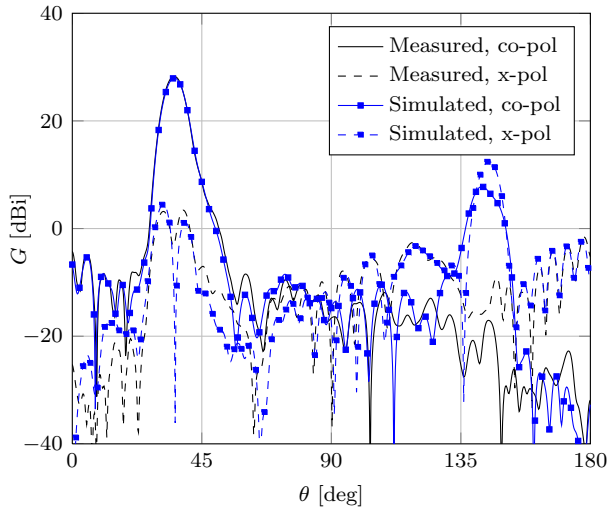


**Figure A.6** *Radiation pattern of DTU/Ticra sample II at 9.6 GHz in the  $\phi=135^\circ$  cut.*

# B

## VARIABLE ROTATION TECHNIQUE

---

The variable rotation technique (VRT) used in reflectarray antenna design is thoroughly described in [97]. However, the description is specifically given for stub-tuned patch elements. This appendix presents the derivation of VRT for arbitrary elements and takes outset in the linear orthogonal reflection coefficients.

### B.1 Derivation

For simplicity, the element under consideration is a dipole as depicted in B.1, but the derivation holds for arbitrary element geometries. An  $x, y$  coordinate system is defined with origin in the center of the reflectarray element. A local  $u, v$ -coordinate system is likewise defined in the center of the element, but is fixed to the element, thus the rotation of the element is described by the rotation angle  $\psi$  which is the rotation angle of the  $u, v$ -coordinate system relative to the  $x, y$ -coordinate system.

Assuming an RHCP plane wave propagating in the negative  $z$  direction is incident on the reflectarray unit cell depicted in Figure B.1

$$\mathbf{E}^i = (\hat{x} + j\hat{y}) E_0 e^{jkz}, \quad (\text{B.1})$$

the wave can be described in the local coordinate system  $(u, v)$ ,

$$\begin{aligned} \mathbf{E}^i &= ([\hat{u} \cos \psi - \hat{v} \sin \psi] + j[\hat{u} \sin \psi + \hat{v} \cos \psi]) E_0 e^{jkz} \\ &= (\hat{u} [\cos \psi + j \sin \psi] + j\hat{v} [\cos \psi + j \sin \psi]) E_0 e^{jkz}, \\ &= (\hat{u} + j\hat{v}) e^{j\psi} E_0 e^{jkz}. \end{aligned} \quad (\text{B.2})$$

For now, it is assumed that the FSS does not produce any cross-polar field, thus the reflected field may be given by the transverse reflection coefficients  $R_u, R_v$

$$\mathbf{E}^s = (\hat{u} R_u + j\hat{v} R_v) E_0 e^{j\psi} e^{-jkz}. \quad (\text{B.3})$$

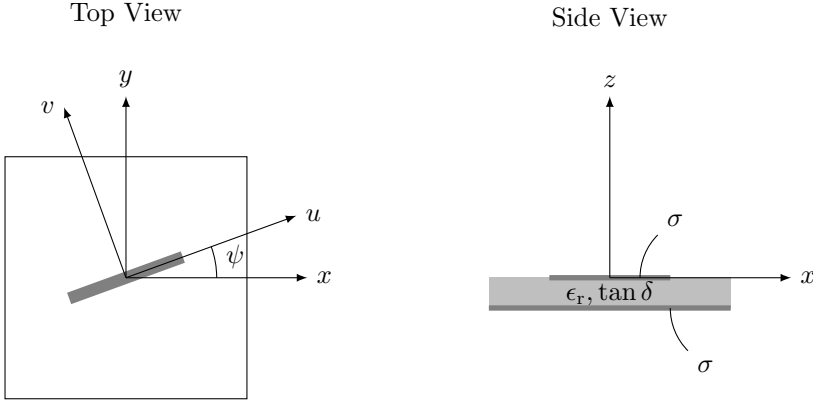


**Figure B.1** Global  $(x, y)$  and local  $(u, v)$  coordinate systems used in the element rotation technique.

The reflection coefficients in the above expression may be rewritten

$$\begin{aligned}
 \hat{u}R_u + j\hat{v}R_v &= [\hat{x} \cos \psi + \hat{y} \sin \psi] R_u + j[-\hat{x} \sin \psi + \hat{y} \cos \psi] R_v \\
 &= \hat{x}R_u \cos \psi + \hat{y}R_u \sin \psi + j\hat{y}R_v \cos \psi - j\hat{x}R_v \sin \psi \\
 &= [\hat{x}R_u + j\hat{y}R_v] \cos \psi - [\hat{x}R_v + j\hat{y}R_u] j \sin \psi \\
 &= \frac{1}{2} ([\hat{x}R_u + j\hat{y}R_v] [e^{j\psi} + e^{-j\psi}] - [\hat{x}R_v + j\hat{y}R_u] [e^{j\psi} - e^{-j\psi}]) \\
 &= \frac{1}{2} ([\hat{x}R_u + j\hat{y}R_v - \hat{x}R_v - j\hat{y}R_u] e^{j\psi} + [\hat{x}R_u + j\hat{y}R_v + \hat{x}R_v + j\hat{y}R_u] e^{-j\psi}) \\
 &= \frac{1}{2} ([R_u - R_v] [\hat{x} - j\hat{y}] e^{j2\psi} + [R_u + R_v] [\hat{x} + j\hat{y}] e^{-j\psi}). \quad (\text{B.4})
 \end{aligned}$$

Using (B.4) in (B.3), the reflected field can be written

$$\mathbf{E}^s = \frac{1}{2} ([R_u - R_v] [\hat{x} - j\hat{y}] e^{j2\psi} + [R_u + R_v] [\hat{x} + j\hat{y}]) E_0 e^{-jkz}, \quad (\text{B.5})$$

which is similar to the reflected field from [97], which is, however, deduced less general for stub-tuned patch elements.

From (B.5), it is observed that when  $R_u = -R_v$ , the reflected field is a pure RHCP wave for the given RHCP incident wave. For  $R_u = -R_v = 1$ , (B.3) becomes

$$\mathbf{E}^s = E_0 (\hat{x} - j\hat{y}) e^{j2\psi} e^{-jkz}. \quad (\text{B.6})$$

The same derivation can be made from a LHCP incident wave, which leads to the conclusion that the reflected wave will have the same sense of rotation as the incident wave. It is also noted, that when the element is rotated by  $\psi$ , the reflected wave is delayed or advanced  $2\psi$ , depending on the sense of rotation of the element and of the incident wave. However, in this conclusion one crucial assumption is made, which is that the reflection coefficients  $R_u$  and  $R_v$  are independent of rotation angle. This is the case for reflectarray elements where the mutual coupling is low, but it does not hold for reflectarray elements in general.

For  $R_u = R_v$ , the sense of rotation will be opposite for the incident and reflected waves, which is the case of e.g. an infinite PEC. By the second term of (B.3), it is seen that the reflected wave is independent of the rotation angle  $\psi$ .

## B.2 Circular Polarized Reflection Coefficients

The scattering matrices of reflectarray elements that are found using Ansys Designer are given in terms of transverse vertical (V) and horizontal (H) components. The unit vectors,  $\hat{a}_V^i$  and  $\hat{a}_H^i$  are shown in Figure B.2, and it is observed that for normal incidence ( $\phi = 0^\circ, \theta = 0^\circ$ ) and zero rotation of the element under investigation ( $\psi = 0$ ), the unit vectors are related by  $\hat{a}_V^i = -\hat{u}$  and  $\hat{a}_H^i = \hat{v}$ .

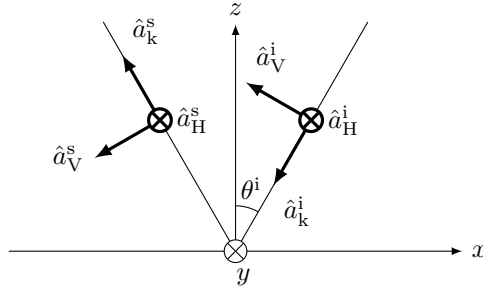


**Figure B.2** Oblique incidence of vertical (V) and horizontal (H) plane waves.

For the incident and scattered plane waves, circular polarization unit vectors



are defined by

$$\hat{a}_{\text{RHCP}}^i = \frac{1}{\sqrt{2}} (\hat{a}_V^i - j\hat{a}_H^i), \quad (\text{B.7a})$$

$$\hat{a}_{\text{LHCP}}^i = \frac{1}{\sqrt{2}} (\hat{a}_V^i + j\hat{a}_H^i), \quad (\text{B.7b})$$

$$\hat{a}_{\text{RHCP}}^s = \frac{1}{\sqrt{2}} (\hat{a}_V^s + j\hat{a}_H^s), \quad (\text{B.7c})$$

$$\hat{a}_{\text{LHCP}}^s = \frac{1}{\sqrt{2}} (\hat{a}_V^s - j\hat{a}_H^s), \quad (\text{B.7d})$$

where  $\hat{a}_V^s$  and  $\hat{a}_H^s$  are the vertical and horizontal unit vectors in the plane of incidence, as shown in Figure B.2. Consider an incident field  $\mathbf{E}^i = \hat{a}_V^i E_V^i + \hat{a}_H^i E_H^i$ . This field can be decomposed into circular components

$$E_{\text{RHCP}}^i = (\hat{a}_{\text{RHCP}}^i)^* \cdot \mathbf{E}^i = \frac{1}{\sqrt{2}} (E_V^i + jE_H^i), \quad (\text{B.8a})$$

$$E_{\text{LHCP}}^i = (\hat{a}_{\text{LHCP}}^i)^* \cdot \mathbf{E}^i = \frac{1}{\sqrt{2}} (E_V^i - jE_H^i), \quad (\text{B.8b})$$

where  $*$  denotes the complex conjugate, and similar for the scattered field,  $\mathbf{E}^s = \hat{a}_V^s E_V^s + \hat{a}_H^s E_H^s$ , the right and left hand circular field components are found by

$$E_{\text{RHCP}}^s = (\hat{a}_{\text{RHCP}}^s)^* \cdot \mathbf{E}^s = \frac{1}{\sqrt{2}} (E_V^s - jE_H^s), \quad (\text{B.8c})$$

$$E_{\text{LHCP}}^s = (\hat{a}_{\text{LHCP}}^s)^* \cdot \mathbf{E}^s = \frac{1}{\sqrt{2}} (E_V^s + jE_H^s). \quad (\text{B.8d})$$

The above equations can be expressed in matrix form, which for the incident field is

$$\begin{bmatrix} E_{\text{RHCP}}^i \\ E_{\text{LHCP}}^i \end{bmatrix} = \frac{1}{\sqrt{2}} \begin{bmatrix} 1 & j \\ 1 & -j \end{bmatrix} \begin{bmatrix} E_V^i \\ E_H^i \end{bmatrix}. \quad (\text{B.9})$$

Taking the matrix inverse, the linear incident field components can be expressed in terms of the circular incident field components by

$$\begin{bmatrix} E_V^i \\ E_H^i \end{bmatrix} = \frac{1}{\sqrt{2}} \begin{bmatrix} 1 & 1 \\ -j & j \end{bmatrix} \begin{bmatrix} E_{\text{RHCP}}^i \\ E_{\text{LHCP}}^i \end{bmatrix}. \quad (\text{B.10})$$

The matrix equation for the scattered field is

$$\begin{bmatrix} E_{\text{RHCP}}^s \\ E_{\text{LHCP}}^s \end{bmatrix} = \frac{1}{\sqrt{2}} \begin{bmatrix} 1 & -j \\ 1 & j \end{bmatrix} \begin{bmatrix} E_V^s \\ E_H^s \end{bmatrix}. \quad (\text{B.11})$$

The linear incident and scattered fields are related by the transverse linear reflection coefficient matrix  $\bar{\bar{R}}_l$

$$\begin{bmatrix} E_V^s \\ E_V^s \end{bmatrix} = \bar{\bar{R}}_l \begin{bmatrix} E_H^i \\ E_H^i \end{bmatrix}, \quad (\text{B.12a})$$

where

$$\bar{\bar{R}}_l = \begin{bmatrix} R_{VV} & R_{VH} \\ R_{HV} & R_{HH} \end{bmatrix}. \quad (\text{B.12b})$$

Combining the equations above, the incident and scattered circular field components can be related by

$$\begin{bmatrix} E_{\text{RHCP}}^s \\ E_{\text{LHCP}}^s \end{bmatrix} = \frac{1}{2} \begin{bmatrix} 1 & -j \\ 1 & j \end{bmatrix} \begin{bmatrix} R_{VV} & R_{VH} \\ R_{HV} & R_{HH} \end{bmatrix} \begin{bmatrix} 1 & 1 \\ -j & j \end{bmatrix} \begin{bmatrix} E_{\text{RHCP}}^i \\ E_{\text{LHCP}}^i \end{bmatrix}, \quad (\text{B.13})$$

which can be combined to a circular reflection matrix  $\bar{\bar{R}}_c$  that relates the incident and reflected circular field components by

$$\begin{bmatrix} E_{\text{RHCP}}^s \\ E_{\text{LHCP}}^s \end{bmatrix} = \bar{\bar{R}}_c \begin{bmatrix} E_{\text{RHCP}}^i \\ E_{\text{LHCP}}^i \end{bmatrix}, \quad (\text{B.14a})$$

where

$$\begin{aligned} \bar{\bar{R}}_c &= \begin{bmatrix} R_{rr} & R_{rl} \\ R_{lr} & R_{ll} \end{bmatrix} \\ &= \frac{1}{2} \begin{bmatrix} (R_{VV} - R_{HH}) - j(R_{VH} + R_{HV}) & (R_{VV} + R_{HH}) + j(R_{VH} - R_{HV}) \\ (R_{VV} + R_{HH}) - j(R_{VH} - R_{HV}) & (R_{VV} - R_{HH}) + j(R_{VH} + R_{HV}) \end{bmatrix}. \end{aligned} \quad (\text{B.14c})$$

### B.3 Dipole Example

To exemplify the properties of the element rotation technique, the simple case of a dipole reflectarray element is calculated. The dipole element is simulated in Ansys Designer, with length and width of 3.5 mm and 0.2 mm, respectively. The dielectric is Rogers 5880 Duroid with  $\epsilon_r = 2.2$  and  $\tan \delta = 0.0009$ , of 0.508 mm thickness, and the dipole and ground-plane are of copper ( $\sigma = 58 \text{ MS/m}$ ). The unit cell dimension is 5 mm in both orthogonal directions, and only normal incidence is considered.

The characteristic observations of (B.5) are seen in Figure B.3, where the phases of the linear reflection coefficients  $R_u$  and  $R_v$  are plotted in Figure B.3a, and the amplitude of the circular reflection coefficients  $R_{rr}$  and  $R_{lr}$  are plotted in

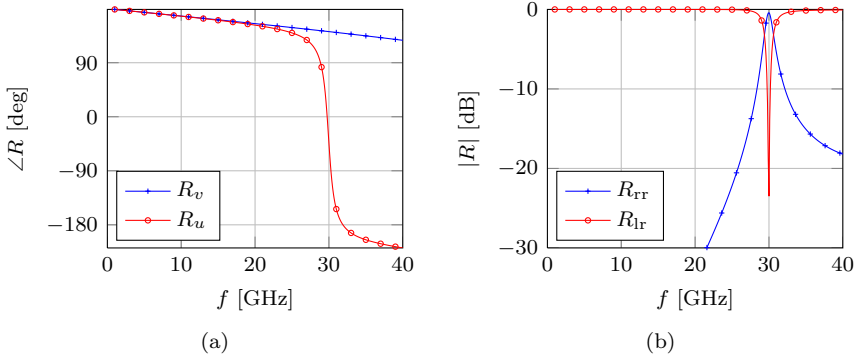


**Figure B.3** The reflection of the dipole reflectarray element in Figure B.1, for  $\psi = 0^\circ$ . (a) shows the phase of the linear transverse reflection coefficients, and (b) shows the amplitude of the circular reflection coefficients.

Figure B.3b. It is observed that at 30.0 GHz, the phase difference of the V and H reflection coefficients is  $180^\circ$ , which by (B.5) translates into a pure RHCP-RHCP reflection. This agrees with the peak RHCP-RHCP reflection coefficient amplitude in Figure B.3b.

Both amplitude and phase of the RHCP-RHCP and RHCP-LHCP reflection coefficients are shown in Figure B.4. It was stated above that when the element is rotated by  $\psi$ , the phase of the element is changed  $2\psi$ . This is shown in Figure B.4b, where it is found that by rotating the dipole  $90^\circ$ , the phase changes from  $140.4^\circ$  to  $-39.6^\circ$ , which yields a phase range of precisely  $180^\circ$ . However, it is noticed that the phase does not follow the  $2\psi$  line accurately. Also, the amplitude varies slightly, most evident in the RHCP-LHCP reflection coefficient. This owes to the fact that the “local” reflection coefficients  $R_u$  and  $R_v$ , which rotates with the element, are not constant when the element is rotated. When the element is rotated in the unit cell, the coupling to neighboring elements is changed, and thus the current distribution and ultimately the reflection coefficients are affected. Due to the low dielectric thickness, the electric field is concentrated between the dipole and ground-plane, and thus only little fringing will couple to the nearest elements.

Due to the finite conductivity of copper and the dielectric loss, the peak RHCP-RHCP reflection coefficient amplitude is less than one, that is  $-0.40$  dB. The loss is specified in Table B.1, where the dielectric loss has been analyzed using PEC, and the conductor loss has been analyzed using lossless Duroid dielectric ( $\tan \delta = 0$ ). It is observed that the loss due to the finite conductivity

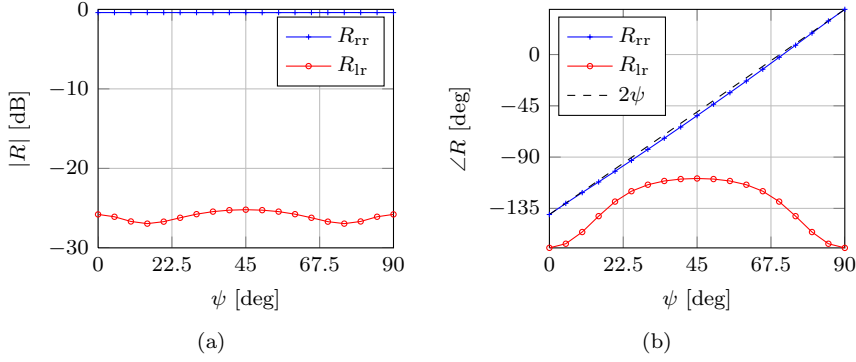


**Figure B.4** The reflection of the dipole reflectarray element in Figure B.1 at 30 GHz, for  $\psi \in [0^\circ, 90^\circ]$ . (a) is the amplitude and (b) is the phase of the circular reflection coefficients.

of copper is the largest. However, both the conductor and dielectric losses depend on the specific unit element geometry. The conductor and dielectric losses for a dipole of twice the width, that is 0.4 mm, have been calculated to 0.16 dB and 0.12 dB, respectively.

**Table B.1** Dielectric and conductor losses in dipole reflectarray element at 30 GHz, using Rogers 5880 substrate ( $\epsilon_r = 2.2$  and  $\tan \delta = 0.0009$ ) and copper ( $\sigma = 58 \text{ MS/m}$ ).

Dielectric loss	0.15 dB
Conductor loss	0.26 dB
Combined loss	0.40 dB



# Publications



## JOURNAL PAPER I

---

# DESIGN, MANUFACTURING, AND TESTING OF A 20/30 GHz DUAL-BAND CIRCULARLY POLARIZED REFLECTARRAY ANTENNA

Thomas Smith, Ulrich Gothelf,  
Oleksiy S. Kim, and Olav Breinbjerg

*Status*

Submitted: May 2013

### **Bibliography**

- [J1] T. Smith, U. Gothelf, O. S. Kim, and O. Breinbjerg, “Design, Manufacturing, and Testing of a 20/30 GHz Dual-Band Circularly Polarized Reflectarray Antenna,” *Submitted to IEEE Antennas Wireless Propag. Lett.*, 2013.





# Design, Manufacturing, and Testing of a 20/30 GHz Dual-Band Circularly Polarized Reflectarray Antenna

Thomas Smith, Ulrich Gothelf, *Member, IEEE*,  
Oleksiy S. Kim, and Olav Breinbjerg, *Member, IEEE*

**Abstract**—This paper documents the design, manufacturing and testing of a single layer dual-band circularly polarized reflectarray antenna for 19.7–20.2 GHz and 29.5–30.0 GHz. The reflectarray is designed using the concentric dual split-loop element and the variable rotation technique which enables full  $360^\circ$  phase adjustment simultaneously in two separate frequency bands. The elements have been optimized to suppress cross-polar reflection. Thereafter, the element data is included in a design-tool that computes the reflectarray layout and the associated radiation patterns. The reflectarray is composed of  $80 \times 80$  elements printed on a  $40 \times 40$  cm<sup>2</sup> Rogers 5880 substrate. The antenna has been manufactured and measured at the DTU-ESA Spherical Near-Field Antenna Test Facility. The peak gain is 35.8 dBi and 40.0 dBi at 20.0 and 29.8 GHz, respectively, and the aperture illumination efficiency is in the range of 53 to 63 % over the two frequency bands.

**Index Terms**—reflectarray, dual-band, circularly polarized, concentric dual split-loop.

## I. INTRODUCTION

**P**RINTED reflectarray antennas combine desirable features of two conventional aperture antennas, namely the reflector antennas and the planar phased array antennas [1]. It generally consists of an array of scattering elements that are illuminated by a feeding antenna. The beam forming is obtained by adjusting the reflection phase of each individual array element. Depending on the chosen element topology, different phasing techniques have been developed such as stub tuned elements [2], element size variation [3], variable rotation technique (VRT) [4] or random element shapes optimized by use of genetic algorithm [5].

In this communication, a reflectarray antenna for left-hand circular polarization (LHCP) at 19.7–20.2 GHz and right-hand circular polarization (RHCP) at 29.5–30.0 GHz is presented. The reflectarray utilizes the concentric dual split-loop element, that facilitates simultaneous phase adjustment at 20 and 30 GHz. A dual-band circularly polarized corrugated horn

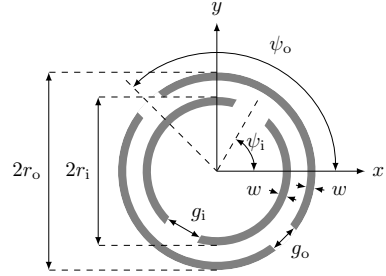


Fig. 1. Geometry of the concentric dual split-loop element.

antenna with integrated polarizer is used as a feeding antenna. The concept is validated by a prototype antenna which is manufactured and measured at the DTU-ESA Spherical Near-Field Antenna Test Facility [6].

The reflectarray is modeled using the local periodicity (LP) assumptions, such that each reflectarray element is assumed to be located in an infinite array of identical elements. The analysis is thus split into two parts: the first considering only the reflectarray elements, and the second considering the reflectarray design and far-field calculation. For the first part, the 2.5D method of moments solver Ansys Designer [7] is used with periodic boundaries and plane-wave excitation. The second part is carried out using an in-house developed numerical code.

The time factor  $e^{j\omega t}$  is assumed and suppressed throughout this communication.

## II. ELEMENT DESIGN

For electrically large planar reflectarrays, the frequency bandwidth is limited due to the differential spatial phase delay [8], thus it is essential to adjust the phase separately in the two frequency bands of interest. For this purpose, the concentric dual split-loop element, depicted in Fig. 1, has been investigated in [9]. The outer and inner split-loops are characterized by their radii  $r_o$  and  $r_i$ , respectively, measured from the center to the outside of the conductor, the rotation angles  $\psi_o$  and  $\psi_i$ , the gap sizes  $g_o$  and  $g_i$ , and equal conductor width  $w$ . The element dimensions are given in Table I.

The element employs the VRT to obtain a desired phase at 20 and 30 GHz simultaneously, by adjusting  $\psi_o$  and  $\psi_i$ ,

Manuscript submitted May, 2013.

T. Smith is with Cobham Satcom, Kgs. Lyngby 2800, Denmark, and also with the Department of Electrical Engineering, Electromagnetic Systems, Technical University of Denmark, Kgs. Lyngby 2800, Denmark (e-mail: thomas.smith@cobham.com).

U. Gothelf is with Cobham Satcom, Kgs. Lyngby 2800, Denmark (e-mail: ulrich.gothelf@cobham.com).

O. S. Kim and O. Breinbjerg are with the Department of Electrical Engineering, Electromagnetic Systems, Technical University of Denmark, Kgs. Lyngby 2800, Denmark (e-mail: osk@elektro.dtu.dk; ob@elektro.dtu.dk).

Color versions of one or more of the figures in this letter are available online at <http://ieeexplore.ieee.org>.

TABLE I  
REFLECTARRAY ELEMENT GEOMETRY DATA.

$r_o$	2.05 mm
$r_i$	1.40 mm
$w$	0.2 mm
Square array grid	5 mm $\times$ 5 mm

respectively. The VRT requires that the reflection coefficients of two orthogonal linear components are of equal magnitude and  $180^\circ$  out of phase, in which case a pure LHCP to LHCP,  $R_{ll}$ , (or RHCP to RHCP,  $R_{rr}$ ) reflection is obtained. This is achieved by optimizing the gap sizes  $g_o$  and  $g_i$  to minimize the magnitude of the cross-polar reflection coefficient, i.e. LHCP to RHCP (or RHCP to LHCP). The optimization is conducted for the incidence angles  $\phi = 0^\circ$  and  $\theta = 30^\circ$ , which are the incidence angles at the center of the reflectarray that is designed.

The concentric dual split-loop element has been optimized for a finite number of combinations of  $\psi_o$  and  $\psi_i$  in steps of  $10^\circ$ . The average magnitudes of the cross-polar reflection coefficients for all rotation angles are  $-33$  and  $-31$  dB, at 19.95 GHz and 29.75 GHz, respectively. The 2-dimensional phase curves of the concentric dual split-loop element are shown in Fig. 2, where  $\angle R_{ll}$  is shown at 19.95 GHz and  $\angle R_{rr}$  is shown at 29.75 GHz.

At 19.95 GHz, the reflection coefficient of the concentric dual split-loop element is determined primarily by  $\psi_o$ , which is seen by the almost vertical contour curves in Fig. 2a. For a fixed value of  $\psi_i$ , an almost linear  $360^\circ$  phase variation of  $R_{ll}$  is obtain when rotating  $\psi_o$  from  $0$  to  $180^\circ$ .

At 29.75 GHz, a more complex behavior of  $\angle R_{rr}$  is observed, which depends on both  $\psi_o$  and  $\psi_i$ . However, two important features are noted: For a fixed value of  $\psi_o$ , a full  $360^\circ$  phase variation is achieved when rotating  $\psi_i$  from  $0$  to  $180^\circ$ , and this variation is monotonic in  $\psi_i$ . Therefore, for a fixed value of  $\psi_o$  and desired reflection phase, a unique solution of  $\psi_i$  exists.

The optimized geometries and the associated reflection coefficients are analyzed for a finite set of incidence angles that are required, and are stored in a look-up table that is used in the separate code for the reflectarray design and analysis.

It should be noted that the elements are optimized for the plane wave angles of incidence at the center of the reflectarray, for cross-polar suppression in the specular direction. However, a better reflectarray design may be obtained by optimizing the elements considering more angles of incidence, and for cross-polar suppression in the direction of the main beam that is not specular for all elements.

### III. REFLECTARRAY DESIGN

A numerical code has been implemented to design and analyse reflectarray antennas, which calculates the radiated far-field by the equivalent currents technique [10, technique II]. An offset fed reflectarray antenna has been designed using this code, and manufactured at the Technical University of Denmark (DTU). The feed antenna is located 30 cm from the

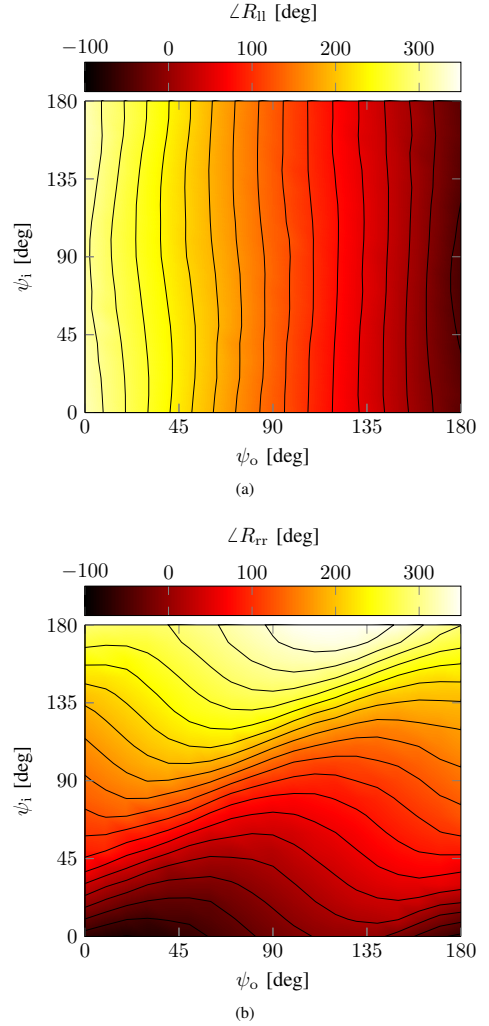


Fig. 2. 2-dimensional phasecurves of the concentric dual split-loop element, for LHCP and RHCP plane wave incidence at 19.95 and 29.75 GHz, respectively.

reflectarray center in the direction  $\phi = 0^\circ$  and  $\theta = 30^\circ$ , and the main beam is pointed in the direction  $\phi = 0^\circ$  and  $\theta = -30^\circ$ . The reflectarray antenna and the utilized coordinate system are depicted in Fig. 3. The reflectarray is printed on a 0.787 mm thick  $40 \times 40$  cm<sup>2</sup> Rogers Duroid 5880 substrate with  $\epsilon_r = 2.2$  and  $\tan \delta = 0.0009$ . The electrical and geometrical data are summarized in Table II.

The reflectarray is designed such that the reflected field of each element adds to a collimated beam in the direction  $\phi = 0^\circ$  and  $\theta = -30^\circ$ . The phase characteristics of the concentric dual split-loop element enable a sequential design procedure [9], where first  $\psi_o$  of all elements are determined

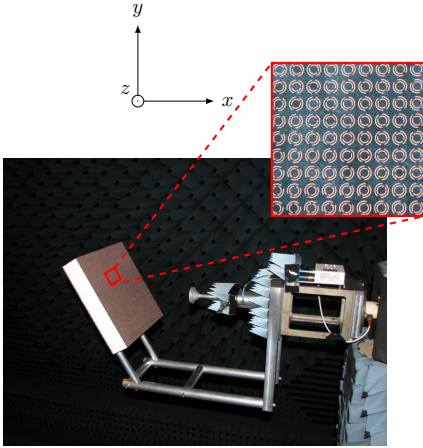


Fig. 3. Offset reflectarray antenna in the DTU-ESA Spherical Near-Field Antenna Test Facility. The coordinate system is oriented with the z-axis orthogonal to the reflectarray surface, and the x-axis in the plane that contains the main beam and the feed antenna.

to obtain a collimated beam at 19.95 GHz, and thereafter  $\psi_i$  of all elements are determined to phase the field accordingly at 29.75 GHz.

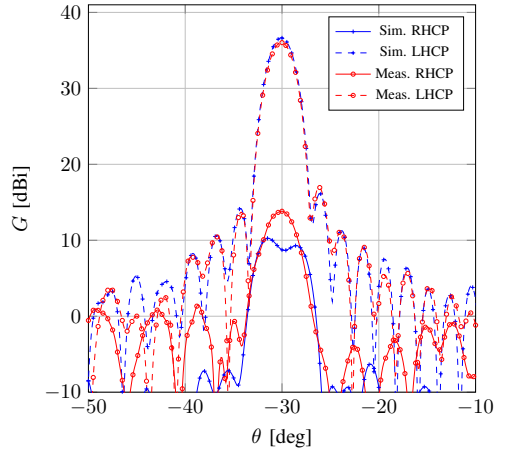
The feed antenna has been analyzed using the commercial software CHAMP [11]. Using this, the incident near-field over the reflectarray aperture has been calculated, which is used in the reflectarray design tool. This makes it possible to use feeding antennas that do not have a well-defined phase center in different radiation planes or at different frequencies, and still obtaining a collimated beam in the desired direction. The directivity of the utilized horn antenna is 15.7 and 13.2 dBi, at 19.95 and 29.75 GHz, respectively, which provides an edge illumination in the range of  $-20$  to  $-5$  dB, relative to the maximum in the reflectarray aperture.

#### IV. REFLECTARRAY RADIATION

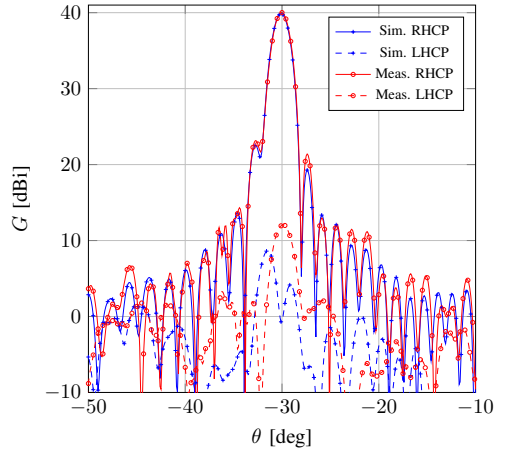
The radiation pattern of reflectarray antenna has been measured at the DTU-ESA Spherical Near-Field Antenna Test Facility. The far-field is obtained through a near-field to far-field transformation, and the  $1\sigma$  uncertainty is 0.1 dB for the peak directivity. The simulated and measured gain patterns of the prototype antenna at 20.0 GHz and 29.8 GHz are shown in Fig. 4, in the  $\phi = 0^\circ$  plane.

TABLE II  
OFFSET REFLECTARRAY ANTENNA DATA.

RX frequencies	19.7 GHz – 20.2 GHz LHCP
TX frequencies	29.5 GHz – 30.0 GHz RHCP
Substrate dimensions	$40 \times 40 \text{ cm}^2$
Substrate thickness	0.787 mm
Substrate properties	$\epsilon_r = 2.2$ , $\tan \delta = 0.0009$
Feed distance to center of array	30 cm
Feed offset angle	$\phi = 0^\circ$ , $\theta = 30^\circ$
Direction of main beam	$\phi = 0^\circ$ , $\theta = -30^\circ$



(a)



(b)

Fig. 4. Measured gain pattern of the reflectarray antenna at (a) 20.0 GHz and (b) 29.8 GHz in the  $\phi = 0^\circ$  plane.

At 20.0 GHz, the measured peak gain is 35.8 dBi and the maximum cross-polarization level is 21.8 dB below that. The side lobe level is 19.1 dB below the peak gain. The simulated peak gain is 0.8 dB higher and the cross polarization level is about 3 dB lower than the measurements. The measured and simulated first three side lobes on each side of the main lobe agree within 0.7 dB dB.

At 29.8 GHz, the measured peak gain is 40.0 dBi. The cross-polarization level and side lobe level are 27 dB and 17 dB below this. The simulated peak gain is 0.2 dB lower than the measured, while the right hand side lobel level is 2 dB lower than the measured. The maximum cross polarization deviates by 3.4 dB. Generally, the measured data agree well with the simulated patterns, considering that the antenna support

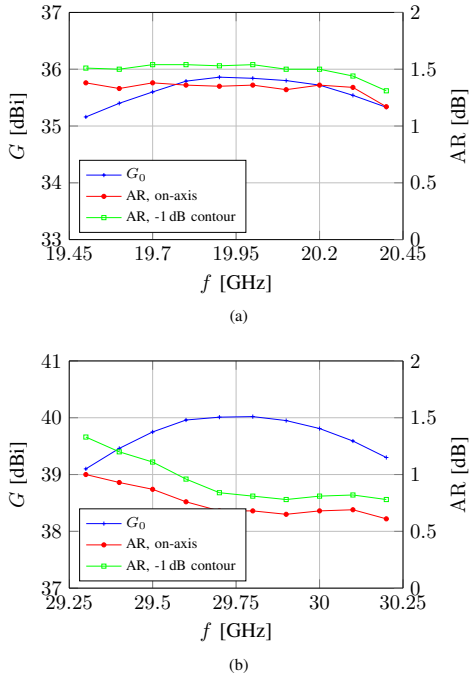


Fig. 5. Co-polar gain and AR measured on axis and along the -1 dB gain contour of the reflectarray at (a) 19.7–20.2 GHz and (b) 29.5–30.0 GHz.

structure is not included in the simulated results.

The asymmetric side lobes observed in Fig. 4b are caused by higher-order modes being excited in the feed antenna polarizer, which causes the incident field to be asymmetric.

The spherical near-field measurements were conducted in steps of 100 MHz over the frequency bands specified in Table II, and the peak gain and maximum axial-ratio (AR) on axis and along the -1 dB gain contour are depicted in Fig. 5. It is seen that the minimum peak gain from 19.7 to 20.2 GHz is 35.6 dBi, and the aperture illumination efficiency is in the range from 53 to 56 %. The measured antenna loss is 0.5 dB.

From 29.5 to 30.0 GHz, the minimum peak gain is 39.8 dBi and the aperture illumination efficiency is from 59 to 63 %. Here, the measured antenna loss is 0.3 dB. The higher aperture illumination efficiency in the upper frequency band is due to a broader feed pattern [12].

## V. CONCLUSION

In this paper, a reflectarray antenna for dual-band circular polarization has been presented. The reflectarray is designed using the concentric split-loop element, which enables simultaneous  $360^\circ$  phase adjustment at two separate frequency bands. The reflectarray was manufactured and measured at the DTU-ESA Spherical Near-Field Antenna Test Facility. The antenna operates at 19.7 – 20.2 GHz and 29.5 – 30.0 GHz with a minimum peak gain of 35.8 and 39.8 dBi in the two

frequency bands of interest, respectively. Aperture illumination efficiencies in the range of 53 to 63 % are obtained.

## REFERENCES

- [1] J. Huang and J. A. Encinar, *Reflectarray Antennas*. IEEE Press, 2008.
- [2] J. Huang, "Microstrip reflectarray," in *Proc. IEEE AP-S Int. Symp.*, 1991, pp. 612–615.
- [3] D. Pozar and T. Metzler, "Analysis of a reflectarray antenna using microstrip patches of variable size," *Electronics Letters*, vol. 29, no. 8, pp. 657–658, 1993.
- [4] J. Huang and R. Pogorzelski, "A Ka-band microstrip reflectarray with elements having variable rotation angles," *IEEE Trans. Antennas Propag.*, vol. 46, no. 5, pp. 650–656, 1998.
- [5] Y. Aoki, H. Deguchi, and M. Tsuji, "Reflectarray with arbitrarily-shaped conductive elements optimized by genetic algorithm," in *Proc. IEEE AP-S Int. Symp.*, 2011, pp. 960–963.
- [6] "DTU-ESA spherical near-field antenna test facility," [http://www.dtu.dk/centre/ems/English/research/dtu\\_esa\\_facility.aspx](http://www.dtu.dk/centre/ems/English/research/dtu_esa_facility.aspx).
- [7] "Ansys Designer," <http://www.ansys.com>.
- [8] D. M. Pozar, "Bandwidth of reflectarrays," *Electronics Letters*, vol. 39, no. 21, pp. 1490–1491, 2003.
- [9] T. Smith, N. V. Larsen, U. V. Gothelf, O. S. Kim, and O. Breinbjerg, "20/30 ghz dual-band circularly polarized reflectarray antenna based on the concentric dual split-loop element," in *Proc. ESA Antenna Week*, 2012.
- [10] M. Zhou, S. Sorensen, E. Jorgensen, P. Meincke, O. Kim, and O. Breinbjerg, "An accurate technique for calculation of radiation from printed reflectarrays," *IEEE Antennas and Wireless Propagation Letters*, vol. 10, pp. 1081–1084, 2011.
- [11] "TICRA CHAMP," <http://www.ticra.com/products/software/champ>.
- [12] T. Smith, N. V. Larsen, U. V. Gothelf, O. S. Kim, and O. Breinbjerg, "An offset-fed 20/30 ghz dual-band circularly polarized reflectarray antenna," in *Proc. EuCAP*, 2013.

## JOURNAL PAPER II

---

# AN FSS-BACKED 20/30 GHz CIRCULARLY POLARIZED REFLECTARRAY FOR A SHARED APERTURE L- AND KA-BAND SATELLITE COMMUNICATION ANTENNA

Thomas Smith, Ulrich Gothelf,  
Oleksiy S. Kim, and Olav Breinbjerg

*Status*

Submitted: May 2013

### **Bibliography**

- [J2] T. Smith, U. Gothelf, O. S. Kim, and O. Breinbjerg, “An FSS-backed 20/30 GHz Circularly Polarized Reflectarray for a Shared Aperture L- and Ka-band Satellite Communication Antenna,” *Submitted to IEEE Trans. Antennas Propag.*, 2013.



# An FSS-backed 20/30 GHz Circularly Polarized Reflectarray for a Shared Aperture L- and Ka-band Satellite Communication Antenna

Thomas Smith, Ulrich Gothelf *Member, IEEE*,  
Oleksiy S. Kim, and Olav Breinbjerg, *Member, IEEE*

**Abstract**—A concept demonstrator for a shared aperture antenna for simultaneous operation at L- (1,525 to 1,661 MHz) and Ka-band (19.2 to 20.2 GHz and 29.5 to 30.0 GHz) is presented. The antenna is a stacked antenna, comprising a Ka-band reflectarray antenna with a frequency selective surface (FSS) ground-plane above an L-band patch array antenna. The reflectarray is based on the concentric dual split-loop element backed by a concentric dual-loop FSS element. The reflectarray comprises  $80 \times 80$  elements and is printed on a  $40 \times 40$  cm<sup>2</sup> Rogers 5880 substrate, while the L-band antenna is a  $2 \times 2$  patch array antenna. The antennas have been manufactured at the Technical University of Denmark (DTU) and measured at the DTU-ESA Spherical Near-Field Antenna Test Facility. The reflectarray provides a maximum directivity of 36.4 and 38.5 dBi at 20.0 and 29.8 GHz, respectively, and an aperture illumination efficiency up to 57 % and 48 %, in the two frequency bands of interest. The degradation in the L-band patch array performance due to the reflectarray is negligible, and the antenna provides a minimum directivity of 11.8 dBi over the L-band frequency band.

**Index Terms**—FSS-backed reflectarray, concentric dual split-loop element, shared aperture antenna.

## I. INTRODUCTION

Ka-band satellite communication provides high-speed internet access and multimedia services, but is sensitive to heavy rain that may cause complete drop-outs in the communication link [1]. L-band satellite communication has been used through decades and presents a stable solution, which is, however, limited by its lower data bandwidth [2]. In this paper, a hybrid antenna for simultaneous L- and Ka-band satellite communication is proposed to exploit the high-speed data rate at Ka-band while preserving the stable L-band data link as fallback without outage.

Though regarded as a narrow-band antenna, the printed reflectarray presents a viable solution for multiband antennas [3], [4]. Multi-band reflectarray antennas may be designed

using broadband elements [5], [6], multi-layer elements [7], [8], interleaved array grids [9], [10] or stacked arrays [11]. The choice is determined by the frequency band separation and possible constraints on the mechanical design.

The use of mature printed circuit board (PCB) fabrication techniques enables easy and inexpensive manufacturing of the antenna, which also facilitates the use of a frequency selective surface (FSS) ground-plane on the bottom layer. In this way, an antenna operating at a separate frequency may be located behind and radiate through the FSS-backed reflectarray [12], [13].

In this work, a stacked L- and Ka-band antenna configuration is proposed, that facilitates utilization of the available antenna aperture at both frequency bands. The Ka-band antenna is a novel FSS-backed dual-band circularly polarized reflectarray antenna. The FSS-backed reflectarrays in [12], [13] are single-band and linearly polarized, thus a new reflectarray element and design procedure have been developed and are presented in this paper, to facilitate operation with opposite sense of circular polarization in two separate frequency bands. The L-band antenna is an existing commercially available four-patch array satellite communication antenna [14] that has not been optimized for the present application. The antenna concept is depicted in Fig. 1. The antenna demonstrator radiates left-hand circular polarization (LHCP) at 19.7 to 20.2 GHz (RX), right-hand circular polarization (RHCP) from 29.5 to 30.0 GHz (TX), and RHCP from 1,525 to 1,661 MHz

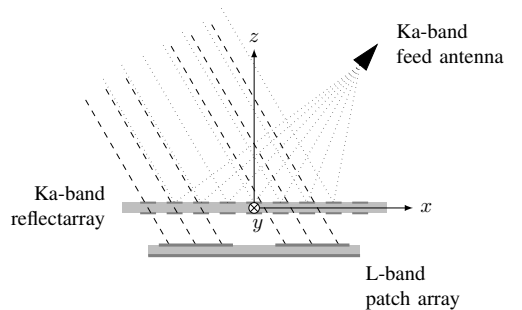


Fig. 1. Geometry of the shared aperture antenna concept. The Ka-band antenna is a printed FSS-backed reflectarray antenna, which is located above an L-band patch array antenna.

Manuscript submitted May, 2013.

T. Smith is with Cobham Satcom, Kgs. Lyngby 2800, Denmark, and also with the Department of Electrical Engineering, Electromagnetic Systems, Technical University of Denmark, Kgs. Lyngby 2800, Denmark (e-mail: thomas.smith@cobham.com).

U. Gothelf is with Cobham Satcom, Kgs. Lyngby 2800, Denmark (e-mail: ulrich.gothelf@cobham.com).

O. S. Kim and O. Breinbjerg are with the Department of Electrical Engineering, Electromagnetic Systems, Technical University of Denmark, Kgs. Lyngby 2800, Denmark (e-mail: osk@elektro.dtu.dk; ob@elektro.dtu.dk).

Color versions of one or more of the figures in this letter are available online at <http://ieeexplore.ieee.org>.



(RX+TX).

The paper is organized as follows: First, the Ka-band reflectarray element is described and the phase characteristics of the element are given. Subsequently, an iterative design procedure is presented that exploits the element characteristics in the design of dual-band pencil beam reflectarrays. A prototype FSS-backed reflectarray is designed using this procedure, and the radiation patterns of the prototype antenna is measured, and the reflectarray performance is discussed. Thereafter, the measured radiation patterns of the L-band antenna – radiating through the reflectarray – are presented. Lastly, conclusions on the proposed antenna concept are given.

The time notation  $e^{j\omega t}$  is assumed and suppressed through the paper.

## II. KA-BAND ANTENNA

The Ka-band FSS-backed reflectarray antenna is designed using a phase-only synthesis and analyzed assuming local periodicity [15], thus the investigations are divided into two parts: the element optimization, and the reflectarray design and analysis. The element is investigated using the commercial software Ansys Designer [16] employing periodic boundaries and plane wave excitation. The reflectarray design is carried out using an in-house developed numerical tool, that calculates the associated far-field by the equivalent currents technique [17, technique II].

### A. Element Design

Due to the large frequency separation between the 20 GHz RX and 30 GHz TX bands, the required phase shifts at the RX and TX frequencies over the reflectarray aperture become very different which makes it impractical to cover both bands by a single broadband element [4]. Thus, it is desired to adjust the phase over the reflectarray aperture independently in the two frequency bands. For this purpose, interleaved element grids are often applied to design multi-band reflectarray antennas [9], [18], [19]. However, when using an interleaved element grid, the inter-element spacing may become undesirably large, which can cause grating lobes [3], and the reflectarray bandwidth is reduced [20], [21]. Interleaved dual split-loop elements have previously been utilized for dual-band reflectarrays [22], however, in this paper we propose a more compact concentric layout. By doing this, grating lobes are avoided and the inter-element coupling in both operating bands is inherently included in the simulation model. The reflectarray and FSS elements are located in a coinciding square array grid with square unit cell side length of 5 mm, thus the reflectarray and FSS elements are included in the same simulation model.

TABLE I  
REFLECTARRAY ELEMENT GEOMETRY DATA.

$(r_o, r_i)$	(2.3 mm, 1.9 mm)
$(r_o^{fss}, r_i^{fss})$	(2.1 mm, 1.6 mm)
Array grid	5 mm × 5 mm
Dielectric thickness	0.787 mm
Rogers Duroid 5880	$\epsilon_r = 2.2, \tan \delta = 0.0009$

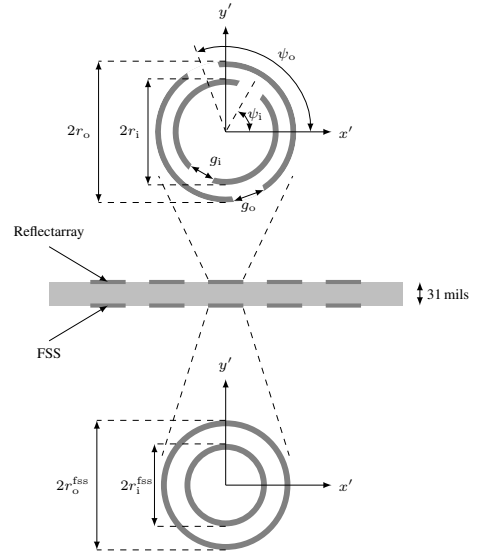


Fig. 2. Geometry of the concentric dual split-loop reflectarray element and the concentric dual-loop FSS element, in the local  $x', y'$  coordinate system.

In this reflectarray antenna design, the concentric dual split-loop element is utilized [23], depicted in Fig. 2. The element consists of two concentric split-loops, which are characterized by their radii  $r_o$  and  $r_i$ , respectively, measured from the center to the outside of the conductor, the rotation angles  $\psi_o$  and  $\psi_i$ , and the gap sizes  $g_o$  and  $g_i$ . The FSS elements consist of concentric dual-loops characterized by the radii  $r_o^{fss}$  and  $r_i^{fss}$ . All loops are of equal trace width 0.2 mm, and the element dimensions are given in Table I.

The present design utilizes the variable rotation technique (VRT) [24], where the phase of the circularly polarized reflected field is adjusted by rotation of the element. Using the concentric dual split-loop element, the phase of the reflected field can be adjusted at 19.95 and 29.75 GHz simultaneously, by rotation of the outer and inner split-loops, respectively. However, for each set of rotation angles ( $\psi_o, \psi_i$ ) the element must be optimized to maximize the magnitude of the co-polar reflection coefficient, i.e. LHCP to LHCP ( $R_{ll}$ ) at 19.95 GHz and RHCP to RHCP ( $R_{rr}$ ) at 29.75 GHz. This is done by adjusting  $g_o$  and  $g_i$ .

The element optimization is carried out on the free-standing reflectarray substrate, i.e. no support structure is included in the analysis model. For a finite number of rotation angles  $\psi_o$  and  $\psi_i$ ,  $g_o$  and  $g_i$  are optimized to maximize  $|R_{ll}|$  at 19.95 GHz and  $|R_{rr}|$  at 29.75 GHz. The optimization is carried out for a plane wave incident angles  $\phi = 0^\circ$  and  $\theta = 30^\circ$ , which is the incidence angles at the center of the reflectarray to be designed.

At 19.95 GHz,  $|R_{ll}|$  varies between  $-0.7$  and  $-0.3$  dB for all combinations of  $\psi_o$  and  $\psi_i$ , while the average cross-polar reflection is  $-23$  dB. At 29.75 GHz,  $|R_{rr}|$  is in the order of

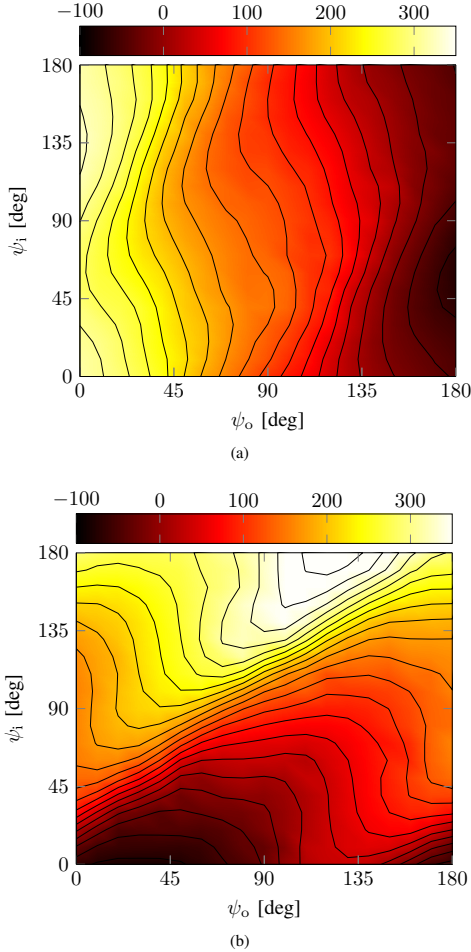


Fig. 3. Phase of (a)  $R_{11}$  at 19.95 GHz and (b)  $R_{rr}$  at 29.75 GHz, for the incidence angles  $\phi = 0$  and  $\theta = 30^\circ$ . Contour curves are shown to highlight the behavior.

$-0.5$  dB for most rotation angles, however, for  $\psi_o \approx \psi_i$ ,  $|R_{rr}|$  is close to  $-1.5$  dB. The average cross-polar reflection is  $-20$  dB. This means that for some rotation angles of the concentric dual split-loops, part of the power is transmitted through the reflectarray and will be scattered by the L-band antenna located behind as well as by the reflectarray support structure. The performance may be further improved by including more geometry variables in the optimization as e.g. the radii of the split-loops, however, at the expense of computation time.

The phase of the co-polar reflection coefficients, i.e.  $\angle R_{11}$  at 19.95 GHz and  $\angle R_{rr}$  at 29.75 GHz, are shown in Fig. 3. At 19.95 GHz,  $360^\circ$  phase variation is achieved when adjusting  $\psi_o$ , but varies within  $\pm 25^\circ$  when  $\psi_i$  is varied. Similarly, at 29.75 GHz,  $360^\circ$  phase variation is achieved when adjusting

$\psi_i$ , however, the phase changes up to  $\pm 90^\circ$  when varying  $\psi_o$ . The dependence of each reflection coefficient,  $R_{11}$  and  $R_{rr}$ , on both split-loop orientation angles,  $\psi_o$  and  $\psi_i$ , is handled properly by the reflectarray design procedure. Thus the reflection coefficients,  $R_{11}$  at 19.95 GHz and  $R_{rr}$  at 29.75 GHz, depend not only on the rotation angle of the outer and inner split-loops,  $\psi_o$  and  $\psi_i$  respectively, but also the rotation angle of the other split-loop: for  $R_{11}$  this mutual dependence on  $\psi_i$  is small while for  $R_{rr}$  it is noticeable larger. This behavior is much more pronounced, compared to the case of concentric dual split-loops on a conventional solid ground-plane [25], where  $R_{11}$  at 19.95 GHz is almost independent of  $\psi_i$ .

The optimized element geometries are subsequently analyzed for a discrete set of incidence angles that covers the angles needed in the reflectarray design, here  $\phi \in [0^\circ; 360^\circ]$  and  $\theta \in [0^\circ; 60^\circ]$  in steps of  $15^\circ$  and  $10^\circ$ , respectively. The data forms a 4-dimensional lookup table ( $\phi, \theta, \psi_o, \psi_i$ ), which is interfaced to the reflectarray design tool.

### B. Reflectarray Design

To minimize scattering from the feeding antenna, an offset configuration has been chosen where the feeding antenna is located 300 mm from the reflectarray center, in the direction  $\phi = 0^\circ$  and  $\theta = 30^\circ$  in the coordinate system of Fig. 1. The reflectarray antenna is designed to obtain a collimated beam in the specular direction, i.e.  $\phi = 180^\circ$  and  $\theta = 30^\circ$ , at 19.95 and 29.75 GHz. The reflectarray data are summarized in Table II.

The reflectarray is printed on a  $40 \times 40$  cm<sup>2</sup> Rogers Duroid 5880 substrate of 0.787 mm thickness, with  $\epsilon_r = 2.2$  and  $\tan \delta = 0.0009$ . To ensure mechanical stability and approximate free-standing conditions, i.e. minimum influence of the antenna support structure, the reflectarray is mounted on a 70 mm thick block of Rohacell 51 HF with  $\epsilon_r = 1.08$  and  $\tan \delta = 0.0021$ . The Rohacell is attached to a rigid aluminum honeycomb plate that is part of the antenna support structure.

A corrugated horn antenna with integrated diplexer and polarizer is used as feeding antenna, and the horn has been modeled in the commercial software CHAMP [26]. This model has been used to calculate the near-field of the feeding horn antenna, which is used for the reflectarray design. The directivity of the utilized horn antenna is 15.7 and 13.2 dBi, at 19.95 and 29.75 GHz, respectively, which provides an edge illumination in the range of  $-20$  to  $-5$  dB, relative to the maximum in the reflectarray aperture.

A design procedure has been developed and implemented in a numerical tool, where first  $\psi_o$  is adjusted to obtain the desired reflection phase at 19.95 GHz, and thereafter  $\psi_i$  to obtain the desired reflection phase at 29.75 GHz. Due to

TABLE II  
OFFSET REFLECTARRAY ANTENNA DATA.

RX frequencies	19.7 GHz – 20.2 GHz LHCP
TX frequencies	29.5 GHz – 30.0 GHz RHCP
Reflectarray dimensions	400 mm $\times$ 400 mm
Feed distance to center of array	300 mm
Feed offset angle	$\phi = 0^\circ, \theta = 30^\circ$
Direction of mainbeam	$\phi = 180^\circ, \theta = 30^\circ$

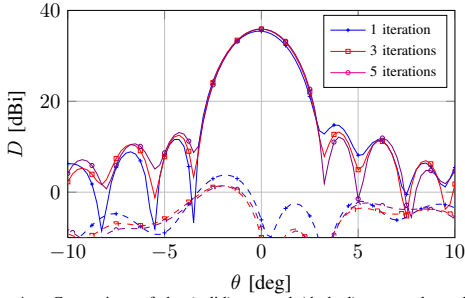


Fig. 4. Comparison of the (solid) co- and (dashed) cross-polar radiation pattern of 1, 3 and 5 iterations of the reflectarray design, at 19.95 GHz in the offset plane.

the reflection coefficients at both design frequencies being dependent on both  $\psi_o$  and  $\psi_i$ , these steps are repeated, thus forming the iterative design procedure that consists of the following steps:

- 1) The reflectarray unit element is optimized with respect to cross-polar suppression and the scattering matrices are stored
- 2) The design tool is initialized with  $\psi_o = \psi_i = 0^\circ$  for all elements
- 3) A 1-dimensional phase-curve of  $R_{ll}$  at 19.95 GHz is generated using local values of  $(\phi, \theta, \psi_i)$ , from which  $\psi_o$  is determined
- 4) A 1-dimensional phase-curve of  $R_{rr}$  at 29.75 GHz is generated using local values of  $(\phi, \theta, \psi_o)$ , from which  $\psi_i$  is determined
- Step 3 and step 4 may be repeated if necessary
- 5) The scattered aperture field is determined by interpolation of the reflection matrix
- 6) The radiated far-field is calculated by equivalent currents technique

Due to the reflection coefficients at both design frequencies being dependent on both  $\psi_o$  and  $\psi_i$ , step 3 and 4 may be repeated, thus forming the iterative design procedure.

The benefit of the iterative design procedure is demonstrated in Fig. 4, where the radiation patterns of the reflectarray at 19.95 GHz, after 1, 3 and 5 iterations are depicted. The maximum directivity is increased by 0.6 dB, and the cross polarization is lowered by 2.4 dB. The changes in the radiation pattern at 29.75 GHz are negligible since the elements are always optimized at this frequency in the last step.

The reflectarray support structure was manufactured at the mechanical workshop at the Technical University of Denmark, and is depicted in Fig. 5, with a zoom of the PCB top layer. The radiation pattern coordinate system is oriented with the  $z$ -axis in the direction of the main beam and the  $x$ -axis is in the plane that contains the main beam and the feeding antenna.

### C. Reflectarray Radiation

The Ka-band FSS-backed reflectarray antenna was measured in 0.1 GHz resolution in the frequency bands 19.5 – 20.4 GHz and 29.3 – 30.2 GHz. The reflectarray support structure depicted in Fig. 5 was utilized, and the L-band antenna

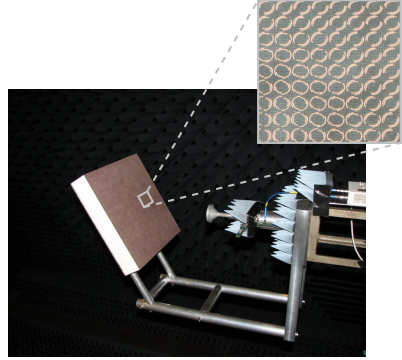


Fig. 5. Offset FSS-backed reflectarray antenna in the DTU-ESA Spherical Near-Field Antenna Test Facility.

was not included in these measurements. The measured radiation patterns of the reflectarray at 20.0 GHz are depicted in Fig. 6a in the offset plane, and in Fig. 6b in the transverse plane. The maximum directivity is 36.4 dBi. The side lobe and cross polarization levels are 21.4 dB and 30.6 dB below the maximum directivity. The loss measured at the input of the diplexer is 1.1 dB  $\pm$  0.4 dB across the band.

In Fig. 7a and Fig. 7b, the radiation patterns at 29.8 GHz are depicted in the offset and transverse plane, respectively. Here, the maximum directivity is 38.5 dBi, and the side lobe level and cross polarization levels are 16.2 dB and 24.1 dB below that. The measured loss is 0.8 dB  $\pm$  0.4 dB across the band.

Fig. 8 presents the maximum directivity and on-axis axial-ratio (AR) over the RX and TX frequency bands. In the RX frequency band, the minimum directivity is 36.0 dBi and the AR is below 0.8 dB. The aperture illumination efficiency is 53 to 57 %, which is similar to the performance obtained using a solid ground-plane [25]. In the TX frequency band, the minimum directivity is 37.5 dBi, and the on-axis AR is below 1.8 dB. The aperture illumination efficiency is in the range of 32 to 48 %. This is, however, worse than the performance of the solid ground-plane reflectarray in [25]. This owes to power being transmitted through the FSS ground-plane, as described in Section II-A, which is then reflected from the aluminum mounting plate behind the Rohacell. This power is then scattered in different directions through the sides of the Rohacell and adds to the far-field in different phases depending on the frequency, which is seen by variation in the maximum directivity over frequency, in Fig. 8b. Thus, the reflectarray performance in the TX frequency band should be improved by further optimization of the reflectarray and FSS elements, to maximize the magnitude of the co-polar reflection coefficient, i.e.  $|R_{rr}|$  at 29.75 GHz. This may be achieved by including the radii of the both the split-loops and the radii of the FSS loops into optimization.

### III. L-BAND PERFORMANCE

To validate the transparency of the FSS-backed reflectarray, a second measurement setup has been manufactured with an

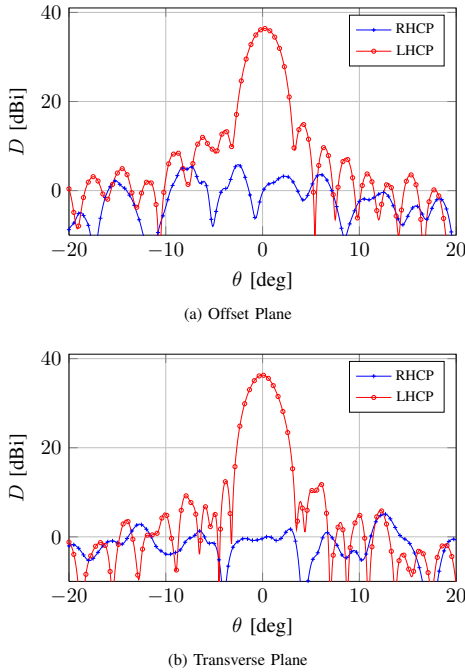


Fig. 6. Measured directivity pattern of the FSS-backed reflectarray antenna at 20.0 GHz, in the offset and transverse plane.

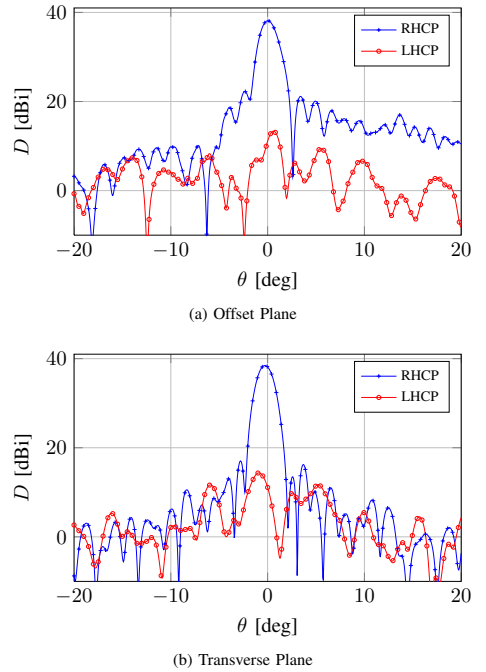


Fig. 7. Measured directivity pattern of the FSS-backed reflectarray antenna at 29.8 GHz, in the offset and transverse plane.

L-band antenna located behind the reflectarray, see Fig. 9. The L-band antenna is a commercial four-patch array antenna for satellite communication in the Inmarsat Broadband Global Area Network (BGAN) [27], which has not been designed for this specific application. This antenna is located on an aluminum mounting plate, on which the Ka-band FSS-backed reflectarray is held by the Rohacell structure seen in Fig. 9.

The radiation pattern of the L-band antenna mounted on the aluminum support structure has been measured with and without the FSS-backed reflectarray in front. The measurement without the FSS-backed reflectarray in front serves as the reference when observing the impact of the FSS-backed reflectarray.

The radiation patterns of both measurements, at 1.643 GHz in the  $\phi = 0^\circ$  plane, are shown in Fig. 10. The maximum directivity of the antenna with the FSS-backed reflectarray in front is 12.2, which is 0.1 dB lower than the reference. The maximum cross polarization level is 13.3 dB below the maximum directivity, which is 0.8 dB higher than to the reference. The side lobe level at  $\theta = -70^\circ$  rises by 0.7 dB, while the side lobe level at  $\theta = 70^\circ$  decrease by 0.4 dB. Similar influence on the radiation patterns has been observed in the entire far-field sphere.

The measurements were conducted from 1,500 to 1,700 MHz, and the directivity varies within  $\pm 0.15$  dB of the reference, and the maximum cross polarization varies less than  $\pm 2.5$  dB. The measured input reflection coefficient

of the four-patch array antenna is depicted in Fig. 11. The maximum reflection coefficient of the antenna behind the FSS-backed reflectarray is  $-17$  dB, which is slightly worse than the reference measurement of  $-17.9$  dB. Only minor changes are observed over the measured frequency band.

It should be noted that the L-band antenna has a footprint of only  $22 \times 22 \text{ cm}^2$  which is approximately  $1/4$  of the available area. The L-band antenna can thus be enlarged accordingly to utilize the available area, i.e.  $40 \times 40 \text{ cm}^2$ , which should improve the maximum directivity by up to 6 dB. In the presented antenna demonstrator, the L-band antenna is radiating orthogonally through the Ka-band reflectarray, but for the final antenna, the L- and Ka-band beams should be collocated.

#### IV. CONCLUSION

To combine high-speed data communication at Ka-band with a stable L-band data link, a shared aperture antenna, comprising a Ka-band FSS-backed reflectarray and an L-band patch array antenna, has been proposed and presented. The reflectarray is designed using a concentric dual split-loop element optimized for maximum co-polar reflection and a dedicated iterative design tool for the reflectarray layout. Due to the complex phase characteristics of the element, an iterative design procedure has been developed and presented, which improves the radiation pattern of the reflectarray.

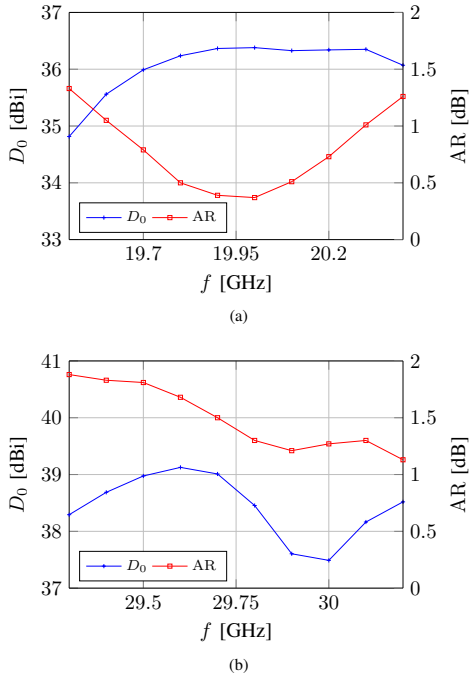


Fig. 8. The co-polar directivity and the on-axis AR of the FSS-backed reflectarray in (a) the RX and (b) the TX frequency bands, in the  $\phi = 0^\circ$  plane.

The Ka-band performance of the FSS-backed reflectarray has been validated by measurements in the DTU-ESA Spherical Near-Field Antenna Test Facility. At the RX and TX center frequencies aperture illumination efficiencies of 56 and 41 % are obtained.

An existing commercial L-band patch array antenna was used to demonstrate the L-band transparency of the FSS-backed reflectarray antenna. The measurements showed that the impacts on both the radiation and the reflection coefficient of the L-band antenna, when placing the FSS-backed reflectarray in front, are negligible.

In conclusion, the numerical and experimental study presented here demonstrates that the proposed concept of a shared-aperture L- and Ka-band antenna, employing an FSS-backed dual-frequency reflectarray for the Ka-band in front of a patch-array antenna for the L-band, has proven viable. The obtained performance results are satisfactory and can even be further improved in the final design.

#### REFERENCES

- [1] F. Gargione, T. Iida, F. Valdoni, and F. Vatalaro, "Services, technologies, and systems at ka band and beyond-a survey," *IEEE J. Select. Areas Commun.*, vol. 17, no. 2, pp. 133–144, 1999.
- [2] B. R. Elbert, *The Satellite Communication Applications Handbook*, 2nd ed. Artech House, 2004.
- [3] J. Huang and J. A. Encinar, *Reflectarray Antennas*. IEEE Press, 2008.
- [4] D. M. Pozar, "Bandwidth of reflectarrays," *Electron. Lett.*, vol. 39, no. 21, pp. 1490–1491, 2003.

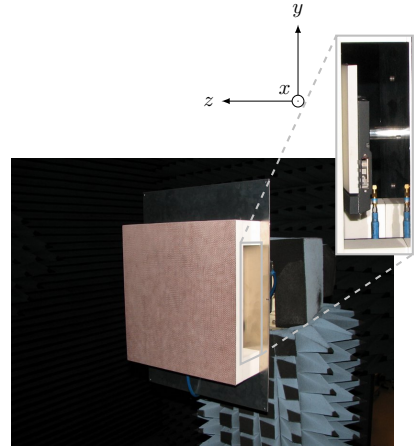


Fig. 9. L-band patch array antenna behind the FSS-backed reflectarray. The radiation pattern coordinate system is located with the z-axis orthogonal to the reflectarray, and the x-axis is in the horizontal plane.

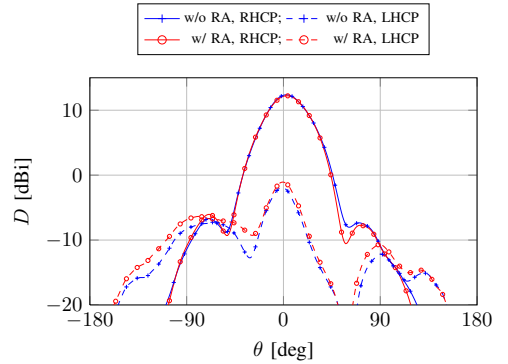


Fig. 10. Radiation pattern of the L-band four-patch array antenna, with (w/ RA) and without (w/o RA) the FSS-backed reflectarray in front, at 1,643 MHz in the  $\phi = 0^\circ$  plane in the coordinate system specified in Fig. 9.

- [5] K. Mayumi, H. Deguchi, and M. Tsuji, "Wideband single-layer microstrip reflectarray based on multiple-resonance behavior," in *IEEE AP-S Int. Symp.*. IEEE, Jul. 2008, pp. 1–4.
- [6] A. Yu, F. Yang, A. Elsherbeni, and J. Huang, "Design and measurement of a circularly polarized Ka-band reflectarray antenna," in *Proc. EuCAP*, 2009, pp. 2769–2773.
- [7] D. Wu, R. Hall, and J. Huang, "Dual-frequency microstrip reflectarray," in *IEEE AP-S Int. Symp.*, vol. 4, 1995, pp. 2128–2131 vol.4.
- [8] J. A. Encinar, "Design of a dual frequency reflectarray using microstrip stacked patches of variable size," *Electron. Lett.*, vol. 32, no. 12, pp. 1049–1050, 1996.
- [9] M. R. Chaharmir, J. Shaker, N. Gagnon, and D. Lee, "Design of broadband, single layer dual-band large reflectarray using multi open loop elements," *IEEE Trans. Antennas Propag.*, vol. 58, no. 9, pp. 2875–2883, Sep. 2010.
- [10] A. Yu, F. Yang, A. Elsherbeni, J. Huang, and Y. Kim, "An offset-fed x-band reflectarray antenna using a modified element rotation technique," *IEEE Trans. Antennas Propag.*, vol. 60, no. 3, pp. 1619–1624, Mar. 2012.
- [11] C. Han, C. Rodenbeck, J. Huang, and K. Chang, "A C/Ka dual frequency

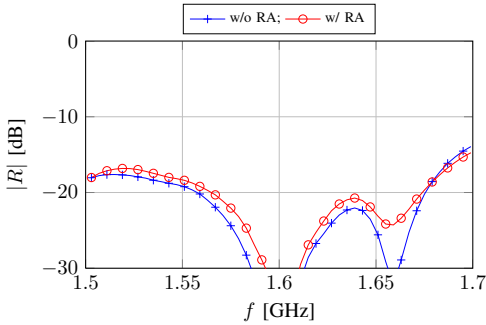


Fig. 11. Measured reflection coefficient of the L-band patch array antenna, without (w/o RA) and with (w/ RA) the FSS-backed reflectarray in front.

- dual layer circularly polarized reflectarray antenna with microstrip ring elements," *IEEE Trans. Antennas Propag.*, vol. 52, pp. 2871–2876, 2004.
- [12] J. Shaker and M. Cuhaci, "Multi-band, multi-polarisation reflector-reflectorarray antenna with simplified feed system and mutually independent radiation patterns," *IEE Proc. Microw. Antennas Propag.*, vol. 152, no. 2, pp. 97–101, 2005.
- [13] M. Chaharmir, J. Shaker, and H. Legay, "Dual-band Ka/X reflectarray with broadband loop elements," *IET Microw. Antennas Propag.*, vol. 4, p. 225, 2010.
- [14] "Explorer 500," <http://www.cobham.com/about-cobham/aerospace-and-security/about-us/satcom/lyngby/products/land-based-satcom-communications/explorer-500.aspx>.
- [15] J. Encinar and J. Zornoza, "Three-layer printed reflectarrays for contoured beam space applications," *IEEE Trans. Antennas Propag.*, vol. 52, no. 5, pp. 1138–1148, 2004.
- [16] "Ansys Designer," <http://www.ansys.com>.
- [17] M. Zhou, S. Sorensen, E. Jorgensen, P. Meincke, O. Kim, and O. Breinbjerg, "An accurate technique for calculation of radiation from printed reflectarrays," *IEEE Antennas Wireless Propag. Lett.*, vol. 10, pp. 1081–1084, 2011.
- [18] E. B. Felstead, J. Shaker, M. R. Chaharmir, and A. Petosa, "Enhancing multiple-aperture ka-band navy SATCOM antennas with electronic tracking and reflectarrays," in *Proc. MILCOM*, ser. 1, vol. 2002. IEEE, Oct. 2002, pp. 168–172.
- [19] F. Yang, Y. Kim, J. Huang, and A. Elsherbeni, "A single-layer tri-band reflectarray antenna design," in *IEEE AP-S Int. Symp.*, 2007, pp. 5307–5310.
- [20] D. Pozar, "Wideband reflectarrays using artificial impedance surfaces," *Electron. Lett.*, vol. 43, no. 3, pp. 148–149, 2007.
- [21] G. Zhao, Y.-C. Jiao, F. Zhang, and F.-S. Zhang, "A subwavelength element for broadband circularly polarized reflectarrays," *IEEE Antennas Wireless Propag. Lett.*, vol. 9, pp. 330–333, 2010.
- [22] C. Guclu, J. Perruisseau-Carrier, and O. Civi, "Proof of concept of a dual-band circularly-polarized RF MEMS beam-switching reflectarray," *IEEE Trans. Antennas Propag.*, vol. 60, no. 11, pp. 5451–5455, Nov. 2012.
- [23] T. Smith, N. V. Larsen, U. V. Gothelf, O. S. Kim, and O. Breinbjerg, "20/30 ghz dual-band circularly polarized reflectarray antenna based on the concentric dual split-loop element," in *Proc. ESA Antenna Week*, 2012.
- [24] J. Huang and R. Pogorzelski, "A Ka-band microstrip reflectarray with elements having variable rotation angles," *IEEE Trans. Antennas Propag.*, vol. 46, no. 5, pp. 650–656, 1998.
- [25] T. Smith, U. V. Gothelf, O. S. Kim, and O. Breinbjerg, "Design, manufacturing, and testing of a 20/30 ghz dual-band circularly polarized reflectarray antenna," *IEEE Antennas Wireless Propag. Lett.*, 2013, in Submission.
- [26] "TICRA CHAMP," <http://www.ticra.com/products/software/champ>.
- [27] "Inmarsat BGAN," <http://www.inmarsat.com/services/bgan>.



## CONFERENCE PAPER I

---

# INVESTIGATION OF BACKFIRE MONOFILAR HELICAL ANTENNA

Thomas Smith, Niels Larsen, Ulrich Gothelf,  
Oleksiy S. Kim, and Olav Breinbjerg

*Status*

Presented: April 2011

### **Bibliography**

- [C1] T. Smith, N. Larsen, U. Gothelf, O. S. Kim, and O. Breinbjerg, "Investigation of Backfire Monofilar Helical Antenna," *Proc. EuCAP.*, pp. 1511–1510, 2011.





# Investigation of Backfire Monofilar Helical Antenna

Thomas Gunst Smith<sup>\*†</sup>, Niels Vesterdal Larsen<sup>\*</sup>, Ulrich Vesterager Gothelf<sup>\*</sup>,  
Oleksiy S. Kim<sup>†</sup>, Olav Breinbjerg<sup>†</sup>

<sup>\*</sup>Thrane & Thrane A/S

Lundtoftegårdsvej 93D, DK-2800 Kgs. Lyngby, Denmark.

<sup>†</sup>Department of Electrical Engineering, Electromagnetic Systems, Technical University of Denmark  
Ørstedes Plads, Building 348, DK-2800 Kgs. Lyngby, Denmark

**Abstract**—This paper presents a numerical investigation of the electromagnetic properties of the backfire monofilar helical antenna. The current distribution along the helical conductor, the input impedance, and the front-to-back ratio are calculated and analyzed for the backfire operation of the antenna. A parametric study of the helical geometry and the resulting antenna characteristics will be described and discussed. The currents and fields are calculated using the simulation software AWAS based on the Method of Moments with a wire representation of the ground plane.

## I. INTRODUCTION

Helical antennas have been used for more than half a century and are popular due to their wideband operation. In most applications, the helical antenna is operated in either the axial or normal mode and this is primarily determined by the circumference of the helix,  $C_h$ . The axial mode is excited when  $C_h \approx \lambda_0$ , where  $\lambda_0$  is the free space wavelength, and the normal mode is excited when  $C_h \ll \lambda_0$  [1]–[3]. When excited in the axial mode, the helix can be modelled as being located on an infinite ground plane, however, empirical results show that the axial mode is excited for helical antennas with ground plane diameter down to twice the diameter of the helix [1], [4]. When the diameter of the ground plane is decreased to the diameter of the helix or smaller, a backfire operating mode can be excited [5]. The present paper elaborates on the results given in [5] to yield a thorough understanding of the backfire radiating mode of the monofilar helical antenna, and thus forms a solid basis for the design of backfire monofilar helical antennas.

The current distribution on the antenna is calculated using AWAS, which is based on a Method of Moment formulation with a piecewise linear thin-wire approximation and delta-gap excitation [6]. The influence of the helix and ground plane radii on the axial mode and backfire operation of the helical antenna is described. Subsequently, a parametric study of the influence of the helix diameter and the spacing between turns is presented. Radiation characteristics such as the directivity and front-to-back (F/B) ratio are calculated and discussed, and the results are presented in a way that easily illustrates the influence of the geometrical parameters defined in Fig. 1. From these results, the set of parameters ( $r_g, r_h, S$ ) leading to maximum directivity and/or F/B ratio are deduced. The impedance of the backfire helical antenna is examined as well, and it is found that the frequency dependence is very similar

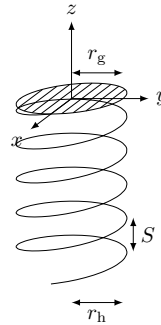


Fig. 1. Backfire monofilar helical antenna geometry and coordinate system.

to that of the axial mode helical antenna described in [1]. It is shown that, in similarity with the axial mode helical antenna, an impedance bandwidth exceeding 50 % can be obtained for the backfire helical antenna.

The geometric parameters are depicted in Fig. 1, where  $S$  is the spacing between turns, and  $r_h$  and  $r_g$  are the radii of the helix and ground plane, respectively. The radius of the conductor is denoted  $a$  and the number of turns  $n$ . For these investigations, the conductor radius is fixed at  $a = 0.0025\lambda_0$ , which satisfies the assumptions for thin-wire approximation of the conductor. For these investigations a peripheral excitation is used; for helical antennas with a ground plane diameter larger than or equal to the helix diameter, the excitation is located on the helix periphery. For ground plane diameters smaller than the helix diameter, the two are connected by a straight wire, and the excitation is located at the ground plane periphery.

The coordinate system is oriented such that the positive  $z$ -axis is in the direction of backfire radiation, hence the F/B ratio is defined as

$$F/B = \frac{D(\theta = 0^\circ)}{D(\theta = 180^\circ)}, \quad (1)$$

where  $D$  is the directivity of the antenna.

## II. THE BACKFIRE MODE

The parameters defined in Fig. 1 determine the impedance and radiating characteristics of the helical antenna, and will

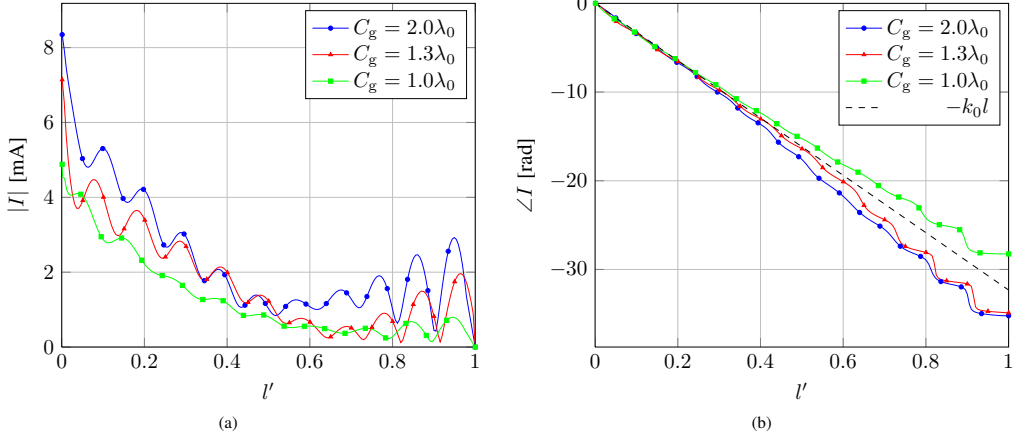


Fig. 2. (a) Amplitude and (b) phase of electric current along normalized conductor length  $l'$  with 1 V delta-gap excitation. --- is the free space phase progression with wave number  $k_0$ .

be thoroughly investigated in Section III. For now, the helical antenna to be examined is characterized by  $n = 5$ ,  $C_h = 1.0\lambda_0$  and  $S = 0.15\lambda_0$ .

#### A. Current Distribution

When excited in the axial mode, the helical antenna can be modelled as being located on an infinite ground plane, however, the axial mode radiation may be excited for ground plane diameters as small as two times the diameter of the helix [1]. The current distribution along the helical conductor in the three cases where  $C_g = 2.0\lambda_0$ ,  $1.3\lambda_0$  and  $1.0\lambda_0$ ,  $C_g$  being the circumference of the ground plane, has been calculated and is depicted in Fig. 2.

For the case  $C_g = 2.0\lambda_0$ , the current distribution can be divided into a decaying region ( $0 \leq l' \lesssim 0.5$ ) and a standing wave region ( $0.5 \lesssim l'$ ),  $l'$  being the normalized conductor length. A standing wave is also present over the decaying region of the conductor, however, the Standing-Wave-Ratio (SWR) is small. The standing wave pattern may also be described by the interaction of the forward propagating wave, and the reflected backwards propagating wave. The power reaching the end of the conductor is reflected and results in ripples in the current amplitude, as seen in Fig. 2a, and the constant phase level in Fig. 2b. This indicates a pure standing wave.

A commonly used method of interpreting the radiation from helical antennas is by modelling the helix as an array of single-turn elements. In this way, the progressive phase  $\psi$  of each element may be formulated by [1]

$$-\psi = k_0 \left( S \cos \theta + \frac{L}{p} \right) \quad (2a)$$

where  $k_0$  is the wave number in free space,  $L = \sqrt{C_h^2 + S^2}$  is the length of one helix turn, and  $p$  is the relative phase

velocity of the wave along the conductor with respect to the phase velocity in free space. For the fields to add in-phase,  $\psi = -2\pi$  inserted in (2a) yields

$$p = \frac{L}{\lambda_0 - S \cos \theta}. \quad (2b)$$

The phase of the electric current on the conductor may be expressed as  $-kl$ , where  $k$  is the wave number of the wave propagating along the conductor as plotted in Fig. 2b. The phase progression in free space,  $-k_0l$ , is plotted as reference. The relative phase velocity may be expressed by [2]

$$p = \frac{k_0}{k}, \quad (3)$$

and observing Fig. 2b, it is apparent that the wave propagating along the conductor in the case  $C_g = 2.0\lambda_0$  is a slow wave, that is the phase velocity is lower than that of free space. This agrees with (2b), which for in-phase fields in the axial mode direction ( $\theta = 180^\circ$ ) yields a relative phase velocity less than unity for this particular choice of  $C_h$  and  $S$ . The radiation pattern of the helical antenna with  $C_g = 2\lambda_0$  is depicted in Fig. 3a, and the antenna radiates in the axial mode direction as expected. In this paper, the axial mode direction refers to the  $\theta = 180^\circ$  direction, to be consistent with the notation in literature [1], [2].

When the diameter of the ground plane is equal to the diameter of the helix, that is  $C_g = 1.0\lambda_0$ , the helical antenna radiates in the backfire direction ( $\theta = 0^\circ$ ) as seen in Fig. 3c. In Fig. 2a it is seen that the decaying region now occupies a larger portion of the helical conductor and the standing wave region is reduced to the  $0.75 \lesssim l'$  region. The SWR over the decaying region is also decreased.

Observing (3) and Fig. 2b, it is noted that the wave propagating along the helical conductor is a fast wave. This satisfies (2b) for in-phase fields in the  $\theta = 0^\circ$  direction, that

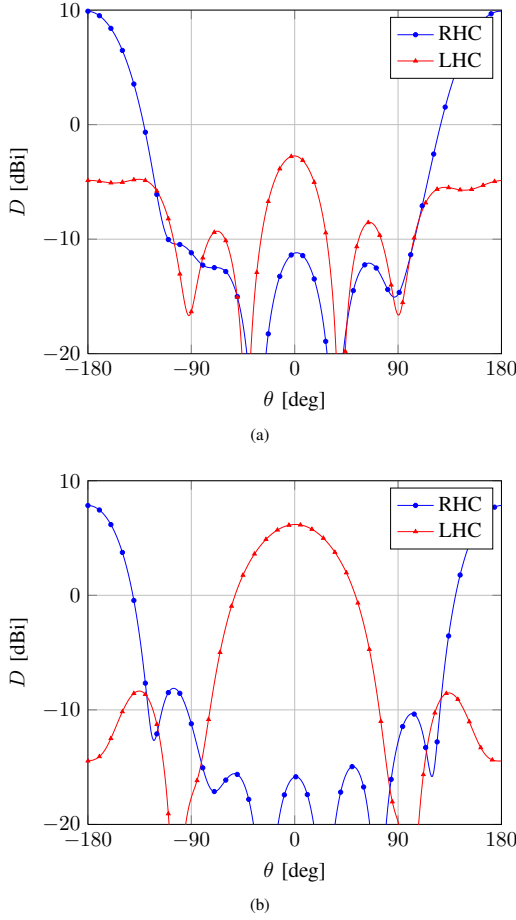


Fig. 3. Radiation pattern of helical antenna with ground plane circumference (a)  $2.0\lambda$  and (b)  $1.3\lambda$ , in the cut  $\phi = 0^\circ$ .

is, the relative phase velocity is greater than unity. For this particular configuration of the backfire helical antenna, an F/B ratio of 21.4 dB is observed in Fig. 3c.

For a fixed set of  $C_h$  and  $S$ , both axial mode and backfire radiation can be obtained by adjusting the size of the ground plane, as exemplified in the above cases. By proper choice of ground plane diameter, it is possible to achieve equal directivity in both the axial mode and backfire direction. For the present case of  $C_h = 1.0\lambda$  and  $S = 0.15\lambda$ , this happens when  $C_g = 1.3\lambda$ , and the current distribution is shown in Fig. 2. The characteristics are a combination of the axial mode and backfire helical antennas, that is, the decaying region extends over  $0 \leq l' \lesssim 0.65$  in which  $p \approx 1$ . The radiation pattern is depicted in Fig. 3b, where an F/B ratio of 0.2 dB is observed. It is seen that the sense of circular polarization is opposite in the axial mode and backfire direction, which is

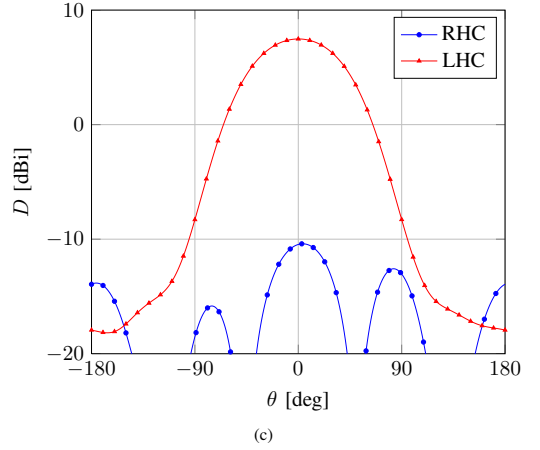


Fig. 3. Radiation pattern of helical antenna with ground plane circumference (c)  $1.0\lambda$ , in the cut  $\phi = 0^\circ$ .

also observed with Fig. 3, where the axial mode antenna is Right Hand Circular (RHC) and the backfire helical antenna is Left Hand Circular (LHC), however, this may not always be the case.

### B. Impedance

The input impedance of the backfire helical antenna has been calculated for different configurations, which are characterized by  $n = 5$  and  $C_g = C_h = 1.0\lambda_0$ . For the three cases  $S = 0.10\lambda_0$ ,  $0.15\lambda_0$  and  $0.20\lambda_0$ , the impedance is depicted in Fig. 4. The backfire helical antenna is seen to exhibit wideband impedance characteristics similar to the axial mode helical antenna. For the three cases, bandwidths of 36 %, 51 % and 64 % are obtained with return loss better than 15 dB by a simple two-component match to  $50 \Omega$ .

## III. PARAMETRIC STUDY

In Section II, a backfire helical antenna was compared to an axial mode helical antenna. To investigate the influence of the geometry on the backfire helical antenna, a parametric study has been conducted. For the backfire helical antenna, the directivity in the direction of backfire radiation and F/B ratio are the main parameters of interest.

### A. Ground Plane Size

For a fixed set of  $S$  and  $C_h$  both axial mode and backfire operation of the helical antenna have been demonstrated, by varying the ground plane size. This has lead to a survey of the influence of the ground plane size on the radiation pattern, in the antenna configurations where  $C_h = 1.0\lambda_0$  and  $S = 0.10\lambda_0$ ,  $0.15\lambda_0$  and  $0.20\lambda_0$ . The results are summarized in Fig. 5, where the backfire directivity ( $\theta = 0^\circ$ ) and F/B ratio are depicted.

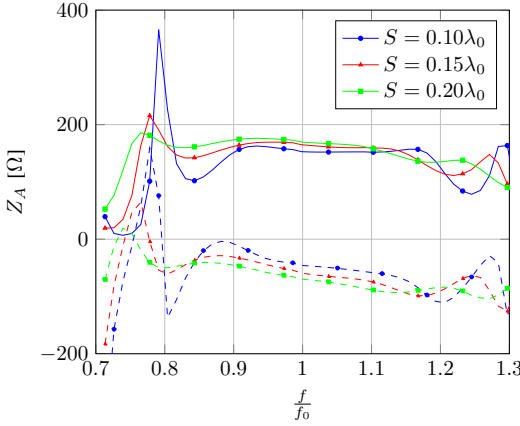


Fig. 4. Input — resistance and - - - reactance of backfire helical antenna over normalized frequency range,  $C_g = C_h = 1.0\lambda_0$ .

For all three antenna configurations, it is found that maximum backfire directivity is achieved when  $C_g$  is between  $1.0\lambda_0$  and  $1.1\lambda_0$ , and maximum F/B ratio for  $C_g$  between  $0.9\lambda_0$  and  $1.1\lambda_0$ . It is noted that for all cases the helical antenna has the same directivity in the backfire and axial mode direction when  $C_g = 1.3\lambda_0$ , see Fig. 5b. Hence for helical antennas with a ground plane diameter less than  $0.4\lambda_0$ , the antenna radiates in the backfire direction. For helical antennas with a ground plane diameters larger than  $0.4\lambda_0$  the antenna radiates the axial mode direction, which is close to the empirical rule-of-thumb that the ground plane diameter must be larger than  $0.5\lambda_0$  [1].

### B. Helix Parameters

Based on the results in Section III-A, the ground plane diameter is now fixed to equal the diameter of the helix. For a fixed number of turns,  $n = 5$ , the helix can be characterized by two parameters only, namely  $S$  and  $C_h$ . The influence of these parameters on particularly the backfire directivity and the F/B ratio has been investigated, and the results are shown in Fig. 6. The black lines in the figures are constant  $S/C_h$  ratios. Observations along these lines are equivalent to frequency sweeps, that is, the electrical size of the helix scales linearly in all three parameters ( $S, C_h, C_g$ ).

For spacings  $S$  between turns in the order of  $0.1\lambda_0$ , maximum directivity is achieved when the circumference of the helix is between  $0.8\lambda_0$  and  $1.2\lambda_0$ , which is similar to the observations of axial mode helical antennas [1]. High directivity may also be achieved for helical antennas of small circumference,  $C_h = 0.4\lambda_0$ , when the spacing between turns is large, i.e. in the order of  $S \approx 0.4\lambda_0$ .

It is seen that high directivity may be achieved for very different combinations of  $S$  and  $C_h$ , however, the F/B ratio is not necessarily high as seen from Fig. 6b. This is exemplified by the configuration  $C_h = 0.58\lambda_0$  and  $S = 0.28\lambda_0$  where

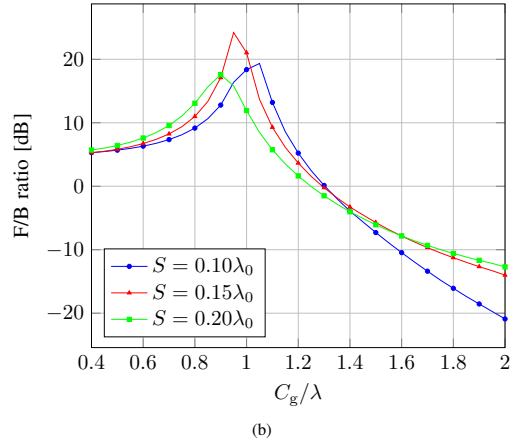
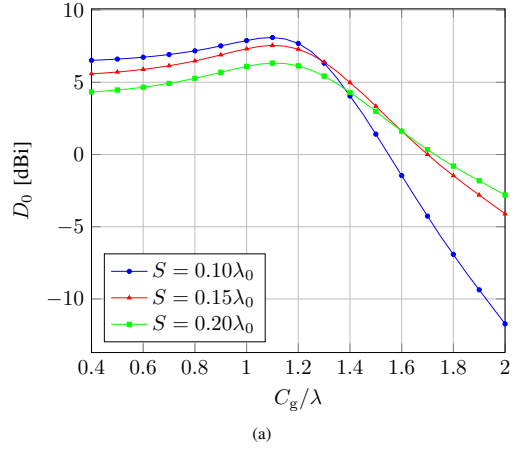


Fig. 5. (a) directivity and (b) F/B ratio of three backfire helical antenna configurations for  $C_h = 1.0\lambda_0$ .

maximum directivity of 9.9 dBi is achieved. For this antenna, the F/B ratio is 4.4 dB which may be unacceptable in many cases.

A maximum F/B ratio of 24.7 dB is achieved for the antenna configuration  $S = 0.14\lambda_0$  and  $C_h = 0.96\lambda_0$ , in which case the directivity is 7.6 dBi. Observing the constant  $S/C_h$  curves and the F/B ratio contour in Fig. 6b, it is found that the backfire helical antenna can be operated with an F/B ratio better than 10 dB over a 37% bandwidth.

For each combination of  $C_h$  and  $S$ , the current distribution on the conductor has been evaluated and  $p$  has been calculated, both using the simulated phase results, i.e. (3), and the theoretical expression in (2b) for  $\theta = 0^\circ$ .  $p$  from (3) has been calculated over  $0 \leq l' \leq 0.5$  which contains the decaying current amplitude region only for most backfire configurations. The white solid contour curve in Fig. 6b indicates the  $p = 1$  level by (3); in the area to the right of this curve  $p > 1$ .

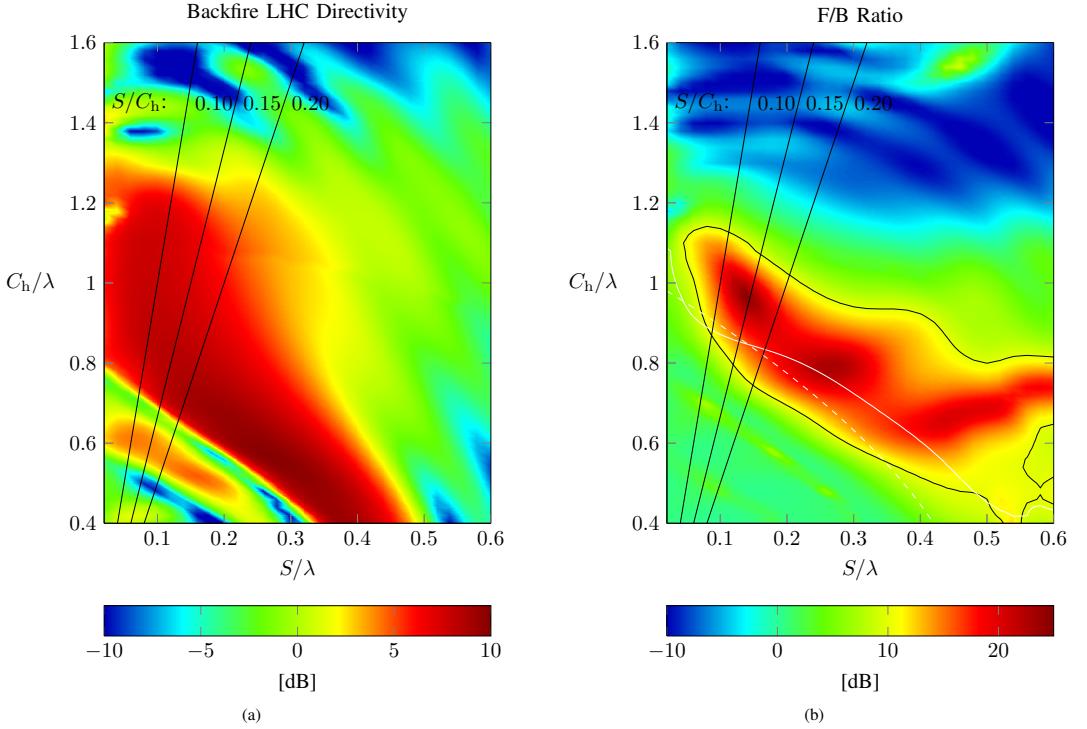


Fig. 6. Influence of the helical geometry on the (a) backfire LHC directivity and (b) F/B ratio for  $C_g = C_h$ . Moving along the constant  $S/C_h$ -lines corresponds to a frequency sweep for a fixed geometrical configuration. In (b), the 10 dB F/B ratio contour and  $p = 1$  contour are shown in solid black and white, respectively, and the theoretical in-phase condition of (2b) for backfire radiation for  $p = 1$  is shown in dashed white.

One should remember that  $p > 1$  is not a sufficient nor necessary criterion for backfire radiation, e.g. for  $C_h = 0.78\lambda$  and  $S = 0.16\lambda$  the in-phase condition (2b) yields  $p = 0.95$  for  $\theta = 0^\circ$ . The theoretical results from (2b) is shown by a white dashed line. It is seen that the theoretical curve of (2b) is close to, but does not coincide with, the contour of  $p = 1$  of the simulated currents. The deviation emphasizes that the array model of the helical antenna is a crude, and for some configurations inaccurate, way of modelling the antenna.

#### IV. CONCLUSIONS

The backfire monofilar helical antenna has been investigated. The characteristics of the current distribution on the helical conductor have been described, and the axial and backfire radiating mode of the helical antenna have been investigated by the phase velocities of the currents propagating along the conductor. The input impedance of the backfire helical antenna exhibits a wideband operation similar to the axial mode antenna, and 15 dB impedance bandwidths up to 64% have been demonstrated. An F/B ratio above 10 dB can be obtained over a 37% bandwidth.

It has been found that maximum directivity and F/B ratio

can be achieved for the backfire helical antenna when the diameters of the ground plane and helix are equal. Lastly, a parametric study of the geometrical helix parameters has been presented, from which optimal dimensions of the backfire helical antenna can be chosen for maximum directivity or F/B ratio.

#### REFERENCES

- [1] J. D. Kraus, *Antennas*, 2nd ed. McGraw-Hill, 1988.
- [2] W. L. Stutzman and G. A. Thiele, *Antenna Theory and Design*, 2nd ed. Wiley, 1997.
- [3] M. Roy, "Constructing normal-mode helical antennas," *IEE-IERE Proceedings - India*, vol. 7, pp. 119–123, 1969.
- [4] H. Nakano and J. Yamauchi, "Characteristics of modified spiral and helical antennas," *IEE Proceedings H, Microwaves, Optics and Antennas*, vol. 129, pp. 232–237, 1982.
- [5] H. Nakano, J. Yamauchi, and H. Mimaki, "Backfire radiation from a monofilar helix with a small ground plane," *IEEE Trans. Antennas Propagat.*, vol. 36, pp. 1359–1364, Oct. 1988.
- [6] A. R. Djordjevic, M. B. Bazdar, V. V. Petrovic, D. I. Olcan, T. K. Sarkar, and R. F. Harrington, *AWAS for Windows, Version 2.0, Analysis of Wire Antennas and Scatterers, Software and User Manual*. Artech House, 2002.



## CONFERENCE PAPER II

---

# 20/30 GHz DUAL-BAND CIRCULARLY POLARIZED REFLECTARRAY ANTENNA BASED ON THE CONCENTRIC DUAL SPLIT-LOOP ELEMENT

Thomas Smith, Niels Larsen, Ulrich Gothelf,  
Oleksiy S. Kim, and Olav Breinbjerg

*Status*

Presented: October 2012

### **Bibliography**

- [C2] T. Smith, N. Larsen, U. Gothelf, O. S. Kim, and O. Breinbjerg, “20/30 GHz Dual-Band Circularly Polarized Reflectarray Antenna based on the Concentric Dual Split-Loop Element,” *Proc. 34th ESA Antenna Workshop*, 2012.





# 20/30 GHz DUAL-BAND CIRCULARLY POLARIZED REFLECTARRAY ANTENNA BASED ON THE CONCENTRIC DUAL SPLIT-LOOP ELEMENT

Thomas Gunst Smith<sup>1,2</sup>, Niels Vesterdal Larsen<sup>1</sup>, Ulrich Vesterager Gothelf<sup>1</sup>, Oleksiy S. Kim<sup>2</sup>, and Olav Breinbjerg<sup>2</sup>

<sup>1</sup>Thrane & Thrane A/S, Lundtoftegårdsvej 93D, DK-2800 Kgs. Lyngby, Denmark

<sup>2</sup>Department of Electrical Engineering, Electromagnetic Systems, Technical University of Denmark, Ørstedes Plads, Building 348, DK-2800 Kgs. Lyngby, Denmark

## ABSTRACT

A concentric dual split-loop element is designed and investigated for reflectarray antenna design in the emerging 20 GHz and 30 GHz Ka-band satellite communication spectrum. The element is capable of providing adjustment of the phase of reflection coefficients for circular plane waves in two separate frequency bands, by rotation of the individual split-loops. Cross-polar reflection is simultaneously minimized by optimizing the gaps in the split-loops. Based on the element characteristics, an iterative design procedure is proposed and used to design a front-fed reflectarray antenna. The aperture efficiency exceeds 56 % with an on-axis axial ratio below 0.21 dB in both frequency bands.

## 1. INTRODUCTION

A reflectarray antenna generally consists of an array of scattering elements and a feeding antenna. The operating principle is derived from classical reflector antennas, where a shaped surface can be designed to produce e.g. a pencil or contoured beam. However, for planar reflectarrays, the scattering elements are designed to reflect the incident field with a desired phase, such that a given far-field can be achieved [1].

For high-gain antennas, printed reflectarrays are of particular interest due to their low cost, ease of manufacture and reconfigurability [2]. Thus a printed reflectarray is a feasible candidate for user terminal antennas for satellite communication in the emerging Ka-band spectrum. When choosing the reflectarray element topology, the requirements to polarization and bandwidth are essential. For circular polarization, commonly used elements include stub-tuned patches [3], crossed dipoles [4, 5] and single split-loops [6, 7]. However, for large reflectarrays the differential spatial phase delay is signifi-

cant [8] making it extremely challenging to cover the entire 20 – 30 GHz frequency band, thus it is preferred to utilize a reflectarray element which allows separate phase adjustment in the 20 and 30 GHz frequency bands. For this purpose, a concentric dual split-loop element utilizing the element rotation technique is proposed. The element is investigated and optimized for dual-frequency circular polarization, specifically LHCP from 19.7 to 20.2 GHz (RX) and RHCP from 29.5 to 30.0 GHz (TX). This element was suggested in [1, p. 122], but to the best of our knowledge it has not been subject to detailed investigations.

## 2. ELEMENT DESIGN AND INVESTIGATION

The commercially available software Ansoft Designer has been employed to optimize the element geometry. By using periodic boundary conditions and plane wave excitation the element is simulated as if it was located in a two dimensional infinite square grid array, with an inter-element spacing of 5 mm. The element has shown stable performance over relevant incidence angles; hence only normal incidence is considered in this paper.

### 2.1. Element Rotation Technique

A local  $(u, v)$  coordinate system is assigned to the element under consideration, which in Figure 1 is exemplified by a simple dipole though the following is valid for arbitrary element geometries. The rotation of the local coordinate system, and thus the element, can be described in the global  $(x, y)$  coordinate system by the rotation angle  $\psi$ .

An incident RHCP plane wave is considered traveling in the negative  $z$ -direction  $\mathbf{E}^i = (\hat{x} + j\hat{y}) E_0 e^{jkz}$ , where  $E_0$  is the electric field amplitude and  $k$  is the free-space

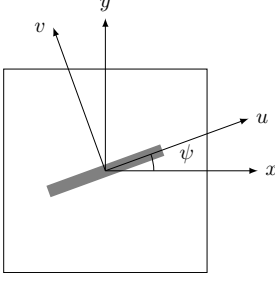


Figure 1. Global  $(x, y)$  and local  $(u, v)$  coordinate system for element rotation.

wavenumber. The time-factor  $e^{j\omega t}$  is assumed and suppressed. By decomposing this incident field along the  $u$ - and  $v$ -directions and employing the associated linear reflection coefficients,  $R_u$  and  $R_v$ , it can readily be shown that the reflected far-field plane wave can be described by

$$\mathbf{E}^s = \frac{1}{2} \left( (R_u - R_v) [\hat{x} - j\hat{y}] e^{j2\psi} + (R_u + R_v) (\hat{x} + j\hat{y}) \right) E_0 e^{-jkz}, \quad (1)$$

where  $R_u, R_v$  are the reflection coefficients of the linear electric field components along  $\hat{u}, \hat{v}$ , respectively. It is evident that for  $R_u = R_v e^{j\pi}$ , the scattered field is a pure RHCP plane wave traveling in the positive  $z$  direction and the phase scales linearly in  $\psi$ . However, if either  $|R_u| \neq |R_v|$ , or if the phase difference is not equal to  $\pi$ , cross-polarization (here LHCP) is introduced.

It is important to note that for elements placed in a reflectarray element grid, the coupling to the neighboring elements will generally change when the element is rotated. It is therefore crucial to modify the element geometry accordingly to keep  $R_u = R_v e^{j\pi}$ , such that the cross-polar reflection is suppressed [7]. This is usually achieved by an anisotropic design where only one of the two linear orthogonal polarizations excites a resonant element, e.g. a dipole on a grounded dielectric, as depicted in Figure 1. In the case of resonance, the polarization parallel to the dipole will see a reflection with zero phase, whereas the orthogonal polarization will be reflected with a phase equal to  $\pi$  due to the infinite ground-plane. Therefore, if the dipole length is adjusted properly, a phase-difference of  $\pi$  is ensured. However, since the losses increase significantly around the resonance, the amplitude of the parallel component will be smaller than the orthogonal. It is thus clear that the losses put a constraint on the cross-polarization level that can be achieved.

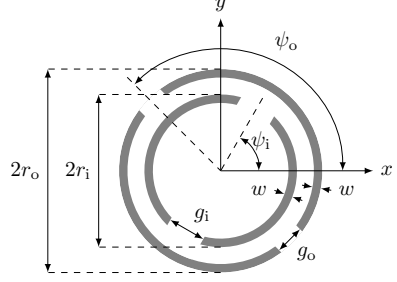


Figure 2. Concentric dual split-loop reflectarray element geometry.

## 2.2. Concentric Dual Split-Loop Element

The concentric dual split-loop element proposed in this paper is illustrated in Figure 2. The outer and inner split-loop is characterized by the radii  $r_o$  and  $r_i$ , respectively, measured from the center to the outside of the conductor, the rotation angles  $\psi_o$  and  $\psi_i$ , the gap sizes  $g_o$  and  $g_i$ , and equal conductor width  $w$ . The element is printed on a grounded Rogers RT/Duroid 5880 substrate with dielectric constant  $\epsilon_r = 2.20$ , dissipation factor  $\tan \delta = 0.0009$  and thickness of 1.016 mm.

The concept of the concentric dual split-loop element is that the inner and outer split-loop can be rotated such that desired reflection phases are obtained at 20 and 30 GHz simultaneously. As noted in Section 2.1, the geometry of the concentric dual split-loop element must be adjusted such that the orthogonal reflection coefficients have a phase difference of  $\pi$ , so that no cross-polarization occurs. However, when the outer and inner split-loops are rotated their coupling to each other and to neighboring elements change. Therefore, by adjusting the gaps of the split-loops,  $g_o$  and  $g_i$ , each element is optimized to minimize cross-polar reflection, for all rotation angles. In this way, the cross-polar reflection coefficient at both 20 and 30 GHz is suppressed below  $-31$  dB for all rotation angles. The optimized element geometry is given in Table 1. Due to the symmetry of the concentric dual split-loop element, all properties are  $180^\circ$  periodic in rotation, hence results are shown for  $\psi_o$  and  $\psi_i$  in the interval  $0^\circ$  to  $180^\circ$ .

Table 1. Reflectarray element geometry data.

$r_o$	1.9 mm
$r_i$	1.4 mm
$w$	0.2 mm
$\psi_o, \psi_i$	$[0^\circ; 180^\circ]$
$g_o$	[0.46 mm; 0.52 mm]
$g_i$	[0.24 mm; 1.01 mm]

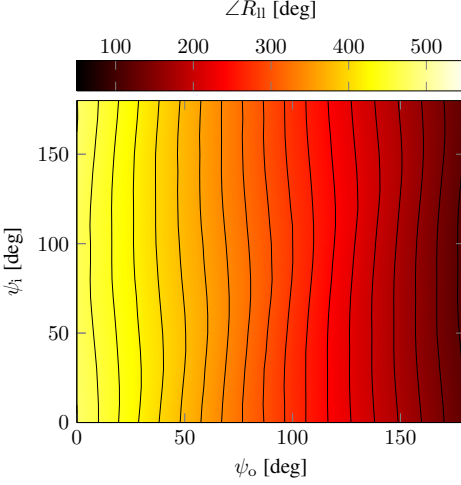


Figure 3. Phase of 20 GHz LHCP-to-LHCP reflection coefficient.

At 20 GHz, the reflection coefficient is primarily determined by  $\psi_o$  and almost unaffected by  $\psi_i$ , which can be seen in Figure 3, where  $\angle R_{ll}$  is the phase of the LHCP-to-LHCP circular reflection coefficient. The contour curves are almost vertical and equidistant, indicating that the rotation of the outer split-loop provides the desired linear phase adjustment over rotation angle  $\psi_o$  for any value of  $\psi_i$ . For a fixed value of  $\psi_o$ , the phase varies within  $\pm 5.0^\circ$  when  $\psi_i$  is varied.

At 30 GHz, the reflection coefficients are found to depend on both  $\psi_o$  and  $\psi_i$ , which is evident in Figure 4, where  $\angle R_{rr}$  is the phase of the RHCP-to-RHCP reflection coefficient. However, an important feature is that for a fixed value of  $\psi_o$ , the phase is monotonic in  $\psi_i$ , which means that for a given rotation angle of the outer split-loop, there is a unique solution for the rotation angle of the inner split-loop which gives a desired reflection phase.

The phase range of the circular co-polar reflection coefficient is exactly  $360^\circ$ , for  $\psi_o$  or  $\psi_i$  in the interval  $0^\circ$  to  $180^\circ$ , at 20 and 30 GHz, respectively. This range is of course necessary for the use of the element in the reflectarray design. For all rotation angles of both the inner and outer split-loops, the amplitude of the co-polar reflection coefficient is above 0.26 and 0.35 dB over the entire RX and TX frequency bands, respectively.

The above mentioned characteristics of the circular reflection coefficients enables a design of a reflectarray antenna, where the reflectarray is first optimized for 20 GHz performance by determining  $\psi_o$  for all ele-

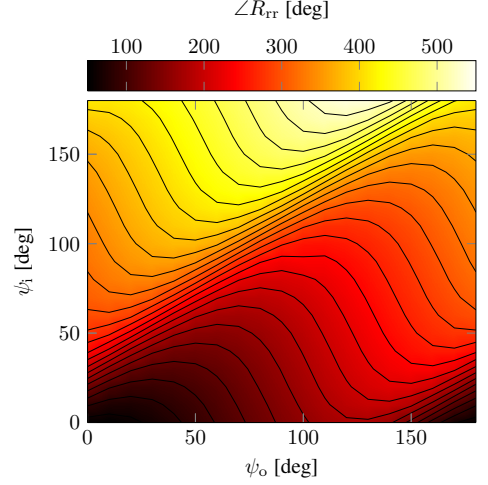


Figure 4. Phase of 30 GHz RHCP-to-RHCP reflection coefficient.

ments, and afterwards adjusting  $\psi_i$  for 30 GHz performance without affecting the radiation at 20 GHz significantly.

### 3. REFLECTARRAY DESIGN

Based on the element characteristics presented in Section 2, an iterative design procedure has been developed to determine  $\psi_o$  and  $\psi_i$  for each reflectarray element. In this section, the proposed design procedure is described and a concept reflectarray antenna design is presented.

#### 3.1. Design Procedure

As stated in Section 2, the reflection coefficient at 20 GHz is almost unaffected by rotation of the inner split-loop, hence the reflectarray may be optimized for 20 GHz and subsequently 30 GHz. The reflectarray is designed for a single frequency in each of the two separate frequency bands, and the design procedure can generally be outlined as follows:

1.  $g_o$  and  $g_i$  are optimized for minimum cross-polar reflection using Ansoft Designer, for a finite set of  $\psi_o$  and  $\psi_i$
2.  $\psi_o$  and  $\psi_i$  of all reflectarray elements are set to zero
3.  $\psi_o$  is determined for all reflectarray elements
  - (a) A one dimensional 20 GHz phase-curve is generated for varying  $\psi_o$ , while keeping  $\psi_i$  fixed

- (b)  $\psi_o$  is determined from the phase-curve and the desired reflected phase
4.  $\psi_i$  is determined for all reflectarray elements
  - (a) A one dimensional 30 GHz phase-curve is generated for varying  $\psi_i$ , while keeping  $\psi_o$  fixed
  - (b)  $\psi_i$  is determined from the phase-curve and the desired reflected phase
5. The scattered aperture field over the reflectarray is calculated
6. The radiated field of the entire reflectarray is calculated and the feed pattern is added

Step 3 and step 4 can be repeated such that the actual non-zero rotation angle of  $\psi_i$  is included when choosing  $\psi_o$ . This may be necessary for concentric dual split-loop geometries where the coupling between the two loops is larger at 20 GHz. However, for the present design a single iteration is sufficient.

The procedure has been implemented in a numerical code that calculates the radiated far-field by the equivalent currents technique [9, technique II].

### 3.2. Concept Design

To validate the proposed reflectarray element, a front-fed circular aperture reflectarray has been designed. The reflectarray is designed to have a broadside pencil beam towards  $\theta = 0^\circ$  and consists of approximately 11,300 elements. The developed code allows for an arbitrary feed antenna, but here a Gaussian beam feed model is used. The specifications of the reflectarray and feed antenna are summarized in Table 2.

The rotation angles of the concentric dual split-loop elements are shown in Figure 5. Due to the rotational symmetry of the reflectarray only a cross-section from the center to the edge is shown, where element 61 and 120 are the element near the center and edge, respectively. It is found that the rotation angle of the outer split-loop scales linearly with the distance from the element to the feed antenna, which is due to the linear  $2\psi_o$  reflection phase behavior and independence of  $\psi_i$ , as discussed in Section 2. However, the rotation angle of the inner split-loop is highly aperiodic. This is caused by the complex behavior of the reflection phase, as also discussed in Section 2.

Table 2. Specifications of front-fed reflectarray antenna.

RX	19.7 GHz – 20.2 GHz LHCP
TX	29.5 GHz – 30.0 GHz RHCP
Diameter	60 cm
Focal length	46 cm
Edge taper	–12 dB

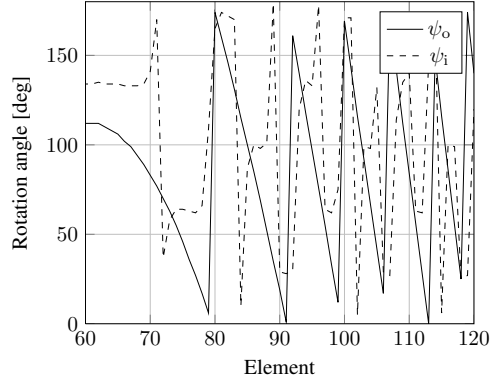


Figure 5. Rotation angles of reflectarray elements along radial cut from centre to edge of the circular aperture.

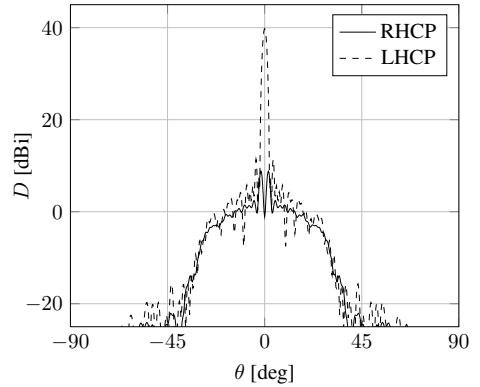


Figure 6. Radiation pattern of the designed reflectarray at 20 GHz.

The radiation pattern of the front-fed reflectarray is depicted in Figure 6 for 20 GHz and in Figure 7 for 30 GHz, with a zoom of the 30 GHz radiation pattern in Figure 8. At 20.0 GHz, the maximum directivity is 39.8 dBi, which corresponds to an aperture efficiency of 60 %, and the sidelobe level is 28.4 dB below peak. At 30.0 GHz, the maximum directivity is 43.2 dBi, which is an aperture efficiency of 58 %, and the sidelobe level is 30.4 dB below peak.

Over the RX and TX frequency bands, the on-axis copolar directivity and axial ratio (AR) is plotted in Figure 9 and 10, respectively. The designed reflectarray antenna has an aperture efficiency exceeding 56 % and an on-axis AR below 0.21 dB over both the RX and TX frequency bands.

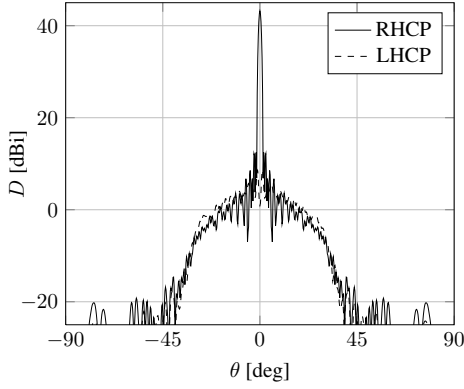


Figure 7. Radiation pattern of the designed reflectarray at 30 GHz.

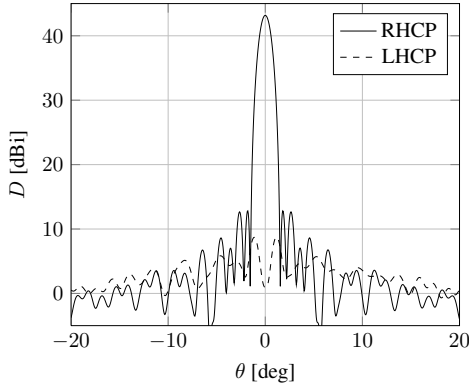


Figure 8. Zoom of the radiation pattern of the designed reflectarray at 30 GHz.

#### 4. CONCLUSIONS

A concentric dual split-loop reflectarray element for dual-band circular polarization has been presented. The element provides means for adjusting the phase of circular reflection coefficients in two separate frequency bands. By optimizing the element geometry, the cross-polar reflection coefficient of the element has been suppressed below  $-31$  dB for all element rotation angles, at both design frequencies simultaneously.

An iterative design-procedure has been presented, and a front-fed reflectarray antenna has been designed for dual-band 20 and 30 GHz application. The reflectarray shows satisfying performance in both frequency bands, with an aperture efficiency above 56 % and on-axis AR below 0.21 dB.

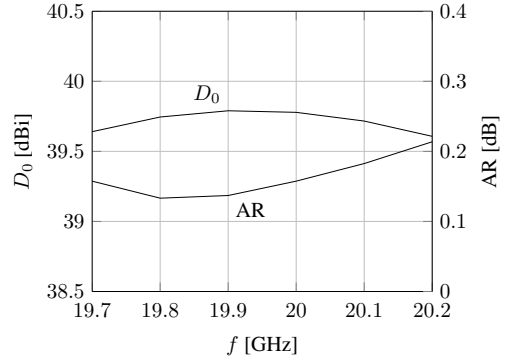


Figure 9. On-axis directivity and AR in RX frequency band.

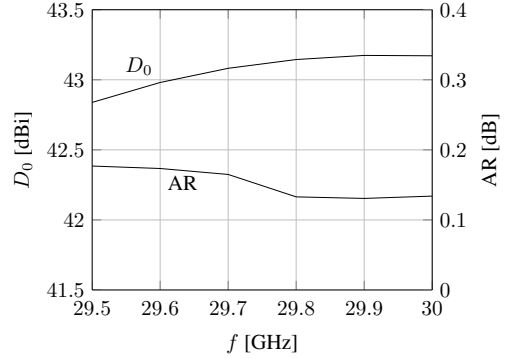


Figure 10. On-axis directivity and AR in TX frequency band.

A prototype reflectarray is planned to be manufactured and measured in the near future to validate the presented results.

#### REFERENCES

- [1] J. Huang and J. A. Encinar. *Reflectarray Antennas*. IEEE Press, 2008.
- [2] J. A. Encinar. Recent advances in reflectarray antennas. In *Proceedings of the European Conference on Antennas and Propagation*, pages 1–6, 2010.
- [3] J. Huang and R. J. Pogorzelski. A Ka-band microstrip reflectarray with elements having variable rotation angles. *IEEE Transactions on Antennas and Propagation*, 46(5):650–656, 1998.
- [4] E. B. Felstead, J. Shaker, M. R. Chaharmir, and A. Petosa. Enhancing multiple-aperture ka-band

- navy SATCOM antennas with electronic tracking and reflectarrays. In *MILCOM 2002. Proceedings*, volume 2002 of 1, pages 168–172. IEEE, October 2002.
- [5] R. Chaharmir, J. Shaker, and M. Cuhaci. Development of dual-band circularly polarised reflectarray. In *IEE Proceedings - Microwaves, Antennas and Propagation*, volume 153, pages 49–54, 2006.
  - [6] B. Strassner, C. Han, and K. Chang. Circularly polarized reflectarray with microstrip ring elements having variable rotation angles. *IEEE Transactions on Antennas and Propagation*, 52(4):1122–1125, April 2004.
  - [7] A. Yu, F. Yang, A. Z. Elsherbeni, J. Huang, and Y. Kim. An offset-fed x-band reflectarray antenna using a modified element rotation technique. *IEEE Transactions on Antennas and Propagation*, 60(3):1619–1624, March 2012.
  - [8] D. M. Pozar. Bandwidth of reflectarrays. *Electronics Letters*, 39(21):1490–1491, 2003.
  - [9] M. Zhou, S. B. Sorensen, E. Jorgensen, P. Meincke, O. S. Kim, and O. Breinbjerg. An accurate technique for calculation of radiation from printed reflectarrays. *IEEE Antennas and Wireless Propagation Letters*, 10:1081–1084, 2011.

## CONFERENCE PAPER III

---

# 20/30 GHz DUAL-BAND CIRCULARLY POLARIZED REFLECTARRAY ANTENNA BASED ON THE CONCENTRIC DUAL SPLIT-LOOP ELEMENT

Thomas Smith, Niels Larsen, Ulrich Gothelf,  
Oleksiy S. Kim, and Olav Breinbjerg

*Status*

Presented: April 2013

### **Bibliography**

- [C3] T. Smith, N. Larsen, U. Gothelf, O. S. Kim, and O. Breinbjerg, “20/30 GHz Dual-Band Circularly Polarized Reflectarray Antenna based on the Concentric Dual Split-Loop Element,” *Proc. EuCAP*, 2013.





# An Offset-Fed 20/30 GHz Dual-Band Circularly Polarized Reflectarray Antenna

Thomas Gunst Smith\*, Niels Vesterdal\*, Ulrich Gothelf\*,  
Oleksiy S. Kim†, and Olav Breinbjerg†

\*Thrane & Thrane A/S, Lundtoftegårdsvej 93D, DK-2800 Kgs. Lyngby, Denmark.

†Department of Electrical Engineering, Electromagnetic Systems, Technical University of Denmark, Ørstedes Plads, Building 348, DK-2800 Kgs. Lyngby, Denmark.

**Abstract**—A dual-frequency circularly polarized offset reflectarray antenna for Ka-band satellite communication is presented. The reflectarray is designed using the concentric dual split-loop element which enables full  $360^\circ$  phase adjustment simultaneously in two separate frequency bands. The elements have been optimized to suppress the cross-polar reflection. Thereafter, the element data is used for synthesis of the reflectarray layout and computation of the associated radiation patterns. The reflectarray is  $400\text{ mm} \times 400\text{ mm}$  and radiates LHCP at 19.95 GHz and RHCP at 29.75 GHz. Aperture efficiencies of 58% and 60% are obtained at these frequencies, and the cross-polarization is more than 25 dB below peak gain.

**Index Terms**—reflectarray antenna; reflectarray element; dual-band; circularly polarized; concentric dual split-loop

## I. INTRODUCTION

Printed reflectarray antennas present a viable alternative to reflector antennas, due to their compact size and low cost [1]. However, their planar nature implies a narrow bandwidth which is limited due to the differential spatial phase delay and the element bandwidth [2]. The differential spatial phase delay can be mitigated by using a non-planar multifacet reflectarray, or by optimizing the element phase shift at multiple frequencies [3], [4]. The first case allows the use of regular reflectarray elements such as patches or loops, however, the low profile layout of the antenna is lost and the manufacturing complexity increases. In the second case, the compactness and ease of manufacture is kept but this necessitates the use of advanced reflectarray elements.

In this paper an offset reflectarray antenna for the emerging Ka-band satellite communication services is presented. The reflectarray utilizes the concentric dual split-loop element [5], where the reflection phase is adjusted by the variable rotation technique (VRT) [6]. The reflectarray is fed by a dual-band corrugated horn antenna. The reflectarray is designed to radiate a left-hand circularly polarized (LHCP) pencil beam from 19.7 to 20.2 GHz, and a right-hand circularly polarized (RHCP) pencil beam from 29.5 to 30.0 GHz, in the specular direction.

The time factor  $e^{j\omega t}$  is assumed and suppressed throughout this paper.

## II. CONCENTRIC DUAL SPLIT-LOOP ELEMENT

The reflectarray is designed using the concentric dual split-loop element depicted in Fig. 1, that is printed on a 0.787 mm

Duroid 5880 substrate with  $\epsilon_r = 2.2$  and  $\tan \delta = 0.0009$ , with solid copper on the back side. The commercial software Ansoft Designer is used for the element analysis. Periodic boundary conditions are employed to simulate each element as the unit cell of a two dimensional infinite array. The array grid is uniform and square, and the inter-element spacing is 5 mm.

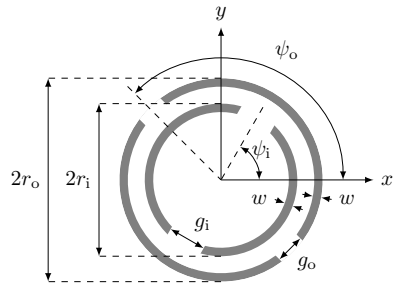


Fig. 1. Geometry of the concentric dual split-loop element; see dimensions in Table I.

The element consists of two concentric split-loops, each characterized by their respective radii  $r_o$  and  $r_i$ , gap widths  $g_o$  and  $g_i$ , rotation angles  $\psi_o$  and  $\psi_i$  and equal conductor widths  $w$ . The dimensions are specified in Table I. By adjusting the gaps of the split-loops,  $g_o$  and  $g_i$ , the element can be tuned such that the incident circularly polarized wave is reflected with the same sense of polarization, i.e. RHCP to RHCP, and LHCP to LHCP. By varying both  $\psi_o$  and  $\psi_i$ , the phase of the reflected circularly polarized waves can be adjusted by the VRT at the band center of frequencies 19.95 and 29.75 GHz, simultaneously. However, for each set of  $\psi_o$  and  $\psi_i$ ,  $g_o$  and  $g_i$  must be optimized to minimize the cross-polar reflection

TABLE I  
REFLECTARRAY ELEMENT GEOMETRY DATA.

$r_o$	2.05 mm
$r_i$	1.40 mm
$w$	0.2 mm
Square array grid	5 mm $\times$ 5 mm

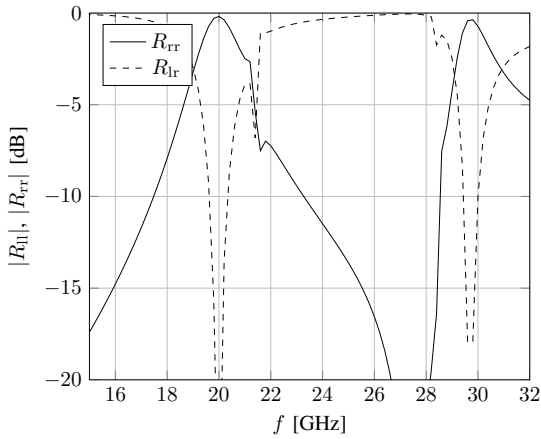


Fig. 2. Frequency sweep of circular reflection coefficients, for  $\psi_o = 0^\circ$  and  $\psi_i = 0^\circ$  at  $\phi^i = 0^\circ$ ,  $\theta^i = 30^\circ$  incidence angle.

(RHCP to LHCP, and vice versa).

For the case  $\psi_o = 0^\circ$  and  $\psi_i = 0^\circ$ , the amplitude of the RHCP to RHCP reflection ( $R_{rr}$ ) and RHCP to LHCP reflection ( $R_{lr}$ ) are depicted in Fig. 2, for  $\phi^i = 0^\circ$ ,  $\theta^i = 30^\circ$  incidence angle, which is the incidence angle at the center of the reflectarray. For these rotation angles  $|R_{||}| = |R_{rr}|$  and  $|R_{\perp}| = |R_{lr}|$ . It is seen that  $R_{lr}$  is indeed minimized at the design frequencies 19.95 and 29.75 GHz.

In Fig. 3,  $|R_{||}|$  is depicted at 19.95 GHz for varying  $\psi_o$  while keeping  $\psi_i = 0^\circ$ , and  $|R_{rr}|$  at 29.75 GHz for varying  $\psi_i$  while keeping  $\psi_o = 0^\circ$ . At 19.95 GHz,  $|R_{||}|$  is in the range from  $-0.19$  to  $-0.16$  dB owing to dielectric and conductor losses. These losses are dominant for the linear field component that is parallel to the axis of the outer gaps. Negligible currents are excited on the inner split-loop at 19.95 GHz, hence the reflection becomes invariant of  $\psi_i$ . This means that one linear component of the circularly polarized field will exhibit these losses independently of rotation angle, and this will introduce a constant level of cross-polarization regardless of  $\psi_i$ . The cross-polar level has been minimized to approximately  $-35$  dB.

At 29.75 GHz,  $|R_{rr}|$  is in the range from  $-0.35$  to  $-0.12$  dB. The oscillating behavior is caused by currents being excited on both the inner and outer split-loop. Thus, when the gaps are aligned, e.g.  $\psi_o = \psi_i = 0^\circ$ , the linear field component parallel to the axis of the gaps exhibits more loss than the transverse, which also de-polarizes the field. However, when the axes of the inner and outer gap are orthogonal, both orthogonal linear field components exhibit loss, and this de-polarizes the field to a lesser extent. Generally, the cross-polar  $|R_{lr}|$  is below  $-20$  dB for all rotation angles.

In Fig. 4, phase curves are shown at 19.95 for varying  $\psi_o$  while keeping  $\psi_i = 0^\circ$ , and at 29.75 GHz for varying  $\psi_i$  while

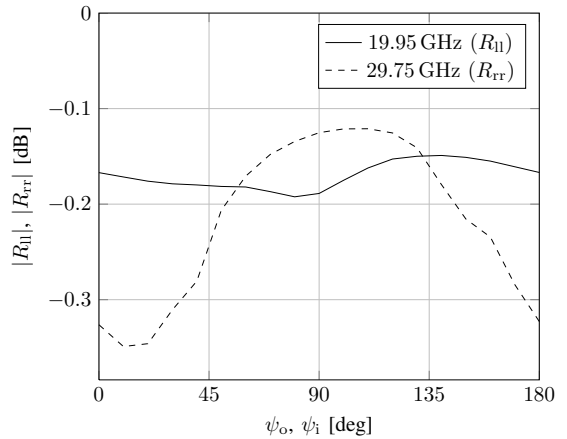


Fig. 3. Amplitude of the co-polar circular reflection coefficients at 19.95 ( $R_{||}$ ) for varying  $\psi_o$  for  $\psi_i = 0^\circ$ , and at 29.75 GHz ( $R_{rr}$ ) for varying  $\psi_i$  for  $\psi_o = 0^\circ$ .

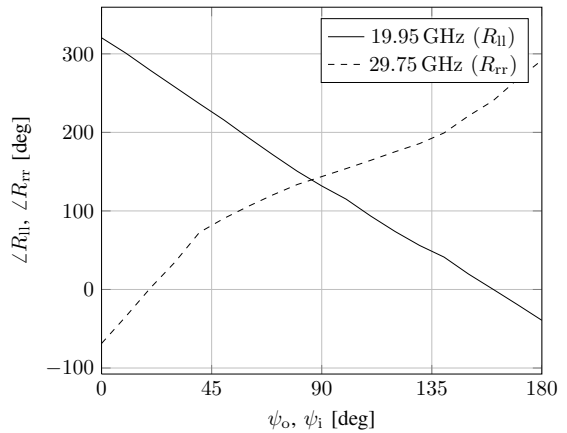


Fig. 4. Phase of the co-polar circular reflection coefficients at 19.95 ( $R_{||}$ ) for varying  $\psi_o$  for  $\psi_i = 0^\circ$ , and at 29.75 GHz ( $R_{rr}$ ) for varying  $\psi_i$  for  $\psi_o = 0^\circ$ .

keeping  $\psi_o = 0^\circ$ . At 19.95 GHz, the phase is almost linear over the rotation angle  $\psi_o$ , as predicted by the VRT. It has been found that the reflection coefficients and thus phase curve are almost invariant of  $\psi_i$  at this frequency. However, the phase curve at 29.75 GHz is not linear and has also been found to depend on  $\psi_o$ .

The concentric dual split-loop element is optimized for rotation angles in steps of  $10^\circ$ , for plane wave incidence from  $\phi^i = 0^\circ$ ,  $\theta^i = 30^\circ$ . The found geometries are subsequently simulated for plane wave incidence for  $\phi^i \in [0^\circ; 360^\circ]$  and

TABLE II  
OFFSET REFLECTARRAY ANTENNA DATA.

RX frequencies	19.7 GHz – 20.2 GHz LHCP
TX frequencies	29.5 GHz – 30.0 GHz RHCP
Reflectarray dimensions	400 mm × 400 mm
Feed distance to center of array	300 mm
Feed offset angle	$\phi = 0^\circ, \theta = 30^\circ$
Direction of mainbeam	$\phi = 180^\circ, \theta = 30^\circ$

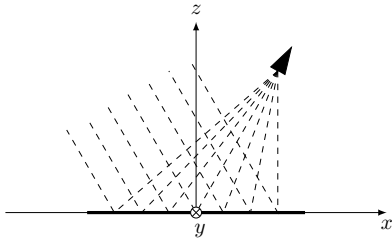


Fig. 5. Geometry of the offset reflectarray antenna with a pencil beam toward  $\phi = 180^\circ$  and  $\theta = 30^\circ$ .

$\theta^i \in [0^\circ; 60^\circ]$ . The calculated reflection coefficients form a lookup table that is used in the following reflectarray design.

Based on the observed characteristics of the concentric dual split-loop element a two-step reflectarray design procedure has been implemented. First, the outer split-loops are designed from the 19.95 GHz phase curve, and second, the inner split-loops are positioned from the 29.75 GHz phase curve, taking the actual rotation angle of the outer split-loop into account. To achieve the best possible design, however, the two-step procedure may be repeated, forming an iterative procedure described in [5].

The reader is referred to [5] for more details on the concentric dual split-loop element and the iterative design procedure.

### III. OFFSET REFLECTARRAY ANTENNA

Using the presented concentric dual split-loop element, an offset reflectarray antenna is designed and demonstrated, with the specifications given in Table II. The reflectarray is 400 mm by 400 mm (80 by 80 elements) and is fed by a feed antenna located at an offset angle  $\phi = 0^\circ, \theta = 30^\circ$ , 300 mm from the center of the reflectarray. The configuration is depicted in Fig. 5.

#### A. Feed Antenna

The feed antenna is a dual-band corrugated horn that radiates LHCP from 19.7 to 20.2 GHz and RHCP from 29.5 to 30.0 GHz. The horn is analyzed using BOR-MoM in the commercial software CHAMP by TICRA. Radiation patterns at the design frequencies 19.95 and 29.75 GHz are shown in Fig. 6 and 7 in a local feed coordinate system. The radiation pattern is rotationally symmetric. At 19.95 GHz, the maximum directivity is 15.7 dBi and the cross-polarization is 31.2 dB

below. At 29.75 GHz, the maximum directivity is 13.2 dBi and the cross-polarization is 22.9 dB below.

The feed antenna has not been optimized for this particular application, however, the focal length of the reflectarray has been chosen such that the illumination level along the edge of the reflectarray varies from approximately  $-20$  to  $-5$  dB relative to the maximum in the reflectarray aperture.

The actual feed has been measured at the DTU-ESA Spherical Near-Field Antenna Test Facility [7], which will be used in the reflectarray analysis for the comparison against reflectarray measurements.

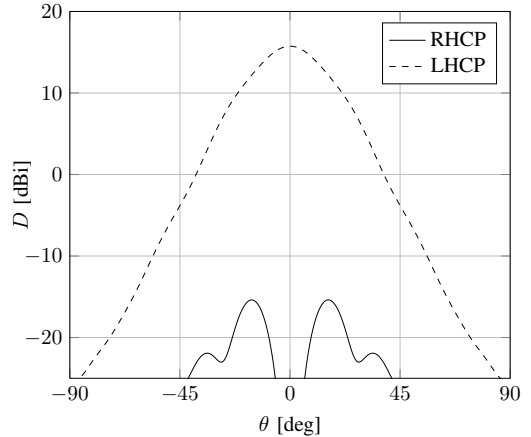


Fig. 6. Feed antenna directivity pattern at 19.95 GHz.

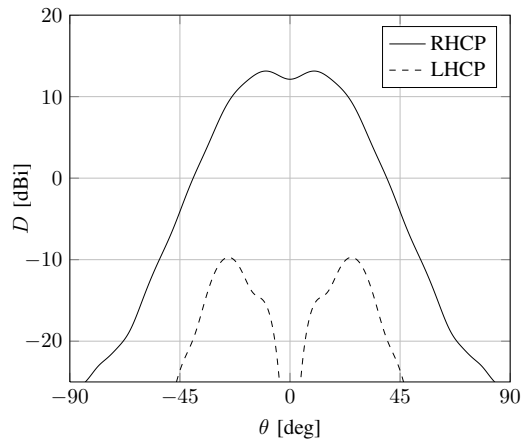


Fig. 7. Feed antenna directivity pattern at 29.75 GHz.

#### B. Reflectarray Design

To obtain a pencil beam toward  $\phi = 180^\circ, \theta = 30^\circ$ , the reflected field should have a planar phase front in this direction.

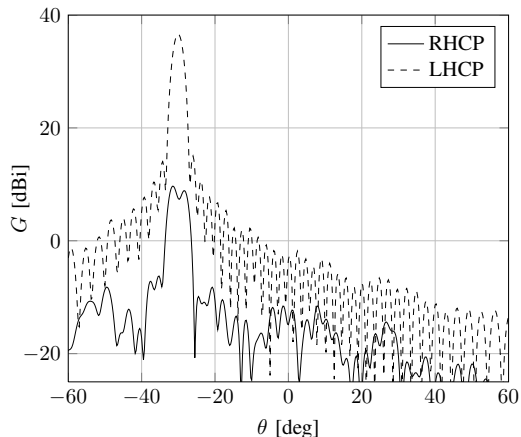


Fig. 8. Gain pattern of the designed reflectarray at 19.95 GHz in the  $\phi = 0^\circ$  cut.

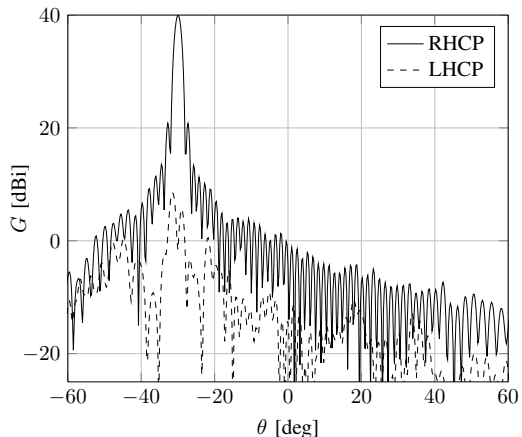


Fig. 9. Gain pattern of the designed reflectarray at 29.75 GHz in the  $\phi = 0^\circ$  cut.

This is achieved by adjusting the rotation angles  $\psi_o$  and  $\psi_i$  of each reflectarray element. Usually, the phase compensation is found by assuming a point source feed antenna, thus the phase compensation is equal to the electrical length from the feed to the particular element. In this design, the incident near-field of the dual-band corrugated horn antenna is calculated in the reflectarray aperture. From this field the correct phase compensation can be chosen, even for feed antennas with no phase center. The reflectarray is designed using the iterative design procedure described in the Section II, and the far-field radiation is calculated by the equivalent currents technique [8, technique II].

### C. Simulated Radiation Patterns

The simulated gain patterns of the offset reflectarray antenna are depicted in Fig. 8 and 9, at 19.95 and 29.75 GHz, respectively. At 19.95 GHz, the peak gain is 36.6 dBi and the maximum sidelobe and cross-polarization are 22.7 dB and 26.9 dB below that, respectively. At 29.75 GHz, the gain is 40.0 dBi and the maximum sidelobe gain and cross-polarization are 19.3 dB and 31.5 dB below that, respectively. The high cross-polarization level owes to the fact that the concentric dual split-loop elements have only been optimized for the single incidence angle ( $\phi^i = 0^\circ, \theta^i = 30^\circ$ ).

The maximum axial-ratio within the  $-1$  dB contour of the main-beam is 1.3 dB and 0.3 dB at 19.95 GHz and 29.75 GHz, respectively.

The reflectarray antenna is currently being manufactured and will be measured at the DTU-ESA Spherical Near-Field Antenna Test Facility. The measurement results and the antenna performance over the frequency bands of interest will be presented at the conference.

## IV. CONCLUSION

In this paper, a dual-band circularly polarized reflectarray antenna has been presented. The reflectarray utilizes the concentric dual split-loop element, which enables simultaneous phase adjustment in two separate frequency bands. An iterative design procedure has been used to optimize the reflectarray at 19.95 GHz, and subsequently at 29.75 GHz.

At the design frequencies, the peak gain is 36.6 and 40.0 dB, which corresponds to aperture efficiencies of 60% and 58%, respectively. The cross-polarization is more than 25 dB below peak gain, however, this may be suppressed further by optimizing the concentric dual split-loop element for multiple angles of incidence.

## REFERENCES

- [1] J. Huang and J. A. Encinar, *Reflectarray Antennas*. IEEE Press, 2008.
- [2] D. M. Pozar, "Bandwidth of reflectarrays," *Electronics Letters*, vol. 39, no. 21, pp. 1490–1491, 2003.
- [3] A. Roederer, "Reflector antenna comprising a plurality of panels," NL Patent US 6 411 255, 2002.
- [4] J. A. Encinar and J. A. Zornoza, "Broadband design of three-layer printed reflectarrays," *IEEE Transactions on Antennas and Propagation*, vol. 51, no. 7, pp. 1662 – 1664, Jul. 2003.
- [5] T. Smith, N. V. Larsen, U. V. Gothelf, O. S. Kim, and O. Breinbjerg, "20/30 ghz dual-band circularly polarized reflectarray antenna based on the concentric dual split-loop element," in *Proc. ESA Antenna Week*, 2012.
- [6] J. Huang and R. Pogorzelski, "A Ka-band microstrip reflectarray with elements having variable rotation angles," *IEEE Transactions on Antennas and Propagation*, vol. 46, no. 5, pp. 650–656, 1998.
- [7] [Online]. Available: [http://www.dtu.dk/centre/ems/English/research/dtu\\_esa\\_facility.aspx](http://www.dtu.dk/centre/ems/English/research/dtu_esa_facility.aspx)
- [8] M. Zhou, S. Sorensen, E. Jorgensen, P. Meincke, O. Kim, and O. Breinbjerg, "An accurate technique for calculation of radiation from printed reflectarrays," *IEEE Antennas and Wireless Propagation Letters*, vol. 10, pp. 1081 –1084, 2011.

# PATENT APPLICATION I

---

## COMBINED L-BAND (1-2 GHz) AND KA-BAND (20-30 GHz) ANTENNA

Thomas Smith, Johan Granholm,  
Oleksiy S. Kim, and Olav Breinbjerg

*Status*

Filed: January 2013

### **Bibliography**

- [P1] T. Smith, J. Granholm, O. S. Kim, and O. Breinbjerg, “Combined L-band (1-2 GHz) and Ka-band (20-30 GHz) Antenna,” *Patent Application PCT/EP2013/050259*, 2013.



## A DUAL ANTENNA

The present invention relates to a dual antenna and in particular to a dual-reflector antenna comprising a backfire helix using the sub-reflector as its reflector.

In recent years, the internet has become the keystone in modern communication systems.

- 5 Both land-based as well as many mobile users, e.g. maritime, demand easy, reliably and low-cost access to high-speed communications via the internet. For some applications, e.g. maritime, wireless data communications via e.g. satellite is the preferred method to provide the necessary bandwidth. As the data bandwidth requirements continue to grow, satellites therefore have to operate at yet higher frequencies, moving from e.g. nowadays typically
- 10 operating in L-band (the 1-2 GHz frequency range, there providing typically up to 0.5 Mbit/s data rate) range to operate in Ka-band (the 20-30 GHz frequency range, there capable of providing > 100 Mbit/s data rate). While L-band satellite communications is practically unaffected by the atmosphere effects (i.e. attenuation owing to rain, snow etc.), Ka-band satellite communications may exhibit a complete outage in the case of e.g. heavy rain. Thus,
- 15 there is a demand for integrated antennas capable of simultaneously operating in L- and Ka-band, for use in compact and low-cost, dual-band satellite communication systems, hence providing outage-free operation when combining the two systems.

- For dual-band high-performance antenna systems operating in widely spaced frequencies, such as L- and Ka-band, the same antenna cannot easily be used, but two antennas have to
- 20 be combined. A major challenge in the development of dual-band, high-performance antennas, which shall radiate in the same direction, is to select and integrate the two antennas to have minimum interaction or disturbance onto each other, while yet achieving sufficient performance in both bands. In e.g. a combined L-band/Ka-band antenna system, the Ka-band antenna may (easily) be degraded in gain and sidelobe performance by the
- 25 presence of the low frequency, L-band antenna. Since the high-frequency Ka-band antenna may often be implemented as e.g. a dual-reflector antenna (comprising a main reflector and a sub-reflector), a key issue is to find a suitable L-band antenna which may be integrated with the Ka-band antenna with minimum disturbance to the Ka-band antenna.

- Communication technologies may be seen in: US4608574, Richard C. Johnson and Rickey B. Cotton: "A Backfire Helical Feed", IEEE Trans Transactions on Antennas and Propagation, Vol. AP-32, No. 10, pp. 1126-1128, Oct. 1984, Hisamatsu Nakano, Junji Yamauchi and Hiroaki Mimaki: "Backfire Radiation from a Monofilar Helix with a Small Ground Plane", IEEE Transactions on Antennas and Propagation, Vol AP-36, No. 10, pp. 1359-1364, Oct. 1988, H. E. King and J. L. Wong: "240-400 MHz Antenna System for the Fleetsatcom Satellites", IEEE
- 30 AP-S, Antennas and Propagation Society International Symposium, 1977, June 21, pp. 349-
- 35



352, US7388559, JP2226804, JP63194403, US4742359, US3184747, WO9205681, A. Brunner: "Dual polarization coaxial corrugated horn feed with split focus subreflector", Proc. of 16th ESA Workshop on Dual Polarization Antennas, June 8-9, 1993, ESTEC, Noordwijk, The Netherlands, ESTEC publication no. WPP-051, pp. 205-208, DE4200755, DE9200357,  
 5 US5926146, US5835057, US7038632, US2003/0234745 and US2008/0120654.

In a first aspect, the invention relates to a dual antenna comprising:

- a main reflector,
- a sub-reflector,
- a helix,
- 10 - a feed antenna,

wherein:

- the feed antenna is positioned so as to receive radiation reflected by the sub-reflector and/or emit radiation toward the sub-reflector,
- the helix is adapted to emit radiation toward and/or receive radiation reflected off the  
 15 main reflector,

wherein the sub-reflector is positioned between the main reflector and the helix.

In this context, a dual antenna is an antenna having two or more feed antennas. Naturally, the two or more feed antennas may be of the same or different types and may emit or be configured to emit radiation within the same or different, such as non-overlapping,  
 20 wavelength intervals. Also, the two or more feed antennas may generally receive or be configured to receive radiation within the same or different, such as non-overlapping, wavelength intervals.

In the present context, the dual antenna has a main reflector and a sub-reflector. The main reflector usually is an element receiving radiation from a radiation emitter, such as a satellite  
 25 or antenna, or which outputs radiation toward a radiation receiver, such as a satellite or an antenna. In this context, the radiation emitter and/or receiver (antenna or satellite) will not be a part of the present antenna and will usually not be attached thereto.

Usually, the main reflector has the purpose of collecting, collimating, focussing and/or concentrating sufficient radiation and reflecting as much of this radiation as feasible toward another element, such as the sub-reflector, the helix or a satellite/antenna.

5 The main reflector may be a curved element, such as a parabolic reflector. Alternatively, the main reflector may be a radiation transmissive element, such as a lens, or the main reflector may be a plane element comprising thereon, e.g. a reflectarray performing the collimating/focussing/collecting/concentrating action on the radiation.

10 Naturally, situations may exist where the main reflector receives radiation from another, even larger element, which larger element then performs the main task of collecting and concentrating radiation.

In this context, a helix is a coiled conductor or conducting element. This element may have one or more conducting elements, such as a monofilar, bifilar, trifilar, quadrifilar coiled element.

15 The feed antenna may be configured to only be a radiation receiver or only be a radiation transmitter or both.

According to the invention, the feed antenna is positioned so as to receive radiation reflected by the sub-reflector and/or emit radiation toward the sub-reflector. The feed antenna can be, but not limited to, a horn or an open-ended waveguide.

20 Usually, the main reflector will have a larger cross sectional area, when viewed in a plane perpendicular to a direction between a centre of the main reflector and of the sub-reflector and/or when viewed in a plane perpendicular to a direction between a centre of the main reflector and a radiation emitter/receiver, such as a satellite, toward which the main reflector is aimed. The aim of the main reflector is defined by radiation emitted from the sub-reflector, reflected by the main reflector and impinging on a radiation receiver (e.g. satellite or  
25 antenna) or vice versa. Usually, the set-up (positioning and curvatures) of the sub-reflector and the main reflector is so that radiation from a point source at a predetermined position (where the radiation feed antenna usually is positioned) and covering a predetermined area of the sub-reflector will be reflected and impinge on a predetermined area of the main reflector and will then be forwarded as a more or less collimated beam toward the  
30 satellite/antenna. Of course, radiation could travel in the opposite direction. This makes no difference.

The main and sub-reflectors preferably form a dual-reflector set-up, such as a so-called Cassegrain antenna set-up, a Gregorian antenna, displaced variants thereof or the like.

The feed antenna and sub-reflector may form a combined unit such as e.g. a splash plate feed, see e.g. US4058812.

- 5 The helix is adapted to emit radiation toward and/or receive radiation reflected off the main reflector, so as to be able to use the main reflector as a radiation collector and concentrator in the same manner as the sub-reflector.

When the sub-reflector is positioned between the main reflector and the helix, the helix will not attenuate the radiation travelling between the main and sub-reflectors.

- 10 In general, the emission characteristics of the helix depends on a number of factors, such as the number of conductors, the number of windings, the winding pitch, and the diameter of the helix. In addition, the diameter and position of the ground plane as well as the diameter thereof is of relevance. Also, the position of feeding the helix with power or tapping a signal from the helix is of importance.
- 15 Preferably, the helix has a central axis directed toward the main reflector, such as a centre of the main reflector.

Usually, an end fire helix will have a ground plane positioned at one end. Therefore, in one embodiment, the antenna further comprises an electrically conducting element positioned between the helix and the main reflector. Preferably, this ground plane or conducting element is positioned so as to ensure that the helix is in an end-fire configuration, and preferably, the helix is in a back-fire configuration. Back-fire configuration describes that the helix then is fed at the end the closest to the main reflector, and that the size of the ground plane is suitable.

- In Hisamatsu Nakano, Junji Yamauchi and Hiroaki Mimaki: "Backfire Radiation from a Monofilar Helix with a Small Ground Plane", IEEE Transactions on Antennas and Propagation, 25 Vol AP-36, No. 10, pp. 1359-1364, Oct. 1988, a detailed description is made as to how to generate a back-fire helix.

- In a preferred embodiment, the sub-reflector and the ground plane are one and the same element. This not only makes the device lighter and cheaper but also ensures that the helix may be positioned as closely to the sub-reflector as possible so that also the helix may be positioned close to the position at which the main reflector focuses received radiation or from where radiation may be provided on to the main reflector and from which it may subsequently form a nicely collimated beam.
- 30

In a preferred embodiment, the antenna further comprises a data provider and a controller, the controller being configured to:

- communicate with the feed antenna, the helix and the data provider,
- determine a signal quality and/or strength of a signal output of the feed antenna and/or the helix, and
- determine, from the determination, one of the feed antenna and the helix and feed a signal from the data provider to the determined one of the feed antenna and the helix.

In this context, the communication may be a receiving of signals from and/or a transmission of signals to the feed antenna and the helix. Usually, the feed antenna and the helix will, when receiving radiation, output a corresponding signal. Naturally, the corresponding signal may correspond to only a part of the received radiation, such as in situations where the feed antenna/helix is configured or able to only receive or convey certain frequencies or frequency intervals. In the same manner, the signal output from a feed antenna/helix may correspond to only certain frequencies or frequency intervals for the same reason.

The controller may be any type of controller, such as an ASIC, an FPGA, a DSP, a software controlled, general processor, a hardwired processor, a combination thereof or the like. The controller may be a single controller or may be a distributed controller formed of different parts communicating with each other, such as over one or more networks.

Naturally, the signal quality may be determined in any desired manner and may be quantified as desired, such as on the basis of:

- SNR – Signal to noise ratio  $\text{SNR(dB)} = 10 \cdot \log_{10}(P_{\text{signal}}/P_{\text{noise}})$ .
- BER – Bit Error Rate is the number of received binary bits that have been altered due to noise and interference, divided by the total number of transferred bits during a studied time interval.
- C/No – Carrier to Noise ratio.
- Eb/No – Energy per bit relative to noise power spectral density.
- PER – Packet Error Rate.

or other means of determining the data throughput rate and/or QoS of the link.

It is noted that the signal quality may very well differ for the different frequencies, and this determination may be made for each frequency, or the result at one frequency may be used for estimating the signal quality of another frequency.

- 5 It is noted that a number of data transmission protocols are adapted to evaluate a bandwidth possible at the frequency in question, and from this, the signal quality may be determined.

When the signal quality has been determined or estimated, the controller may output this or simply use it for the determination.

- 10 In some situations, the signal quality of either the signal from one of the helix and the feed antenna may always be lower. One such situation is one where the dual antenna receives radiation from a satellite and where the weather influences the radiation. When the helix and the feed antenna are adapted to receive different wavelengths or wavelength intervals, some wavelengths are inherently more influenced by weather (clouds and precipitation as rain and snow) than others. However, reasons may exist for wishing to use a frequency or frequency interval at which the signal quality is lower, such as when this type of communication, when possible, gives a higher data rate or bandwidth.

- 20 Thus, in some situations, it suffices to determine the signal quality of one of the signals from the helix and the feed antenna, such as that which always has the lower quality. If this suffices, that of the helix/feed antenna may then be used; otherwise the other is used. If the signal quality of also the other drops, no communication may be possible using the dual antenna, or it may be desired to direct the dual antenna toward another data transmitter if possible.

- 25 In another situation, the dual reflector antenna may be used for one type of communication and the helix for another type, simultaneously. Thus, the dual reflector set-up may be used for download of data where the helix may be used for a much lower bandwidth upload.

- 30 The data provider may be any type of data provider, such as a computer, a cell phone, a telephone, a video provider, a multimedia source, a telephone, or the like. The data provider may form part of the controller or may be separate therefrom. The data provider may be a single element or a distributed system of elements communicating with each other and/or the controller.

If the determination results in a communication with a lower bandwidth, the controller or the data provider may select or de-select predetermined types of data in order to ensure that the most important data are transmitted as long as data transmission is possible.

5 In one embodiment, the helix is configured to emit/receive radiation within a first wavelength interval and the feed antenna is configured to emit/receive radiation within a second wavelength interval.

Preferably, the first wavelength interval comprises wavelengths longer than any wavelength in the second wavelength interval.

10 Preferably, the first and second frequencies or frequency intervals are so different that the communication at these frequencies has different properties. Usually, such properties are defined at least in part by the frequencies, and it may be desired that the first frequency or interval is below 9 GHz and the second frequency is above 9 GHz, especially if the wireless communication takes place through air/the atmosphere. It is desired that the frequencies are sufficiently different for a difference in properties to exist, whereby it is desired that the  
15 second, higher frequency/interval is above 10 GHz. Also, in one embodiment it is desired that the first, lower frequency/interval is below 9 GHz or below 13 GHz.

IEEE has defined Radar-frequency bands, and it is thus preferred that the first frequency is defined in or around the HF, VHF, UHF, L band, S band, C band and X band frequency intervals. Usually, antenna dimensions make the use of frequencies lower than 100 MHz  
20 difficult, but this does not render such systems impossible.

Also, it is desired that the second frequency/interval is in or around the X band, Ku band, K band, Ka band, V band, W band or mm band intervals. Usually, the higher the frequency of the carrier, the higher a bandwidth may be transported, but such systems often are more vulnerable to interference etc.

25 It is noted that the first and/or second frequencies/intervals may each be selected within a pre-defined band, which bands then preferably are different. Also, a frequency often is not merely provided as a single frequency but as a frequency selected within an interval of frequencies. Thus, any frequency described hereafter may be a single frequency or a frequency determined or selected within a frequency interval. Preferably, both selected  
30 frequencies as well as frequency intervals are non-overlapping.

In one embodiment, the feed antenna has a waveguide having an axis of symmetry and wherein the sub-reflector and the helix are positioned on the axis of symmetry. In this

situation, the dual reflector antenna set-up may be rotational symmetric, and the positioning of the helix also on the symmetry axis minimizes the shadowing of the helix in the radiation received by or emitted by the main reflector while keeping the helix away from the path of the radiation transmitted between the main and sub-reflectors.

- 5 The waveguide may be a waveguide adapted to receive radiation and guide it to a detector, or receive radiation from an emitter and guide it toward the sub-reflector.

In another situation, the helix and sub-reflector may be positioned along a line from a centre of the main reflector and the signal source/destination, such as another antenna or a satellite. In that situation, the helix may be positioned in a "shadow" of the sub-reflector and  
10 thus not in itself deteriorate the signal to any substantial degree.

In one embodiment, the dual antenna further comprises a cable, such as having two or more conductors, connected to the helix, the cable extending, between the feed antenna and the helix, along the axis of symmetry and/or in a zero field area and thus have a very low detrimental effect on the radiation travelling in the feed antenna.

- 15 In general, the present dual antenna may be used for communication with other antennas, such as antennas provided on satellites. The present dual antenna is especially suitable for communicating through the atmosphere, as the dual antenna set-up makes it possible to communicate at different frequencies, which may be required due to atmosphere interference.
- 20 The present dual antenna thus may be suitable for use in or on a house, a vehicle, a boat or the like. Alternatively, the antenna may be used in a ground based station usually being a structure fixed in relation to the ground and adapted to communicate with one or more satellites. Such structures may also be called SAS – Satellite Access Station, RAN – Radio Access Node, Earth Station, Ground Station, satellite gateway or LES – Land Earth Station.
- 25 In the following, preferred embodiments of the invention will be described with reference to the drawing, wherein:
  - Figure 1 illustrates a first embodiment according to the invention,
  - Figure 2 illustrates a second embodiment according to the invention, and
  - Figure 3 illustrates a third embodiment according to the invention.

In figure 1, a dual-reflector antenna is illustrated having a main reflector 100 and a sub-reflector 104 as well as a feed antenna 101. Radiation travels through the feed antenna 101, impinges on the sub-reflector 104 and reflects off the main reflector 100 to form (or be detected as) a parallel beam along the (horizontal in the drawing) axis of symmetry of the main reflector 100. Preferably, the main reflector 100, feed antenna 101 and sub-reflector 104 are rotational symmetric around this axis.

The sub-reflector 104 is held by a narrow tube 103 extending along the axis of symmetry.

Provided is also a helix 102, which is fed by a cable extending inside the tube 103 and which is configured to also use the main reflector 100 for collecting and focussing radiation onto the helix or directing radiation from the helix 102 into a beam along the axis of symmetry. Alternatively, the tube 103 may constitute a conductor, such as an outer conductor of the cable then being e.g. a semi-rigid coaxial cable.

The helix 102 is fed in a so-called back-fire configuration and thus uses the sub-reflector 104 as the ground plane. Naturally, a separate ground plane may be provided for the helix 102.

Thus, a number of advantages are obtained. Firstly, the main reflector 100 is used by both antennas (dual-reflector setup and the helix), whereby a light weight, compact dual antenna is obtained. Also, the position of the helix 102 is advantageous in that it has only very little impact on the operation of the dual-reflector antenna, as it is positioned in the "shadow" of the sub-reflector 104. In the figure, a satellite 10 is illustrated which transmits information, such as data, at one or more wavelengths toward the antenna, and/or the antenna is emitting data toward the satellite.

Usually, in satellite communication, the weather will determine the signal strength and thus the signal quality at different frequencies. The present dual antenna may thus be used for communicating the same data or with the same antenna, whereby the dual-reflector antenna or a larger frequency is used when the weather or conditions permit and where the helix or a lower frequency is used when required even though this will usually entail communicating with a lower bandwidth.

In one situation, the dual-reflector antenna is adapted to operate in the so-called Ka-band (e.g. the 20-30 GHz frequency range) and thus be capable of providing a bandwidth of more than 100 Mbit/s, whereas the helix may be adapted to operate in the so-called L-band (the 1-2 GHz frequency range), there providing typically up to 0.5 Mbit/s data rate.



The signal to/from the two antennas may be fed to a controller 12 which determines the signal strength or quality to/from the satellite 10 and determines which of the two antennas to use.

The controller 12 thus may be connected to (not illustrated but may be comprised therein for illustrative purposes) a data provider which provides data to be transmitted to the satellite and potentially to another recipient, where the controller determines, based on the signal quality/strength, whether to transmit the data to the satellite using the dual-reflector antenna or the helix. Naturally, the controller may be connected to a typical PC or the like, receiving data from the antenna. The PC may also be the data provider providing the data to be transmitted. The other recipient may be available over the internet, which may be communicated with via the satellite 10. Thus, the data forwarded from the satellite 10 may be received from the internet and may be streamed media information, such as streamed radio, video, movies, TV channels or the like, or may be mails, other data, weather information, home pages or the like. The data forwarded to the other recipient and/or the satellite may be URLs, data, mails, video, images, audio or any other type of data.

The data transmission toward the satellite 10 thus may be controlled to take place using that of the antennas having the best (or at least a minimum) signal quality/strength.

Naturally, the controller may then determine how to reduce that data to be fed to the satellite when the amount of desired data exceeds that possible due to the (weather) conditions, such as by removing leisure data and maintaining important data, allowing primarily predetermined types of data (communication, weather information or the like) and disallowing streaming video/TV/movies, if the available bandwidth does not allow both.

Another manner of operating or using the antenna is to use one of the dual reflector set-up and the helix for one type of data or data in one direction, such as download, while the other of the dual reflector set-up and the helix is used for another type of data or e.g. upload.

In figure 2, a slightly different set-up is seen which also has a dual-reflector antenna is illustrated with a main reflector 200 and a sub-reflector 204 as well as a feed antenna 201.

The sub-reflector 204 is held by a number of struts 205 also holding a cable feeding or transporting a signal from a helix 202 again positioned on the symmetry axis of the main reflector. Again, the helix 202 is fed in a so-called back-fire set-up using, again, the sub-reflector 204 as the ground plane.

In all embodiments, the parameters of the helix may be altered, such as the feed position (point of contact between the feeding cable and the helix), as long as the helix is configured to direct a signal toward the main reflector 100 or receive signals therefrom.

5 Naturally, the dual-reflector antenna and the helix based antenna may be used for transmitting or receiving the same frequency or wavelength or different frequencies/wavelengths.

Again, the satellite 10 and the controller 12 are illustrated.

10 In figure 3, a non-rotationally symmetric set-up is illustrated in which the main reflector 100 reflects the radiation on to the sub-reflector 104, reflecting the radiation toward the feed antenna 101 positioned away from the main reflector 100.

Behind the sub-reflector 104, again, the helix 102 is positioned. The helix 102, in the same manner, is positioned so as to receive radiation reflected by the main reflector 100 and/or emit radiation toward the main reflector 100.

Again, the helix 102 is in a backfire set-up using the sub-reflector 102 as the ground plane.

15

## CLAIMS

1. A dual antenna comprising:

- a main reflector,
- a sub-reflector,
- 5 - a helix,
- a feed antenna,

wherein:

- the feed antenna is positioned so as to receive radiation reflected by the sub-reflector and/or emit radiation toward the sub-reflector,
- 10 - the helix is adapted to emit radiation toward and/or receive radiation reflected off the main reflector,

wherein the sub-reflector is positioned between the main reflector and the helix.

2. An antenna according to claim 1, further comprising an electrically conducting element positioned between the helix and the main reflector.

15 3. An antenna according to claim 1, wherein the sub-reflector and the conducting element are one and the same element.

4. An antenna according to any of the preceding claims, further comprising a data provider and a controller, the controller being configured to:

- communicate with the feed antenna, the helix and the data provider,
- 20 - determine a signal quality and/or strength of a signal output of the feed antenna and/or the helix, and
- determine, from the determination, one of the feed antenna and the helix and feed a signal from the data provider to the determined one of the feed antenna and the helix.

5. An antenna according to any of the preceding claims, wherein the feed antenna is configured to emit/receive radiation within a first wavelength interval and the helix is configured to emit/receive radiation within a second wavelength interval, the first wavelength interval comprising a wavelength shorter than any wavelength in the second wavelength interval.

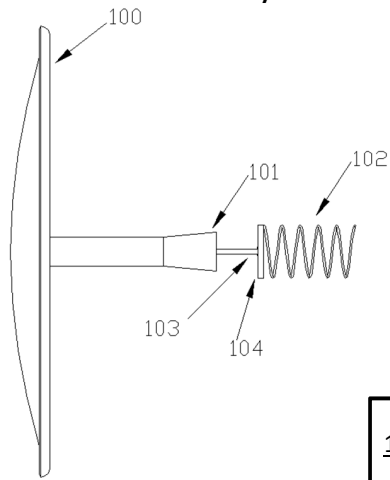
6. An antenna according to any of the preceding claims, wherein the feed antenna has a wave guide having an axis of symmetry and wherein the sub-reflector and the helix are positioned on the axis of symmetry.

7. An antenna according to claim 6, further comprising a cable connected to the helix, the cable extending, between the feed antenna and the helix, along the axis of symmetry.

## SUMMARY

A dual antenna comprising a dual reflector set-up with a main reflector, a sub-reflector and a feed antenna, where a helix is provided which also utilizes the main reflector. The sub-reflector is positioned between the main reflector and the helix so that the helix will not  
5 unnecessarily disturb the operation of the dual reflector set-up while using the main reflector.

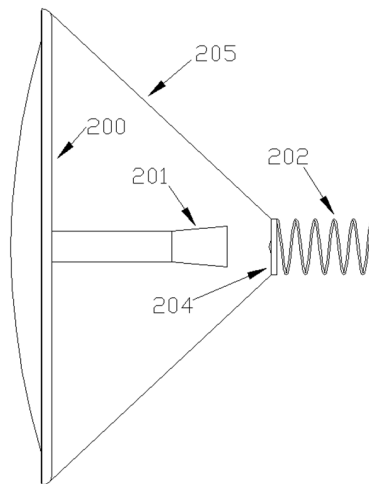
1/2



10

12

Figure 1



10

12

Figure 2

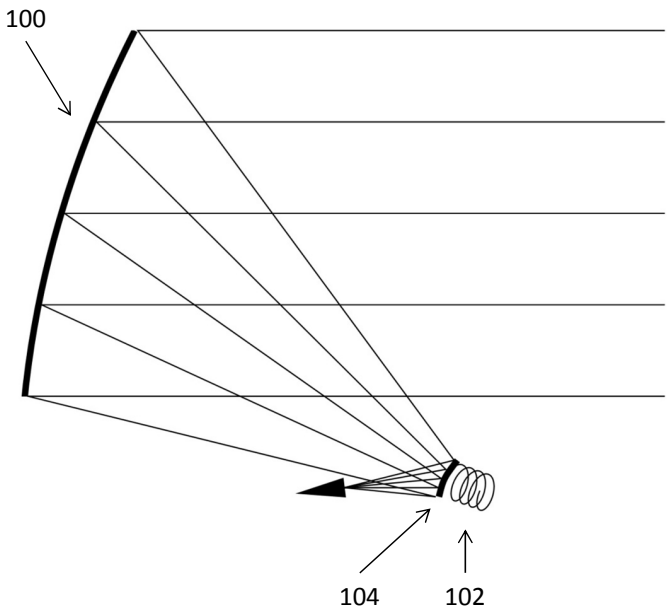


Figure 3

## BIBLIOGRAPHY

---

- [1] B. R. Elbert, *The Satellite Communication Applications Handbook*, 2nd ed. Artech House, 2004.
- [2] F. Gargione, T. Iida, F. Valdoni, and F. Vatalaro, “Services, technologies, and systems at ka band and beyond—a survey,” *IEEE J. Select. Areas Commun.*, vol. 17, no. 2, pp. 133–144, 1999.
- [3] “Inmarsat Global Xpress,” <http://www.igx.com/>.
- [4] “Inmarsat BGAN,” <http://www.inmarsat.com/services/bgan>.
- [5] “SAILOR 500 FleetBroadband Product Sheet,” <http://www.cobham.com/>.
- [6] T. Kitsuregawa, *Advanced Technology in Satellite Communication Antennas: Electrical & Mechanical Design*, 2nd ed. Artech House, 1990.
- [7] W. L. Stutzman and G. A. Thiele, *Antenna Theory and Design*, 2nd ed. Wiley, 1997.
- [8] H. Ehrenspeck, “A new class of medium-size high-efficiency reflector antennas,” *IEEE Trans. Antennas Propag.*, vol. 22, no. 2, pp. 329–332, 1974.
- [9] H. King and J. Wong, “240–400 MHz antenna system for the FleetSatCom satellites,” in *IEEE AP-S Int. Symp.*, vol. 15, 1977, pp. 349–352.
- [10] M. K. V. Heyningen, “Mobile satellite communication system including a dual-frequency, low-profile, self-steering antenna assembly,” U.S. Patent 5 835 057, Nov., 1998.
- [11] G. A. Seck, “Dual-band feed for microwave reflector antenna,” U.S. Patent 5 926 146, Jul., 1999.
- [12] V. Agrawal and W. Imbriale, “Design of a dichroic cassegrain subreflector,” *IEEE Trans. Antennas Propag.*, vol. 27, no. 4, pp. 466–473, Jul. 1979.
- [13] J. Huang, T.-K. Wu, and S.-W. Lee, “Tri-band frequency selective surface with circular ring elements,” *IEEE Trans. Antennas Propag.*, vol. 42, no. 2, pp. 166–175, Feb. 1994.
- [14] S. Barkeshli, T. Smith, H. S. Luh, L. Ersoy, and T. Itanami, “On the analysis and design of the frequency selective surface for the n-star satellite Ku/S-shaped reflector,” in *IEEE AP-S Int. Symp.*, vol. 3. IEEE, Jun. 1995, pp. 1656–1658 vol.3.



- [15] C. Tienda, P. Otero, and M. P. Garcia, "Design of a dichroic subreflector for an antenna operating at s and x bands," in *Proc. EuCAP*. IET, Nov. 2007, pp. 1–5.
- [16] G. R. Stroes, P. J. Loner, J. Santoru, E. C. Chen, and N. Motamed, "Method and apparatus for receiving dual band signals from a common orbital location with an outdoor unit using a frequency selective subreflector and additional antenna feed," U.S. Patent 20 080 120 654, May, 2008.
- [17] T. K. Wu, *Frequency selective surface and grid array*. Wiley, 1995.
- [18] B. Munk, *Frequency selective surfaces : theory and design*. Wiley, 2000.
- [19] C. Chen and T. Tung, "A dual-frequency antenna with dichroic reflector and microstrip array sharing a common aperture," in *IEEE AP-S Int. Symp.*, vol. 20, 1982, pp. 296–299.
- [20] S. Lin, B. Munk, S. Nichols, and R. Brown, "A small dual band SATCOM antenna for x- and q-band," in *IEEE AP-S Int. Symp.*, vol. 20, 1982, pp. 483–486.
- [21] J. James and G. Andrasic, "Dichroic dual-band microstrip array," *Electron. Lett.*, vol. 22, no. 20, pp. 1040–1042, 1986.
- [22] S. D. Targonski and D. M. Pozar, "An L/X dual-band dual-polarized shared-aperture array for spaceborne SAR," in *IEEE AP-S Int. Symp.*, vol. 4, 1999, pp. 2306–2309 vol.4.
- [23] J. Granholm and N. Skou, "Dual-frequency, dual-polarization microstrip antenna development for high-resolution, airborne SAR," in *Asia-Pacific Microwave Conference*, 2000, pp. 17–20.
- [24] J. Granholm, "Dual-frequency and dual-polarization antennas - an investigation of their suitability for high-resolution airborne SAR," Ph.D. dissertation, Technical University of Denmark, 2000.
- [25] D. M. Pozar and S. D. Targonski, "A shared-aperture dual-band dual-polarized microstrip array," *IEEE Trans. Antennas Propag.*, vol. 49, no. 2, pp. 150–157, 2001.
- [26] M. Meng, F. Zhang, X. Ding, K. Ding, and L. Li, "Design of a shared-aperture dual-band dual-polarized microstrip antenna," in *IEEE Int. Symp. Microw. Antenna Propag. EMC Technol. Wireless Commun.*, 2009, pp. 680–683.
- [27] S.-G. Zhuo and T.-H. Chio, "A wideband, low profile p- and ku-band dual polarized shared aperture antenna," in *IEEE AP-S Int. Symp.*, 2012, pp. 794–797.
- [28] J. Huang, "A ka-band circularly polarized high-gain microstrip array antenna," *IEEE Trans. Antennas Propag.*, vol. 43, no. 1, pp. 113–116, 1995.
- [29] A. Sabban, "Ka band microstrip antenna arrays with high efficiency," in *IEEE AP-S Int. Symp.*, vol. 4, 1999, pp. 2740–2743 vol.4.
- [30] J. Huang and J. A. Encinar, *Reflectarray Antennas*. IEEE Press, 2008.

- [31] J. A. Encinar, "Recent advances in reflectarray antennas," in *Proc. EuCAP*, 2010, pp. 1–6.
- [32] D. M. Pozar, "Bandwidth of reflectarrays," *Electron. Lett.*, vol. 39, no. 21, pp. 1490–1491, 2003.
- [33] J. Encinar and J. Zornoza, "Broadband design of three-layer printed reflectarrays," *IEEE Trans. Antennas Propag.*, vol. 51, no. 7, pp. 1662–1664, Jul. 2003.
- [34] D. Pozar, "Wideband reflectarrays using artificial impedance surfaces," *Electron. Lett.*, vol. 43, no. 3, pp. 148–149, 2007.
- [35] E. Carrasco, J. A. Encinar, and M. Barba, "Bandwidth improvement in large reflectarrays by using True-Time delay," *IEEE Trans. Antennas Propag.*, vol. 56, no. 8, pp. 2496–2503, 2008.
- [36] K. Mayumi, H. Deguchi, and M. Tsuji, "Wideband single-layer microstrip reflectarray based on multiple-resonance behavior," in *IEEE AP-S Int. Symp.* IEEE, Jul. 2008, pp. 1–4.
- [37] G. Zhao, Y.-C. Jiao, F. Zhang, and F.-S. Zhang, "A subwavelength element for broadband circularly polarized reflectarrays," *IEEE Antennas Wireless Propag. Lett.*, vol. 9, pp. 330–333, 2010.
- [38] J. A. Encinar, "Design of a dual frequency reflectarray using microstrip stacked patches of variable size," *Electron. Lett.*, vol. 32, no. 12, pp. 1049–1050, Jun. 1996.
- [39] J. Shaker, C. Pike, and M. Cuhaci, "A dual orthogonal cassegrain flat reflector for ka-band application," *Microwave Opt. Technol. Lett.*, vol. 24, no. 1, pp. 7–11, Jan. 2000.
- [40] E. B. Felstead, J. Shaker, M. R. Chaharmir, and A. Petosa, "Enhancing multiple-aperture ka-band navy SATCOM antennas with electronic tracking and reflectarrays," in *Proc. MILCOM*, ser. 1, vol. 2002. IEEE, Oct. 2002, pp. 168–172.
- [41] N. Misran, R. Cahill, and V. Fusco, "Concentric split ring element for dual frequency reflectarray antennas," *Electron. Lett.*, vol. 39, p. 1776, 2003.
- [42] C. Han, C. Rodenbeck, J. Huang, and K. Chang, "A C/Ka dual frequency dual layer circularly polarized reflectarray antenna with microstrip ring elements," *IEEE Trans. Antennas Propag.*, vol. 52, pp. 2871–2876, Nov. 2004.
- [43] C. Han, J. Huang, and K. Chang, "A high efficiency offset-fed x/ka-dual-band reflectarray using thin membranes," *IEEE Trans. Antennas Propag.*, vol. 53, pp. 2792–2798, Sep. 2005.
- [44] R. Chaharmir, J. Shaker, and M. Cuhaci, "Development of dual-band circularly polarised reflectarray," in *IEE Proc. Microwaves, Antennas Propag.*, vol. 153, 2006, pp. 49–54.
- [45] C. Han, S. Hsu, K. Chang, and J. Huang, "A Ku/Ka-dual band reflectarray to emulate a cylindrical reflector for titan cloud precipitation radar and altimeter," in *IEEE AP-S Int. Symp.* IEEE, Jun. 2007, pp. 1445–1448.

- [46] S.-H. Hsu and K. Chang, "A new dual-band reflectarray configuration," in *IEEE AP-S Int. Symp.*, 2008, pp. 1–4.
- [47] M. Chaharmir, J. Shaker, and H. Legay, "Broadband design of a single layer large reflectarray using multi cross loop elements," *IEEE Trans. Antennas Propag.*, vol. 57, pp. 3363–3366, Oct. 2009.
- [48] M. R. Chaharmir, J. Shaker, N. Gagnon, and D. Lee, "Design of broadband, single layer dual-band large reflectarray using multi open loop elements," *IEEE Trans. Antennas Propag.*, vol. 58, no. 9, pp. 2875–2883, Sep. 2010.
- [49] C. Guclu, J. Perruisseau-Carrier, and O. A. Civi, "Dual frequency reflectarray cell using split-ring elements with RF MEMS switches," in *IEEE AP-S Int. Symp.*, 2010, pp. 1–4.
- [50] C. Guclu, J. Perruisseau-Carrier, and O. Civi, "Proof of concept of a dual-band circularly-polarized RF MEMS beam-switching reflectarray," *IEEE Trans. Antennas Propag.*, vol. 60, no. 11, pp. 5451–5455, Nov. 2012.
- [51] F. Yang, Y. Kim, J. Huang, and A. Elsherbeni, "A single-layer tri-band reflectarray antenna design," in *IEEE AP-S Int. Symp.*, 2007, pp. 5307–5310.
- [52] S.-W. Oh, J.-K. Lee, J. Huang, and K. Chang, "A six-band reflectarray antenna," in *IEEE AP-S Int. Symp.*, Jun. 2009, pp. 1–4.
- [53] J. W. M. Baars, *The Paraboloidal Reflector Antenna in Radio Astronomy and Communication*, 1st ed. Springer, 2007.
- [54] R. Johnson and R. Cotton, "A backfire helical feed," *IEEE Trans. Antennas Propag.*, vol. 32, no. 10, pp. 1126–1128, Oct. 1984.
- [55] P.-S. Kildal, S. Skyttemyr, and A. KISHK, "G/T maximization of a paraboloidal reflector fed by a dipole-disk antenna with ring by using the multiple-reflection approach and the moment method," *IEEE Trans. Antennas Propag.*, vol. 45, no. 7, pp. 1130–1139, Jul. 1997.
- [56] J. D. Kraus, *Antennas*, 2nd ed. McGraw-Hill, 1988.
- [57] H. Nakano, Y. Samada, and J. Yamauchi, "Axial mode helical antennas," *IEEE Trans. Antennas Propag.*, vol. 34, no. 9, pp. 1143–1148, 1986.
- [58] M. Roy, "Constructing normal-mode helical antennas," *IEE-IERE Proc. - India*, vol. 7, pp. 119–123, 1969.
- [59] W. T. Patton, "The backfire helical antenna," Ph.D. dissertation, University of Illinois, 1963.
- [60] H. Nakano, J. Yamauchi, and H. Mimaki, "Backfire radiation from a monofilar helix with a small ground plane," *IEEE Trans. Antennas Propag.*, vol. 36, no. 10, pp. 1359–1364, Oct. 1988.
- [61] "Ansys HFSS," <http://www.ansys.com>.

- [62] A. R. Djordjevic, M. B. Bazdar, V. V. Petrovic, D. I. Olcan, T. K. Sarkar, and R. F. Harrington, *AWAS for Windows, Version 2.0, Analysis of Wire Antennas and Scatterers, Software and User Manual*. Artech House, 2002.
- [63] H. Nakano, S. Iio, and J. Yamauchi, "Improvement in front-to-back ratio of a bifilar backfire helix by a flared open end," *IEEE Trans. Antennas Propag.*, vol. 41, no. 11, Nov. 1993.
- [64] A. Sommerfeld, *Optics*. Academic Press, Inc., New York, 1954.
- [65] J. B. KELLER, "Geometrical theory of diffraction," *Journal of the Optical Society of America*, vol. 52, no. 2, pp. 116–130, Feb. 1962.
- [66] "TICRA GRASP," <http://www.ticra.com/products/software/grasp>.
- [67] M. Wahid and S. B. Morris, "Band pass radomes for reduced RCS," in *IEE Colloquium on Antenna Radar Cross-Section*, 1991, pp. 4/1–4/9.
- [68] H. Chen, X. Hou, and L. Deng, "Design of frequency-selective surfaces radome for a planar slotted waveguide antenna," *IEEE Antennas Wireless Propag. Lett.*, vol. 8, pp. 1231–1233, 2009.
- [69] R. Mittra, C. H. Chan, and T. Cwik, "Techniques for analyzing frequency selective surfaces-a review," *Proc. IEEE*, vol. 76, no. 12, pp. 1593–1615, Dec. 1988.
- [70] F. Bayatpur and K. Sarabandi, "Multipole spatial filters using metamaterial-based miniaturized-element frequency-selective surfaces," *IEEE Trans. Microwave Theory Techn.*, vol. 56, no. 12, pp. 2742–2747, 2008.
- [71] J. Epis, "Broadband antenna polarizer," U.S. Patent 3 754 271, Aug., 1973.
- [72] W. M. Shi, W. X. Zhang, and M. G. Zhao, "Novel frequency-selective twist polariser," *Electron. Lett.*, vol. 27, no. 23, pp. 2110–2111, 1991.
- [73] M. Euler, V. Fusco, R. Cahill, and R. Dickie, "325 GHz single layer sub-millimeter wave FSS based split slot ring linear to circular polarization convertor," *IEEE Trans. Antennas Propag.*, vol. 58, no. 7, pp. 2457–2459, 2010.
- [74] M.-A. Joyal and J. Laurin, "A cascaded circular-polarization-selective surface at k band," in *IEEE AP-S Int. Symp.*, 2011, pp. 2657–2660.
- [75] A. Yahaghi, A. Fallahi, H. Abiri, M. Shahabadi, C. Hafner, and R. Vahldieck, "Analysis of frequency selective surfaces on periodic substrates using entire domain basis functions," *IEEE Trans. Antennas Propag.*, vol. 58, pp. 876–886, Mar. 2010.
- [76] "Ansys Designer," <http://www.ansys.com>.
- [77] J. Gianvittorio, J. Romeu, S. Blanch, and Y. Rahmat-Samii, "Self-similar pre-fractal frequency selective surfaces for multiband and dual-polarized applications," *IEEE Trans. Antennas Propag.*, vol. 51, no. 11, pp. 3088–3096, 2003.
- [78] J. Romeu and Y. Rahmat-Samii, "Fractal FSS: a novel dual-band frequency selective surface," *IEEE Trans. Antennas Propag.*, vol. 48, no. 7, pp. 1097–1105, 2000.

- [79] M.-J. Huang, M.-Y. Lv, J. Huang, and Z. Wu, "A new type of combined element multiband frequency selective surface," *IEEE Trans. Antennas Propag.*, vol. 57, pp. 1798–1803, Jun. 2009.
- [80] E. A. Parker, S. M. Hamdy, and R. J. Langley, "Arrays of concentric rings as frequency selective surfaces," *Electron. Lett.*, vol. 17, no. 23, pp. 880–881, Nov. 1981.
- [81] R. Cahill and E. A. Parker, "Concentric ring and jerusalem cross arrays as frequency selective surfaces for a  $45^\circ$  incidence diplexer," *Electron. Lett.*, vol. 18, no. 8, pp. 313–314, Apr. 1982.
- [82] A. N. Tulintseff and Y. Rahmat-Samii, "Scattering analysis of FSS reflectors using huygen's principle," in *IEEE AP-S Int. Symp.*, vol. 2, 1992, pp. 1173–1176.
- [83] M. Houghs, "Design and measurement of a frequency selective surface for a circularly polarized reflector antenna," Master's thesis, Technical University of Denmark, 2012.
- [84] J. Shaker and M. Cuhaci, "Multi-band, multi-polarisation reflector-reflectarray antenna with simplified feed system and mutually independent radiation patterns," *IEE Proc. Microw. Antennas Propag.*, vol. 152, no. 2, pp. 97–101, 2005.
- [85] M. Chaharmir, J. Shaker, and H. Legay, "Dual-band Ka/X reflectarray with broadband loop elements," *IET Microw., Antennas Propag.*, vol. 4, p. 225, 2010.
- [86] J. Shaker, R. Chaharmir, and H. Legay, "Investigation of FSS-Backed reflectarray using different classes of cell elements," *IEEE Trans. Antennas Propag.*, vol. 56, pp. 3700–3706, Dec. 2008.
- [87] M. R. Chaharmir, J. Shaker, and H. Legay, "FSS-backed reflectarray with broadband square loop cell elements for dualband application," in *IEEE AP-S Int. Symp.*, 2008, pp. 1–4.
- [88] H. Li, B.-Z. Wang, G. Zheng, W. Shao, and L. Guo, "A reflectarray antenna backed on FSS for low RCS and high radiation performances," *Progress In Electromagnetics Research C*, vol. 15, pp. 145–155, 2010.
- [89] J. Li, Q. Chen, K. Sawaya, and Q. Yuan, "Amplitude controlled reflectarray using non-uniform FSS reflection plane," in *IEEE AP-S Int. Symp.*, 2011, pp. 2180–2183.
- [90] J. A. Encinar, M. Arrebola, and G. Toso, "A parabolic reflectarray for a bandwidth improved contoured beam coverage," in *Proc. EuCAP*, 2007, pp. 1–5.
- [91] A. Roederer, "Reflector antenna comprising a plurality of panels," NL Patent US 6 411 255, 2002.
- [92] —, "Reflectarray antennas," in *Proc. EuCAP*, 2009, pp. 18–22.
- [93] H. Legay, D. Bresciani, E. Labiole, R. Chiniard, E. Girard, G. Caille, D. Calas, R. Gillard, and G. Toso, "A 1.3 m faceted reflectarray in ku band," in *ANTEM Int. Symp.*, 2012, pp. 1–4.

- [94] D. M. Pozar, S. D. Targonski, and H. D. Syrigos, "Design of millimeter wave microstrip reflectarrays," *IEEE Trans. Antennas Propag.*, vol. 45, no. 2, pp. 287–296, 1997.
- [95] M. Zhou, S. Sorensen, E. Jorgensen, P. Meincke, O. Kim, and O. Breinbjerg, "An accurate technique for calculation of radiation from printed reflectarrays," *IEEE Antennas Wireless Propag. Lett.*, vol. 10, pp. 1081–1084, 2011.
- [96] C. Güçlü, "Dual frequency reconfigurable reflectarray antenna of split ring elements with rf mems switches," Master's thesis, The Graduate of Natural and Applied Sciences of Middle East Technical University, 2010.
- [97] J. Huang and R. Pogorzelski, "A Ka-band microstrip reflectarray with elements having variable rotation angles," *IEEE Trans. Antennas Propag.*, vol. 46, no. 5, pp. 650–656, 1998.
- [98] M. Zhou, "Accurate modeling of advanced reflectarrays," Ph.D. dissertation, Technical University of Denmark, 2012.
- [99] "TICRA CHAMP," <http://www.ticra.com/products/software/champ>.
- [100] "DTU-ESA spherical near-field antenna test facility," [http://www.dtu.dk/centre/ems/English/research/dtu\\_esa\\_facility.aspx](http://www.dtu.dk/centre/ems/English/research/dtu_esa_facility.aspx).
- [101] J. Perruisseau-Carrier, "Recent developments in reconfigurable reflectarrays," in *Proc. ICECom*, 2010, pp. 1–4.
- [102] J. Encinar, C. Tienda, E. Carrasco, M. Arrebola, and G. Toso, "Design of dual-reflectarray antenna for beam scanning," in *IEEE AP-S Int. Symp.*, 2010, pp. 1–4.
- [103] K. W. Whites and R. Mittra, "An equivalent boundary-condition model for lossy planar periodic structures at low frequencies," *IEEE Trans. Antennas Propag.*, vol. 44, no. 12, pp. 1617–1629, Dec. 1996.



## **[www.elektro.dtu.dk](http://www.elektro.dtu.dk)**

Department of Electrical Engineering

Electromagnetic Systems

Technical University of Denmark

Ørstedes Plads

Building 348

DK-2800 Kgs. Lyngby

Denmark

Tel: (+45) 45 25 38 00

Fax: (+45) 45 93 16 34

Email: [info@elektro.dtu.dk](mailto:info@elektro.dtu.dk)